UNIVERSITY OF CALIFORNIA, SAN DIEGO

Momentum balance in the Southern Ocean

A dissertation submitted in partial satisfaction of the
requirements for the degree
Doctor of Philosophy

in

Oceanography

by

Jessica Jean Millar Masich

Committee in charge:

Teresa K. Chereskin, Chair
Sarah T. Gille
Matthew R. Mazloff
Dean Roemmich
Sutanu Sarkar
Lynne D. Talley

2017

The dissertation of Jessica Jean Millar Masich is approved, and it is acceptable in quality and form for publication on microfilm and electronically:

_____

_____

_____

_____

_____

_____

Chair

University of California, San Diego

2017

EPIGRAPH

One could not be sure that the sea and the ground were horizontal,

hence the relative position of everything else seemed phantasmally variable...

— H. P. Lovecraft, The Call of Cthulhu

TABLE OF CONTENTS

LIST OF FIGURES

LIST OF TABLES

ACKNOWLEDGEMENTS

First and foremost, I would like to thank my advisor, Teri Chereskin. Her wisdom, patience, and precision have helped me to grow as a scientist and as a person more than I could have imagined when I came to SIO. Thank you also to my coauthor and committee member Matt Mazloff, whose depth of knowledge and buoyant enthusiasm has propelled me through many of the stickier problems that we have faced in putting this work together. It has been a privilege to work with both of you.

Thank you to my committee, Sarah Gille, Lynne Talley, Dean Roemmich, and Sutanu Sarkar, for their guidance on this work, and to the many instructors here at Scripps who have turned me into an oceanographer. Scripps is an extraordinary community, and I have been so privileged to learn from the very best.

I am grateful to all of my friends here at Scripps, especially the Fiedler-Kannbergs and the Nierenberg Hall 3rd floor team, for all the things I have learned from you, and for all the fun that we have had along the way. From the big things like weddings and defenses to the smaller things like bird invasions and flamingo conventions, from late-night work parties to encouraging each other to just! keep! writing! in Thesis Club – I am so grateful to have shared this journey with you.

A big thanks to Randy Watts, Kathy Donohue, Karen Tracy, Gerry Chaplin, Erran Sousa, Annie Foppert and Yvonne Firing for their work collecting, processing, and analyzing the data from the cDrake experiment. Gathering data from the Drake Passage is no joke, and working with you all on the 2011 instrument recovery cruise was one of the highlights of my life.

Finally, thank you to Max Masich, my husband, who knows what he did.

Chapter Two, in full, is a reprint of the material as it appears in the Journal of Geophysical Research: Oceans, 2015. Masich, J., T. K. Chereskin, and M. R. Mazloff (2015), Topographic form stress in the Southern Ocean State Estimate, *J. Geophys. Res. Oceans*, 120, 7919-7933, doi:10.1002/2015JC011143. The dissertation author was the primary investigator and author of this paper.

Chapter Three, in part, has been submitted to the Journal of Geophysical Research: Oceans. Masich, J., M. R. Mazloff, and T. K. Chereskin. The dissertation/thesis author was the primary investigator and author of this paper.

Chapter Four is currently being prepared for submission for publication of the material. Masich, J., T. K. Chereskin, and M. R. Mazloff. The dissertation author was the primary investigator and author of this material.

VITA

2008	B. A. in Physics with General Honors and minor in Environmental Studies, University of Chicago
2008-2010	Environmental Scientist, Environmental Protection Agency Region 5
2014	M. S. in Oceanography, University of California, San Diego
2017	Ph. D. in Oceanography, University of California, San Diego

PUBLICATIONS

Masich, J., T. K. Chereskin, and M. R. Mazloff (2015), Topographic form stress in the Southern Ocean State Estimate, *J. Geophys. Res. Oceans*, 120, 7919-7933, doi:10.1002/2015JC011143.

ABSTRACT OF THE DISSERTATION

Momentum balance in the Southern Ocean

by

Jessica Jean Millar Masich

Doctor of Philosophy in Oceanography

University of California, San Diego, 2017

Teresa K. Chereskin, Chair

Strong, year-round eastward wind forcing drives the Antarctic Circumpolar Current (ACC), the Southern Ocean's dominant current, on an unbroken path around the Antarctic continent. This near-constant source of eastward wind stress momentum must find a sink, lest the current accelerate indefinitely. The path that this wind stress momentum travels from source to sink plays an essential role in setting the strength and structure of the upwelling branch of the meridional overturning circulation, a key nexus of heat and carbon exchange between the deep ocean and the atmosphere.

This thesis maps Southern Ocean momentum sinks and the pathways that momentum travels through the fluid from source to sink. Using the Southern Ocean State

Estimate, a 1/6 degree, data-assimilating model of the Southern Ocean south of 24.7°S, we find that 95% of wind stress momentum exits the fluid via topographic form stress: 58% across submerged ridges, and 42% across the land masses that block the ACC (Chapter Two). We isolate the interfacial form stress field for the first time in a general circulation model, finding that interfacial form stress carries zonal momentum from source to sink, balancing wind stress, topographic form stress, and thermodynamic forcing to help set the structure of the meridional overturning circulation in the Southern Ocean (Chapter Three). We find that transient eddy interfacial form stress dominates the total interfacial form stress field and tends to concentrate along the six largest topographically steered currents in the ACC. Finally, we explore interfacial form stress via observational data from the cDrake experiment, a four-year deployment of current and pressure recording inverted echo sounders across a standing meander in the Sub Antarctic and Polar Fronts in the Drake Passage (Chapter Four). The cDrake observational estimate aligns closely with previous observational estimates in the region, and provides a strong ground-truth for the model interfacial form stress field.

Chapter 1

Introduction

The ocean encircles the globe in only one place: the Southern Ocean, where the Antarctic Circumpolar Current (ACC) carries 173.3 ± 10.7 Sverdrups of seawater on an unbroken path around Antarctica (Donohue et al., 2016). Eastward wind forcing over the Southern Ocean drives the ACC along its path. Because the current does not accelerate indefinitely, the momentum input by wind stress must find an exit from the fluid system. This thesis explores how zonal momentum exits the Southern Ocean, and how its path from source to sink shapes the Meridional Overturning Circulation (Figure 1.1), whose upwelling branch in the Southern Ocean forms a key exchange of carbon and heat between the atmosphere and the deep ocean (Marshall and Speer, 2012).

The first part of the thesis employs the Southern Ocean State Estimate (Mazloff et al., 2010), an eddy-permitting, data-assimilating model of the Southern Ocean south of 24.7°S, to diagnose the overall sources and sinks of zonal momentum. Wind stress provides an obvious source of eastward momentum; the analysis in Chapter Two shows that topographic form stress, by which momentum exits the fluid by 'leaning' on submerged ridges that block the ACC's flow, balances almost all of this input momentum. The idea that topographic form stress might serve as a unique balance for wind stress

in the ACC is not a new one; Munk and Palmén (1951) first posited the idea more than 60 years ago, and numerous numerical experiments and general circulation model analyses have shown that topographic form stress plays a primary role in the Southern Ocean zonal momentum budget. Chapter Two builds on these previous analyses by mapping the topographic form stress field, demonstrating that nearly all wind stress can be balanced by topography shallower than 3700 m, and that nearly half of wind stress is balanced by form stress across the South American landmass, rather than the submerged ridges.

In the third chapter, we apply the methods developed in the previous chapter to determine the structure of the mechanism that carries momentum from wind stress source to topographic sink, called interfacial form stress. Directly analogous to topographic form stress, interfacial form stress occurs when a lighter fluid layer 'leans' against a vertical perturbation in a heavier fluid layer below. We decompose the meridional overturning circulation in the Southern Ocean State Estimate according to transport forced by wind stress, by topographic form stress, and by interfacial form stress, isolating the interfacial form stress term for the first time in a general circulation model.

Finally, we ground-truth these findings in Chapter Four using an observational dataset from the cDrake experiment, a four-year deployment of current and pressure recording inverted echo sounders along a standing frontal meander in the northern Drake Passage. We compare the cDrake experiment results to previous observational estimates in the region, and to the Drake Passage region of the SOSE model interfacial form stress field.

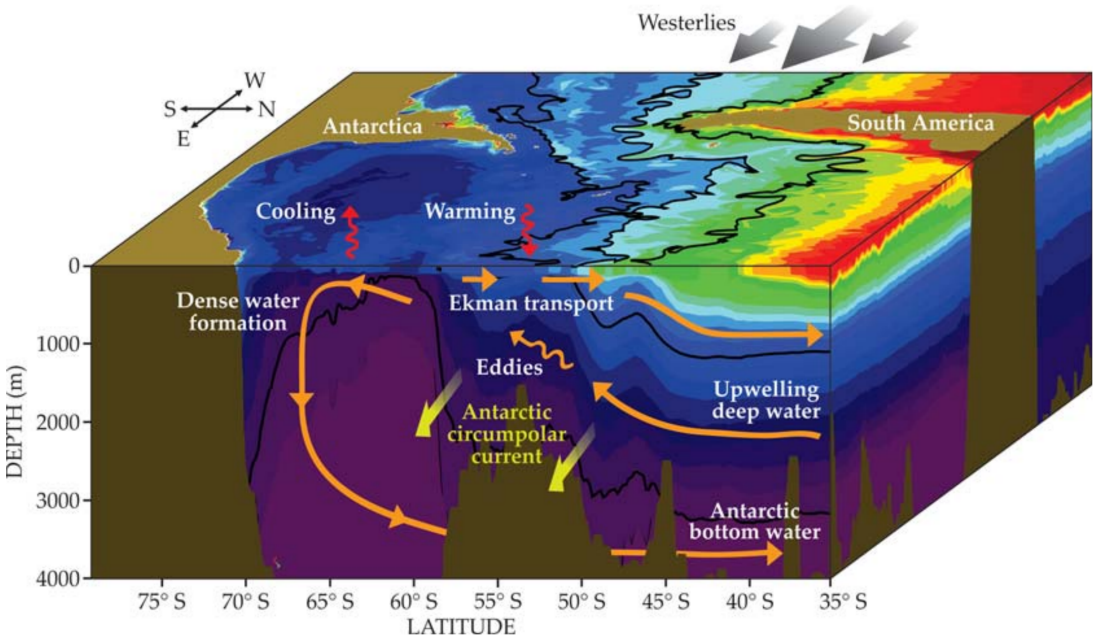

Figure 1.1: Dynamics in the Southern Ocean, reproduced from Morrison et al. (2015). Westerly winds drive the ACC east, and drive a northward surface Ekman layer. Combined with surface buoyancy forcing, this Ekman transport causes deep water to upwell towards the pole, tilting isopycnals (shown in the colors) upwards towards the south. Brine rejection and cooling near the Antartic coast forms dense Antarctic bottom water, which sinks and returns northward.

Chapter 2

Topographic form stress in the Southern Ocean State Estimate

Key points

1. Topographic form stress balances 95% of Southern Ocean wind stress
2. Shallow form stress in the top 3700 m balances most of the wind stress
3. Approximately 40% of wind stress is balanced by form stress across land, 60% by submerged ridges

Abstract

We diagnose the Southern Ocean momentum balance in a six-year, eddy permitting state estimate of the Southern Ocean. We find that 95% of the zonal momentum input via wind stress at the surface is balanced by topographic form stress across ocean ridges, while the remaining 5% is balanced via bottom friction and momentum flux divergences at the northern and southern boundaries of the analysis domain. While the time-mean zonal wind stress field exhibits a relatively uniform spatial distribution, time-

mean topographic form stress concentrates at shallow ridges and across the continents that lie within the Antarctic Circumpolar Current (ACC) latitudes; nearly 40% of topographic form stress occurs across South America, while the remaining 60% occurs across the major submerged ridges that underlie the ACC. Topographic form stress can be divided into shallow and deep regimes: the shallow regime contributes most of the westward form stress that serves as a momentum sink for the ACC system, while the deep regime consists of strong eastward and westward form stresses that largely cancel in the zonal integral. The time-varying form stress signal, integrated longitudinally and over the ACC latitudes, tracks closely with the wind stress signal integrated over the same domain; at zero lag, 88% of the variance in the six-year form stress time series can be explained by the wind stress signal, suggesting that changes in the integrated wind stress signal are communicated via rapid barotropic response down to the level of bottom topography.

2.1 Introduction

Strong, persistent winds over the Southern Ocean drive the Antarctic Circumpolar Current (ACC) on an unblocked eastward path around Antarctica. In a closed ocean basin, continental barriers support a western boundary current structure that balances the momentum input by wind stress; lacking any zonal bounds, the ACC must balance wind stress via other means. While momentum input into the Southern Ocean can be estimated via satellite observations of surface winds, mechanisms for how momentum exits the system are more difficult to observe. Observations and reanalyses have shown an increase in the strength of Southern Ocean wind stress (Thompson and Solomon, 2002; Swart and Fyfe, 2012), while the ACC baroclinic transport appears to remain stable (Böning et al., 2008), suggesting that the interior mechanisms that remove momentum

from the ACC system are counterbalancing changes in the input wind stress. Here we describe where and how momentum exits the ACC system in the Southern Ocean State Estimate (SOSE) model.

Munk and Palmén (1951) first proposed a momentum sink, uniquely important in the Southern Ocean, which might serve to balance the wind stress: form stress across bottom topography. Munk and Palmén estimated that the four tallest ridges under the ACC – the Kerguelen Plateau, Macquarie Ridge, Scotian Arc, and East Pacific Rise – could provide enough zonal pressure gradient across each ridge to balance the wind stress in the zonal mean. We evaluate Munk and Palmén's conjecture by mapping all momentum sources and sinks in the SOSE Southern Ocean between 30°S and 77°S; these maps confirm the broad strokes of their theory but reveal a more complex structure.

2.2 Background

The Southern Ocean State Estimate (SOSE) is a $1/6$-degree, eddy-permitting model of the Southern Ocean. Based on the MITgcm, SOSE employs an iterative adjoint method to perform a least squares fit to observational data from myriad sources, including satellite altimetry and sea surface temperature observations, CTD data from the Argo program and various other observational programs, and bottom pressure and acoustic travel time data from Inverted Echo Sounder experiments. SOSE is constrained by the 1-degree Ocean Comprehensible Atlas (OCCA) world ocean state estimate at its northern boundary at 24.7°S, and by European Center for Medium-Range Weather Forecast reanalysis interim atmospheric model data at the ocean surface (Mazloff et al., 2010). Bottom topography in the SOSE model comes from Smith and Sandwell and the Earth Topography Five-Minute Grid; these datasets are binned to a $1/4$-degree resolution, and then interpolated to the $1/6$-degree SOSE grid (Figure 2.6a). The model has

42 depth levels, with resolution ranging from 10 m at the surface to 250 m at depth. Overall, the SOSE model represents the observed Southern Ocean reasonably well; the 2005-2006 solution better represented the observational data available during that time than did the World Ocean Atlas 2001 climatology (Mazloff et al., 2010). The current model run, spanning 2005 through 2010, assimilates more observational data than this 2005-2006 solution. SOSE's unique combination of eddy-permitting model physics with observational data represents the best possible guess at otherwise unobservable Southern Ocean characteristics, including the basin-scale topographic form stress signal.

The zonally and vertically integrated zonal momentum equation reduces to four terms (see Appendix A):

$$\rho_0 \oint_x \frac{\partial}{\partial y} \int_{z=-H}^{\overline{\eta}} \overline{uv} \mathrm{dzdx} = -\oint_x \int_{z=-H}^{\overline{\eta}} \frac{\partial \overline{p}}{\partial x} \mathrm{dzdx} + \oint_x \overline{\tau^x_{wind}} \mathrm{dx} - \oint_x \overline{\tau^x_{friction}} \mathrm{dx}, \qquad (2.1)$$

where the overbars denote the time mean, ρ_0 is background seawater density, η is the sea surface height, $-H$ is the depth at the seafloor, u is zonal velocity, v is meridional velocity, p is pressure, τ^x_{wind} is zonal wind stress at the surface, and $\tau^x_{friction}$ is zonal stress due to bottom and sidewall friction.

The four terms in equation (1)– from left, meridional momentum flux divergence, topographic form stress contained within the pressure gradient term, wind stress, and bottom friction – form the primary ACC balance in the zonal and depth integral. Eastward momentum from wind stress is the main source of momentum sustaining the ACC, but all three remaining terms can contribute to the westward momentum that balances this term.

Time-mean depth-integrated fields of each term in equation (1) give us an initial sense of what terms may be most important in the momentum balance (Figure 2.1);

while the bottom friction, wind stress, and flux divergence terms are of the same magnitude, the zonal pressure gradient term is an order of magnitude larger. Flux divergence, bottom friction, and pressure gradient fields change sign frequently throughout the domain, while wind stress remains steadily positive over most of the Southern Ocean; thus in the zonal integral, we can expect the wind stress to be large while the bottom friction and advection terms will be smaller. The subset of the pressure gradient field that involves pressure gradients across topography (water leaning on land) is overwhelmed by the pressure gradients in the ocean interior (water leaning on water), but only the pressure gradients across topography contribute to the zonally integrated momentum balance. Extraction of the topographic form stress field from the total zonal pressure gradient field is described in the Methods section below.

Previous numerical studies have confirmed that in the zonal integral, wind stress is primarily balanced by topographic form stress. McWilliams et al. (1978), Treguier and McWilliams (1990), Wolff et al. (1991) and Marshall et al. (1993) have shown that topographic form stress balances wind stress in simple two- and three- layer quasi-geostrophic channel models. More recently, Ward and Hogg (2011) used a five-layer rotating wind-driven channel model to show that while bottom friction and northward transport tend to balance wind stress during spin-up, topographic form stress balances wind stress once the model reaches equilibrium. Howard et al. (2015) used a similar three-layer channel model, this time with both buoyancy forcing and wind forcing, to show that while bottom friction balances the buoyancy forcing at equilibrium, it is topographic form stress that balances the wind stress forcing.

The zonal integral has also been explored in high resolution general circulation models as well; in the $1/2$-degree by $1/4$-degree, 32-level Fine Resolution Antarctic Model (FRAM), topographic form stress was shown to balance wind stress in the zonal average in the unblocked latitudes by Killworth and Nanneh (1994) and Stevens and

Ivchenko (1997), and along streamlines in the ACC latitudes by Ivchenko et al. (1996). Grezio et al. (2005) showed that topographic form stress balances wind stress in the zonal mean in both the $1/4$-degree, 36-level OCCAM project model and the 20-level Parallel Ocean Program (POP) model as well, with a small but significant contribution from eddy flux divergence in both models.

To our knowledge, only Gille (1997) has investigated the zonal structure of the topographic form stress signal in a model with realistic topography. Using the 0.4-degree, 20-level Semtner-Chervin model for latitudes spanning 30°S to 70°S, Gille (1997) found that topographic form stress balanced wind stress at all latitudes in the domain.

Gille (1997) approached the difficult problem of extracting the topographic form stress signal from the full zonal pressure gradient field by dividing the ACC longitudinally into 10-degree sectors, and taking the difference between the geostrophic transport that would be driven by the zonal pressure gradient across the sector and the actual geostrophic transport observed through the sector. The residual between the two signals was attributed to a pressure gradient across topography in the sector, and Gille (1997) was able to show that topographic form stress acts as a momentum sink primarily at three locations along the ACC: Kerguelen and Campbell Plateaus, and the Drake Passage. The results using this method, however, are sensitive to the choice of longitudinal sectors, and may neglect contributions to the form stress signal that come from pressure gradients across topography that is wider than the 10-degree sector size.

Using the observationally-constrained SOSE model from 30°S to 77°S, we take a more direct approach, calculating the pressure gradient across every piece of topography in the domain rather than taking longitudinal sections. We find that in the ACC latitudes 42°S to 65°S, 95% of the net integrated zonal wind stress is balanced by topographic form stress, while meridional momentum flux divergence and bottom/sidewall friction

together contribute only 5% of the westward momentum balance needed to balance the wind stress. Our results align with previous studies in that topographic form stress serves as the primary balance for wind stress, but our analysis reveals a complex structure for the topographic form stress field.

2.3 Methods

The zonal and depth integrated total zonal pressure gradient term can be written:

$$-\oint_x \int_{z=-H}^{\overline{\eta}} \frac{\partial \overline{p}}{\partial x} \mathrm{dzdx} = -\underbrace{\oint_x \frac{\partial}{\partial x} \int_{z=-H}^{\overline{\eta}} \overline{p} \mathrm{dzdx}}_{i} + \underbrace{\oint_x \overline{p_{atm}} \frac{\partial \overline{\eta}}{\partial x} \mathrm{dx}}_{ii} + \underbrace{\oint_x \overline{p_b} \frac{\partial H}{\partial x} \mathrm{dx}}_{iii}, \tag{2.2}$$

where $p_{atm} = p(z = \eta)$ is the atmospheric pressure at the surface, and $p_b = p(z = -H)$ is the bottom pressure at the seafloor. Term (i) in this equation is the net pressure gradient across a zonally bounded basin; Olbers (1998) notes that in a closed, flat-bottomed basin, this term alone would balance input wind stress over the basin. In the unblocked latitudes, term (i) vanishes, and term (ii) and term (iii) represent the transfer of zonal momentum from the atmosphere to the fluid via form stress and from the fluid to the solid earth via form stress, respectively. Term (ii) in this domain is negligibly small, but in the blocked latitudes, both term (i) and term (iii) contribute to the total form stress signal by denoting the transfer of zonal momentum from the fluid to the earth at the continental boundaries.

To capture all three contributions to the total form stress signal in the numerical model, we discretize the left-hand side of equation (2):

$$-\oint_x \int_{z=-H}^{\overline{\eta}} \frac{\partial \overline{p}}{\partial x} \mathrm{dzdx} = -\sum_x \sum_z \frac{\Delta p}{\Delta x} \Delta z \Delta x = -\sum_x \sum_z \Delta p \Delta z. \tag{2.3}$$

This term will reveal the topographic form stress signal, since only momentum transferred to the solid earth will remain in the full circumpolar integral. We refine this calculation in order to locate where these transfers occur.

To extract the topographic form stress signal from the overall pressure field, we first isolate all points in the 3D SOSE pressure field that lie adjacent to topography, $p_b = p(z = -H)$. Though SOSE employs partial cells, in which a fraction of the cell contains fluid and a fraction contains land, we simplify the topographic field so that Δz in this methodology is simply the height of the cell itself, which results in a small uncertainty (2% average, 5.2% maximum) in the integration depth over which the form stress is distributed. For every z-level and along every x-line on the SOSE grid that transects a given region of topography – a seamount, for instance – we calculate the form stress signal by first taking the pressure difference, east-minus-west, between the ocean cell adjacent to the eastern face of the seamount and the ocean cell adjacent to the western face (Figure 2.2):

$$\Delta\overline{p_b} = \overline{p_b}(x = x_E) - \overline{p_b}(x = x_W). \tag{2.4}$$

For all plots of the form stress field, we divide the pressure difference Δp_b by the width of the seamount Δx over which the pressure difference occurs (Figure 2.2b):

$$\frac{\Delta\overline{p_b}}{\Delta x} = \frac{\overline{p_b}(x = x_E) - \overline{p_b}(x = x_W)}{x_E - x_W}. \tag{2.5}$$

We vertically integrate these topographic pressure gradients to show the vertically integrated pressure gradient fields shown in Figures 2.2c, 2.4, and 2.7:

$$\sum_{z=-H}^{\overline{\eta}} \frac{\Delta\overline{p_b}}{\Delta x}\Delta z, \tag{2.6}$$

and we zonally integrate to find the total form stress signal:

$$-\oint_x \int_{z=-H}^{\overline{\eta}} \frac{\partial \overline{p}}{\partial x} \mathrm{dzdx} = \sum_{ridges} \sum_{z=-H}^{\overline{\eta}} \frac{\Delta \overline{p_b}}{\Delta x} \Delta z \Delta x = \sum_{ridges} \sum_{z=-H}^{\overline{\eta}} \Delta \overline{p_b} \Delta z, \tag{2.7}$$

where we have adopted Olbers et al. (2004)'s use of 'ridges' to denote both landmasses and submerged topography. The sign changes here because $\Delta \overline{p_b}$ is calculated across topography, rather than across the ocean basin bound by that topography. Only pressure differences across topography are included in the form stress signal, but every piece of topography – from small seamounts to continents to plains separating abyssal basins – is included in the calculation of the signal.

Finally, we note that in a flat-bottomed periodic ocean, the total pressure gradient $\partial p/\partial x$ must be zero when integrated zonally:

$$\oint_x \frac{\partial \overline{p}}{\partial x} \mathrm{dx} = 0. \tag{2.8}$$

In a periodic ocean interrupted by ridges, the zonally integrated total pressure gradient will be the sum of the pressure differences across those ridges, with opposite sign:

$$\oint_x \frac{\partial \overline{p}}{\partial x} \mathrm{dx} = -\sum_{ridges} \Delta \overline{p_b}. \tag{2.9}$$

We use this relationship to confirm our methodology by comparing the zonally integrated topographic form stress calculation to the zonal integral of the total pressure gradient. We find that the two integrated fields are indeed identical in magnitude, with opposite sign, at every latitude and every depth in the domain.

2.4 Results

2.4.1 Time mean momentum balance

In the 6-year SOSE mean, the total *xy*-integrated zonal wind stress is almost entirely balanced by topographic form stress. For the latitudes that border the northern and southernmost closed ACC transport stream lines, 42°S to 65°S, the time-mean total integrated eastward wind stress for the six-year SOSE run is 6.67×10^{12} N (Table 2.1). Total integrated topographic form stress contributes 6.36×10^{12} N net westward momentum (balancing 95% of the total wind stress); bottom and sidewall friction contributes 1.9×10^{11} N net westward momentum (balancing 3% of the wind stress); and momentum flux divergences at the meridional boundaries account for 1.6×10^{11} N net westward momentum (2%).

For the full domain 30°S to 77°S, these numbers are slightly different (Table 2.1). While the total integrated eastward wind stress is 8.03×10^{12} N, the total integrated westward topographic form stress is 7.30×10^{12} N (balancing 91% of the wind stress); bottom friction is 1.1×10^{11} N (balancing 1%); and momentum flux divergence across the 30°S boundary accounts for 6.1×10^{11} N (balancing 8%). Figure 2.3 shows that the zonally integrated topographic form stress not only balances wind stress in the total integral, but at every latitude as well.

When we move out of the zonally-integrated regime, the horizontal structure of the wind stress and topographic form stress fields diverge radically. Figure 2.4a shows the topographic form stress signal integrated over the full ocean depth. While the wind stress signal (Figure 2.1a) exhibits relatively little horizontal variation, the topographic form stress signal varies in both magnitude and sign.

Within the ACC latitudes, the most readily understood form stress signal is the strong westward (blue, Figure 2.4a) form stress that concentrates over South America

and the ridges that underlie the ACC – Kerguelen Plateau, the Southeast Indian Ridge, the Macquarie Ridge region, the southernmost portion of the East Pacific Rise, and the Phoenix and Shackleton Fracture Zones in the Drake Passage. More surprising is the presence of eastward (red, Figure 2.4a) form stress in the field, due to higher pressure on the east flank of topography than on the west flank. These positive zonal pressure gradients are perhaps less intuitive, since they imply an acceleration of the eastward ACC flow. Eastward topographic form stress in the ACC is not without precedent; Holloway (1987) noted that form stresses could act in the same direction as the mean flow in a simple QG model, and both Stevens and Ivchenko (1997) and Grezio et al. (2005), found in general circulation models that the deepest zonally integrated topographic form stress signals, though an order of magnitude smaller than the wind stress, acted eastward rather than westward. We attribute this net eastward deep form stress to pressure differences across the deepest ocean basins, discussed in section 2.4.3 below.

South and north of the ACC latitudes, the topographic form stress signals have little to do with ACC dynamics. South of the ACC latitudes, pressure differences between the subpolar gyres dominate the topographic form stress signal. Higher pressure in the eastern Weddell Sea than in the western Amundsen, Bellingshausen and Ross Seas causes a positive zonal pressure gradient across the Antarctic Peninsula, and a corresponding negative pressure gradient (blue, Figure 2.4a) across the rest of the Antarctic continent that separates them.

North of the ACC latitudes, pressure differences between the subtropical gyres similarly dominate the form stress signal. A positive zonal pressure gradient between the Indian and Pacific gyres and between the Atlantic and Indian gyres result in eastward form stress (red, Figure 2.4a) across Australia and Africa, respectively. A negative zonal pressure gradient between the Pacific and the Atlantic results in a strong westward form stress (blue, Figure 2.4a) across South America that extends into the ACC latitudes,

discussed in Section 2.4.2 below.

2.4.2 Shallow and deep contributions to topographic form stress

A few previous studies have noted the presence of two depth regimes in topographic form stress. Stevens and Ivchenko (1997) noted two separate 'deep' (2056 m to 3874 m) and 'very deep' (3874 m to 5499 m) regimes in FRAM's zonal mean topographic form stress signal. In the deep regime, the authors found that topographic form stress was of the same order of magnitude as the wind stress. In the very deep regime, they found that the zonal mean topographic form stress had the same sign as the wind stress – implying an average pressure gradient that would act to accelerate, rather than decelerate the ACC flow – and was an order of magnitude smaller. Grezio et al. (2005) noted a similar division in the mean form stress signal between deep (3722 m to 4989 m) and very deep (4989 m to 5500 m) regimes in OCCAM; topographic form stress was of the same order of magnitude as wind stress in the deep regime, but an order of magnitude smaller in the very deep regime. These authors too noted that at some latitudes, the sign of the topographic form stress in the very deep regime was the same as the wind stress.

In SOSE, as well, the integrated topographic form stress can be divided into two regimes: shallower and deeper than 3700 m. Figure 2.4 shows the vertically integrated topographic form stress field (Figure 2.4a), along with the shallow regime integrated from the surface to $z = -3700$ m (Figure 2.4b) and the deep regime from $z = -3700$ m to the seafloor (Figure 2.4c). The topographic form stress signal integrated from the surface to 3700 m resembles the Munk and Palmén paradigm; within the ACC latitudes, primarily westward topographic form stress concentrates over large-scale bottom topography, along with South America. The form stress signal integrated from 3700 m to depth reveals a large-scale structure that tends to cancel in the zonal integral.

For all three fields, the vast majority ($> 99\%$) of the individual topographic form stress signals fall between -2 and 2 N/m^2, an order of magnitude larger than the wind stress signal. Distributions of form stress signals (Figure 2.4, right) for both the shallow regime and the deep regime are narrowly distributed around their respective means, with a few outliers occurring in regions of very narrow ridges such as Macquarie Ridge, where a very small Δx serves to magnify the pressure difference across the ridge.

The degree to which the shallow regime balances the wind stress varies with both latitudinal and depth bounds (Figure 2.5). For the full Southern Ocean domain (30°S to 77°S), the shallow form stress regime balances the wind stress with a bottom bound closer to $z = -3300$ m, and shows very little variability when the latitudinal bounds are slightly narrowed. For ACC latitudes 42°S to 65°S, the shallow topographic form stress regime bound by $z = [-3700 \text{ m}, \overline{\eta}]$ balances 101% of the wind stress in the total integral. Shallow regimes bound at deeper depths tend to overshoot the wind stress signal, until the balance returns to 100% with a bottom bound of approximately $z = -4500$ m, finally reaching 95% of wind stress balanced when the full z domain is included.

For the unbounded latitudes 56°S to 62°S, the balance between shallow form stress and wind stress is relatively poor; only 66% of the wind stress is balanced by a shallow regime bound by $z = [-3700 \text{ m}, \overline{\eta}]$, and only 92% of the wind stressed is balanced when the full z domain is included. Changing the bounds of the latitudinal domain results in significant variability in the amount of wind stress balanced by form stress, ranging from 33% to 146% over the full z domain. This large range reflects the importance of including continents in the form stress calculation; the inclusion of portions of South America and/or the Antarctic Peninsula in the latitudinal domain results in a large variation in the size of the integrated form stress signal.

2.4.3 Shallow ridges

Figure 2.6 reveals the most significant contributors to the shallow topographic form stress signal in the ACC latitudes 42°S to 65°S (Table 2.2): the cumulative zonal integral takes the shape of a step function that decreases at the ridges that contribute the most to the integrated form stress signal. Table 2.1 lists these major contributors, and Figure 2.7 zooms in to their locations. From west, Kerguelen Plateau (Figure 2.7b) contributes 13% of the total westward form stress in the ACC latitudes; the Southeast Indian Ridge/Macquarie Ridge/Campbell Plateau region (Figure 2.7c) contributes 20%; the Drake Passage/South America region (Figure 2.7e) contributes nearly half of the total form stress, at 42%; and there are smaller contributions from the East Pacific Rise (3%; Figure 2.7d)) and Mid-Atlantic Ridge (4%; not pictured) that are less obvious in the cumulative integral shown in Figure 2.6.

For most of the ACC's path, only undersea ridges contribute to the shallow topographic form stress signal. Form stress across South America, though, plays a key role in the overall momentum balance in the ACC latitudes. Net westward form stress across South America not only dwarfs the form stress across the Drake Passage fracture zones, but constitutes 40% of the total westward topographic form stress signal.

2.4.4 Deep density dipole

The deep regime, dominated by large zonal pressure gradients that span thousands of kilometers, tends to cancel in the zonal integral. The deep regime depends on pressure differences across deep abyssal ocean basins that are often separated not only by the large shallow ridges, but also by long expanses of deeper plains. The deep form stress signal depends on a zonal dipole in the pressure in these deep abyssal basins: higher pressure in the deep basins underlying the Atlantic and Indian sectors of the

Southern Ocean, and lower pressure in the deep basins underlying the Pacific sector (Figure 2.8). A comparison of deep enclosed basins along a latitudinal circle – Enderby Basin to Amundsen Basin to Weddell Basin, for instance – reveals a denser-lighter-denser pattern of Antarctic Bottom Water (Figure 2.8a), and an associated pattern of higher-lower-higher deep pressure (Figure 2.8b).

From the Indian to the Pacific sector, the high-to-low pressure gradient between the deep basins results in westward form stress (blue, Figure 2.8c) across the deep plains. From the Pacific to the Atlantic sector, the low-to-high pressure gradient between the deep basins results in an eastward form stress (red, Figure 2.8c) across the plains. This deep density dipole thus creates a deep topographic form stress regime that, regionally, can result in a very large eastward or westward form stress, but largely cancels in the zonal integral.

2.4.5 Time variability

Thus far we have focused on the spatial structure of the six-year time-mean momentum balance only. Integrating the time-varying wind stress and form stress over all longitudes and the ACC latitudes allows us to evaluate the time variability of the overall input and output momentum signals in the ACC. Figure 2.9a shows the wind stress and topographic form stress five-day averaged time series, where the wind stress has been inverted to track with the topographic form stress.

There is little lag between the form stress signal and the wind stress signal. The wind stress signal explains 88% of the variance in the form stress signal at zero lag, with a quick drop off below zero variance explained at a 15-day lag (Figure 2.9b). This high variance explained at zero lag suggests a rapid barotropic response in the ACC system to changes in wind stress, an effect noted by Hughes et al. (1999) via comparisons of wind stress and ACC transport, and explored via theoretical and modeling efforts byWebb and

De Cuevas (2006), Zika et al. (2013), Ward and Hogg (2011), Thompson and Naveira Garabato (2014) and others.

Figure 2.10a shows that the variability in the integrated topographic form stress signal concentrates over topography that lies beneath the ACC fronts. Topography close to the vigorously eddying Agulhas region shows some of the largest standard deviation, along with regions of narrow topography that act as gates across the ACC's path, like Macquarie Ridge and the Drake Passage fracture zones. Even small seamounts and fracture zones in the plains that underlie the ACC frontal paths show a high variance, especially in the Indian Ocean between Kerguelen Plateau and the Southeast Indian Ridge. In regions where the ACC flows around – rather than over and through – the barrier, such as the Campbell Plateau and South America, the variance is much lower, even though these regions contribute a large portion of the time-mean zonally integrated form stress signal.

We check that the state estimation procedure is not favorably adjusting the wind stress field over these regions of high form stress variation by mapping the SOSE wind stress adjustment fields – the difference between the ERA-Interim wind stress data and the SOSE wind stress fields at each time step. We find that there is no correlation between the wind stress adjustment fields and the continents or undersea ridges. Instead, adjustment to the ERA-Interim wind stress data in the ACC latitudes are modest and somewhat homogenous (Figure 2.10b), with SOSE adjustment variance smaller than 5% of the ERA-Interim variance at most locations in the ACC latitudes. Lag correlation between the ERA-Interim wind stress signal and the form stress signal shows that the ERA-Interim wind stress explains 80% of the variance in the form stress signal at zero lag, with a similarly quick drop off below zero variance explained at a 15-day lag. This tells us that this high zero-lag correlation must have a dynamical explanation rather than being a model artifact.

2.5 Conclusions

We have shown that the SOSE momentum balance aligns with previous channel and general circulation model findings: in the zonal integral, topographic form stress acts as the primary balance for wind stress over the Southern Ocean. SOSE's 4D fields have allowed us to look at the spatial and temporal structure that contributes to this net westward form stress signal, and we can confirm Munk and Palmén (1951)'s original theory and Gille (1997)'s finding that the shallow ridges underlying the ACC serve as the primary locations of the westward form drag that balances wind stress.

By mapping the topographic form stress, we have quantified the relative role of the topography that contributes to the overall zonally integrated momentum balance. We find that while the expected submerged ridges do play an important role in the momentum balance, it is South America that plays the most important role, contributing nearly half of the total topographic form stress signal. We also find that the Southeast Indian Ridge contributes to the signal, while the Scotia Arc, located south of much of the ACC flow, contributes little to the total time-mean form stress signal.

We have also characterized two separate deep and shallow form stress regimes – the shallow, wherein undersea ridges and South America combine to balance the wind stress, and the deep, wherein large local form stresses ultimately balance in the zonal integral. The presence of the deep regime helps to explain the small westward form stress found in the deepest parts of the zonally integrated signal calculated in FRAM (Stevens and Ivchenko, 1997) and OCCAM (Grezio et al., 2005); these signals are small because they are residuals of two large westward and eastward deep form stress signals, and they are net positive because the positive form stress between the Pacific and the Indo/Atlantic basins slightly outweighs the negative form stress between the Indo/Atlantic and Pacific basins. We attribute this deep basin density dipole to the

greater presence of denser Antarctic Bottom Water in the deep Atlantic and Indian basins than in the deep Pacific basins.

Finally, the integrated form stress variance explained by the integrated wind stress signal peaks at time lag less than 5 days, suggesting that changes in the wind stress are translated rapidly down to the level of bottom topography. At the same time, this analysis makes clear that momentum must be carried a significant distance not only vertically, but horizontally as well, before it can exit the ACC system. The mechanisms that transport momentum from source to sink are the focus of our future efforts.

2.6 Acknowledgments

SOSE data are available at sose.ucsd.edu. This work was supported by National Science Foundation grants PLR-11419122 and PLR-0961218. J. Masich was also supported by the Department of Defense through the National Defense Science & Engineering Graduate Fellowship Program. Thanks to Sarah Gille and C. S. Jones for useful discussion, and to two anonymous reviewers for their insightful comments.

Chapter Two, in full, is a reprint of the material as it appears in the Journal of Geophysical Research: Oceans, 2015. Masich, J., T. K. Chereskin, and M. R. Mazloff (2015), Topographic form stress in the Southern Ocean State Estimate, *J. Geophys. Res. Oceans*, 120, 7919-7933, doi:10.1002/2015JC011143. The dissertation author was the primary investigator and author of this paper.

2.A Zonal and depth integrated ACC momentum balance

Assuming steady state and applying the continuity equation, the time-mean zonal momentum equation can be written:

$$\rho_0 \frac{\partial}{\partial x}(\overline{uu}) + \rho_0 \frac{\partial}{\partial y}(\overline{uv}) + \rho_0 \frac{\partial}{\partial z}(\overline{uw}) - \rho_0 f \overline{v} = -\frac{\partial \overline{p}}{\partial x} + \frac{\partial \overline{\tau^x}}{\partial z} + \rho_0 \mu \nabla^2 \overline{u}, \tag{2.10}$$

where (u, v, w) are velocities in the (x, y, z) directions, ρ_0 is background seawater density, f is the Coriolis parameter, p is pressure, τ^x is zonal stress, μ is kinematic viscosity, and the overbar indicates the time mean.

Following Stevens and Ivchenko (1997), Johnson and Bryden (1989), and others, we take the circumpolar zonal integral and the vertical integral from seafloor $z = -H(x,y)$ to sea surface $z = \overline{\eta}(x,y)$, yielding:

$$\begin{aligned} \rho_0 \underbrace{\oint_x \int_{z=-H}^{z=\overline{\eta}} \left[\frac{\partial}{\partial x}(\overline{uu}) + \frac{\partial}{\partial y}(\overline{uv}) + \frac{\partial}{\partial z}(\overline{uw}) \right] \mathrm{dzdx}}_{A} \\ = -\oint_x \int_{z=-H}^{z=\overline{\eta}} \frac{\partial \overline{p}}{\partial x} \mathrm{dzdx} + \underbrace{\oint_x \int_{z=-H}^{z=\overline{\eta}} \frac{\partial \overline{\tau^x}}{\partial z} \mathrm{dzdx}}_{B}, \end{aligned} \tag{2.11}$$

where we have neglected the small integrated Coriolis and interior viscosity terms.

Integrating the flux divergence term (A), we have:

$$\oint_x \int_{z=-H}^{z=\overline{\eta}} \left[\frac{\partial}{\partial x}(\overline{uu}) + \frac{\partial}{\partial y}(\overline{uv}) + \frac{\partial}{\partial z}(\overline{uw}) \right] \mathrm{dzdx} = \tag{2.12}$$

$$\oint_x \left[\frac{\partial}{\partial x} \int_{z=-H}^{z=\overline{\eta}} \overline{uu}\mathrm{dz} - (\overline{uu})\Big|_{z=\overline{\eta}} \frac{\partial \overline{\eta}}{\partial x} - (\overline{uu})\Big|_{z=-H} \frac{\partial H}{\partial x} \right.$$

$$+ \frac{\partial}{\partial y} \int_{z=-H}^{z=\overline{\eta}} \overline{uv}\mathrm{dz} - (\overline{uv})\Big|_{z=\overline{\eta}} \frac{\partial \overline{\eta}}{\partial y} - (\overline{uv})\Big|_{z=-H} \frac{\partial H}{\partial y}$$

$$\left. + (\overline{uw})\Big|_{z=\overline{\eta}} - (\overline{uw})\Big|_{z=-H} \right] \mathrm{dx}.$$

The first term on the right hand side disappears in the circumpolar zonal integral. Noting that $w|_{\overline{\eta}} = u|_{\overline{\eta}} \frac{\partial \overline{\eta}}{\partial x} + v|_{\overline{\eta}} \frac{\partial \overline{\eta}}{\partial y}$, and $w|_{-H} = -u|_{-H} \frac{\partial H}{\partial x} - v|_{H} \frac{\partial H}{\partial y}$ and neglecting Stoke drift, we rewrite this equation as:

$$\oint_x \int_{z=-H}^{z=\overline{\eta}} \left[\frac{\partial}{\partial x}(\overline{uu}) + \frac{\partial}{\partial y}(\overline{uv}) + \frac{\partial}{\partial z}(\overline{uw}) \right] \mathrm{dzdx} = \tag{2.13}$$

$$\oint_x \left[-(\overline{uu})\Big|_{z=\overline{\eta}} \frac{\partial \overline{\eta}}{\partial x} - (\overline{uu})\Big|_{z=-H} \frac{\partial H}{\partial x} \right.$$

$$+ \frac{\partial}{\partial y} \int_{z=-H}^{z=\overline{\eta}} \overline{uv}\mathrm{dz} - (\overline{uv})\Big|_{z=\overline{\eta}} \frac{\partial \overline{\eta}}{\partial y} - (\overline{uv})\Big|_{z=-H} \frac{\partial H}{\partial y}$$

$$\left. + (\overline{uu})\Big|_{z=\overline{\eta}} \frac{\partial \overline{\eta}}{\partial x} + (\overline{uv})\Big|_{z=\overline{\eta}} \frac{\partial \overline{\eta}}{\partial y} + (\overline{uu})\Big|_{z=-H} \frac{\partial H}{\partial x} + (\overline{uv})\Big|_{z=-H} \frac{\partial H}{\partial y} \right] \mathrm{dx}.$$

Canceling terms, the final form for the vertically and zonally integrated flux divergence term is simply:

$$\oint_x \frac{\partial}{\partial y} \int_{z=-H}^{\overline{\eta}} (\overline{uv})\mathrm{dzdx}. \tag{2.14}$$

We now expand the stress term (B) into wind stress at the surface of the fluid, τ^x_{wind}, and frictional stress at the bottom and sidewalls of the fluid, $\tau^x_{friction}$. Evaluating the depth integral, this term becomes:

$$\oint_x \int_{z=-H}^{\overline{\eta}} \frac{\partial \overline{\tau^x}}{\partial z} \mathrm{dzdx} = \oint_x [\overline{\tau^x_{wind}} - \overline{\tau^x_{friction}}] \mathrm{dx}. \tag{2.15}$$

Combining terms (A) and (B) with the pressure gradient term, we have the time-mean zonally and vertically integrated zonal momentum equation:

$$\rho_0 \oint_x \frac{\partial}{\partial y} \int_{z=-H}^{\overline{\eta}} \overline{uv} \mathrm{dzdx} = -\oint_x \int_{z=-H}^{\overline{\eta}} \frac{\partial \overline{p}}{\partial x} \mathrm{dzdx} + \oint_x \overline{\tau^x_{wind}} \mathrm{dx} - \oint_x \overline{\tau^x_{friction}} \mathrm{dx}. \tag{2.16}$$

Table 2.1: *xyz*-integrated momentum terms. Positive sign indicates eastward direction; negative sign indicates westward direction.

y **domain**	**Wind stress**	**Topographic form stress**	**Frictional stress**	**Flux divergence**
ACC latitudes 42°S to 65°S	6.67×10^{12} N (+100%)	-6.36×10^{12} N (-95%)	-0.19×10^{12} N (-3%)	-0.16×10^{12} N (-2%)
Full domain 30°S to 77°S	8.03×10^{12} N (+100%)	-7.30×10^{12} N (-91%)	-0.11×10^{12} N (-1%)	-0.61×10^{12} N (-8%)

Table 2.2: Principle contributors to the shallow form stress signal over ACC latitudes 42° S to 65° S.

Location	**Percent contributed to total westward shallow form stress signal**
Kerguelen Plateau	13%
Southeast Indian Ridge / Macquarie Ridge / Campbell Plateau region	20%
East Pacific Rise	3%
South America and Drake Passage	42%
Mid-Atlantic Ridge	4%

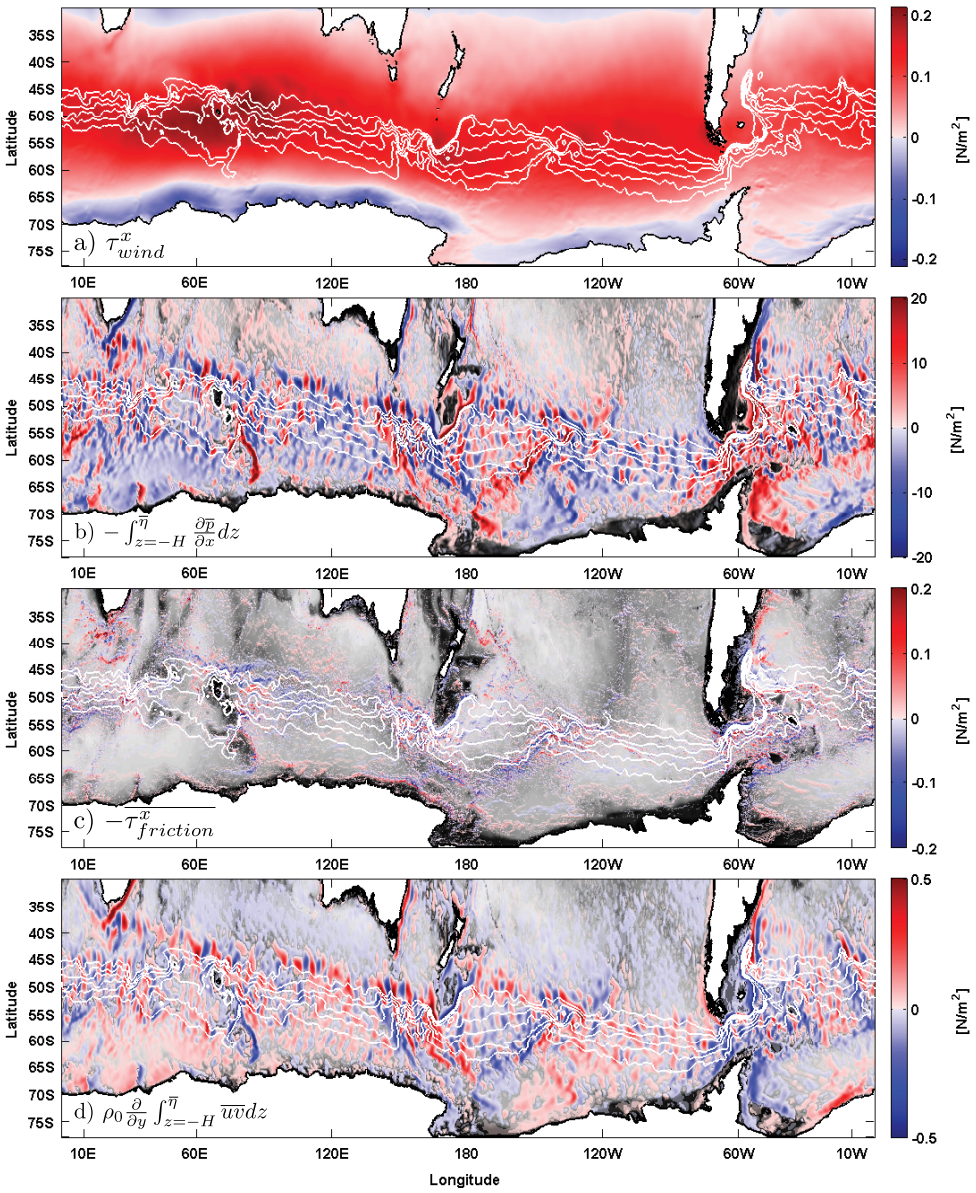

Figure 2.1: Vertically integrated six-year time mean momentum balance terms: (a) wind stress; (b) vertically integrated zonal pressure gradient; (c) bottom and sidewall friction; (d) meridional momentum flux divergence. White lines show SOSE ACC streamlines.

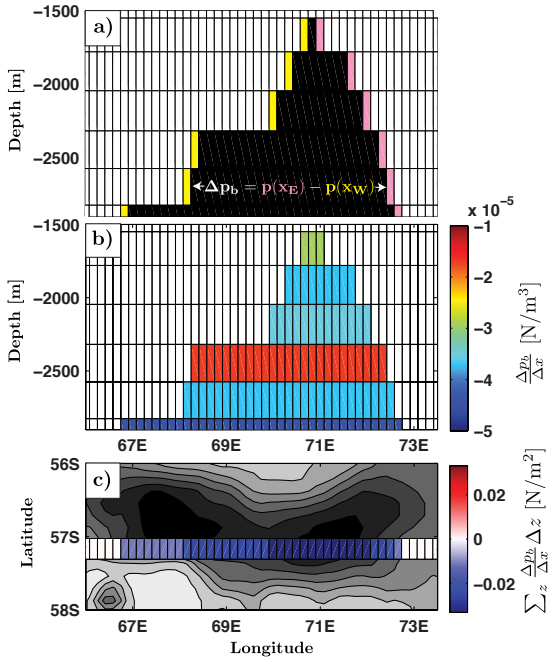

Figure 2.2: (a) Consider a zonal slice through a seamount south of Kerguelen Plateau: white cells indicate areas that contain water, black cells indicate areas that contain land. Pressure on the westward flank (yellow) is subtracted from the pressure on the eastward flank (pink). (b) The pressure difference is divided by the width of the seamount that separates the cells, and this pressure gradient $\Delta p_b/\Delta x$ is assigned to each z-level on the seamount. (c) Pressure gradients at each vertical level are integrated vertically to calculate the form stress field. Zonally integrating this field yields the total vertically and zonally integrated form stress signal.

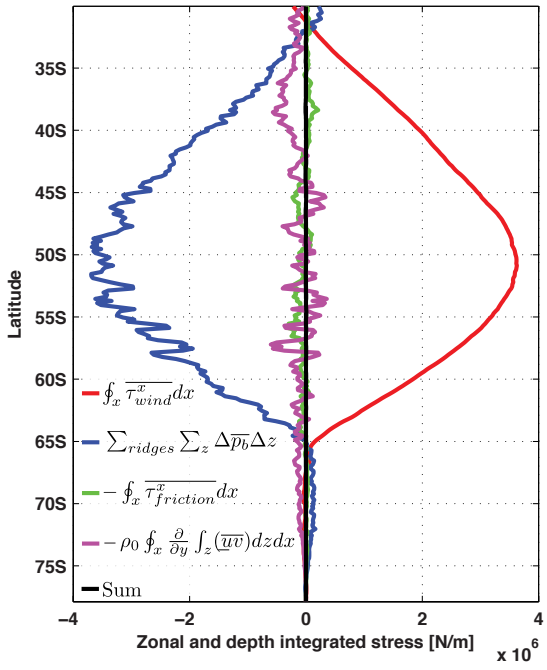

Figure 2.3: Zonal and depth integrated stress terms between 30° S and 77° S. Integrated bottom and sidewall friction (green) and momentum flux divergence (magenta) terms are relatively small at all latitudes. Integrated wind stress (red) is large between 32° S and 65° S, and integrated topographic form stress (blue) is similarly large at these latitudes, balancing wind stress. The black line shows the sum of these terms, demonstrating that these four terms encompass the full zonal and depth integrated momentum balance.

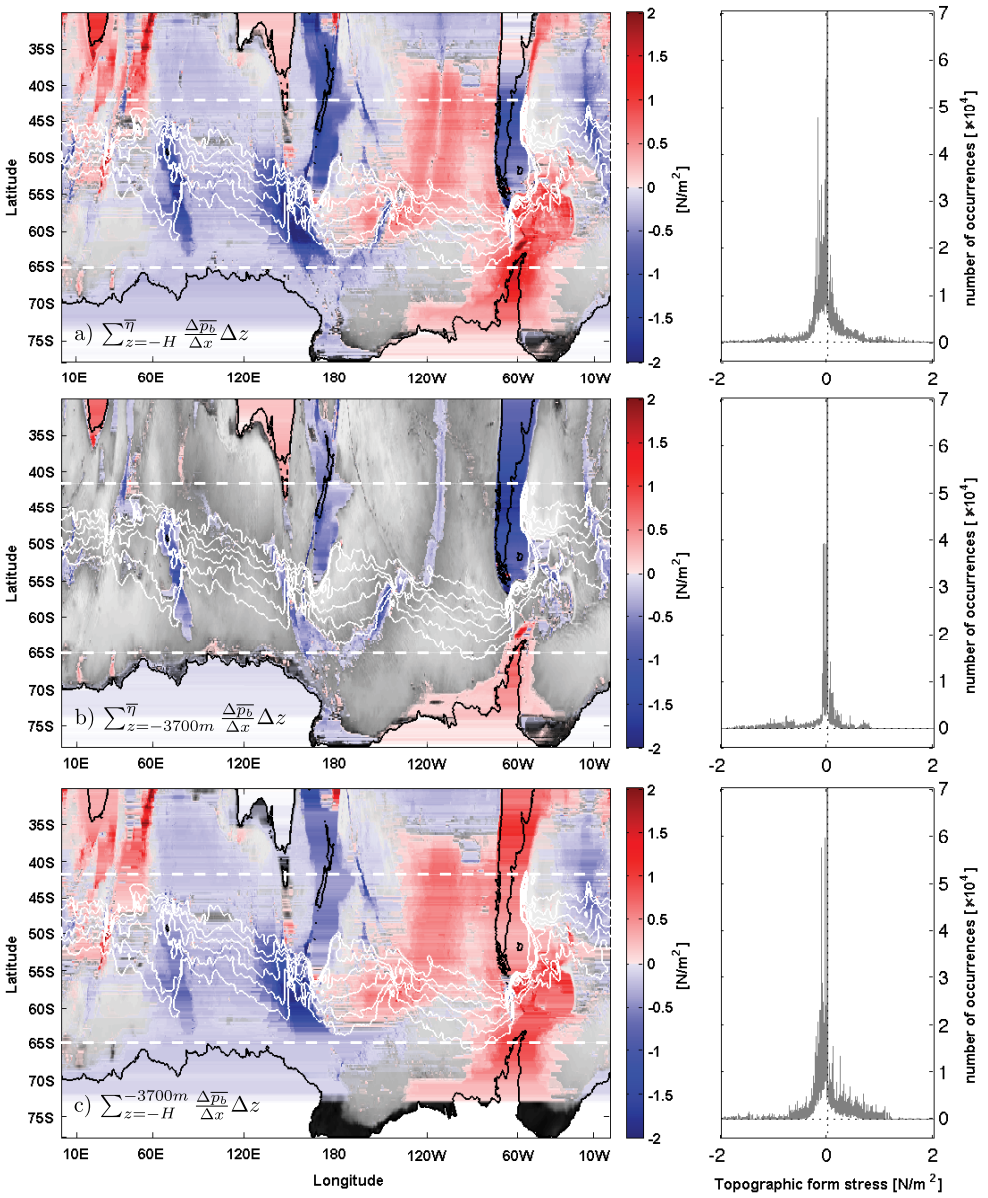

Figure 2.4: Vertically integrated six-year time mean topographic form stress fields (left) and associated histograms (right), for: (a) full depth, (b) from surface to z= -3700 m, and (c) from z= -3700 m to the seafloor. Solid white lines show SOSE ACC streamlines. Dashed white lines show the limits of the ACC latitudes.

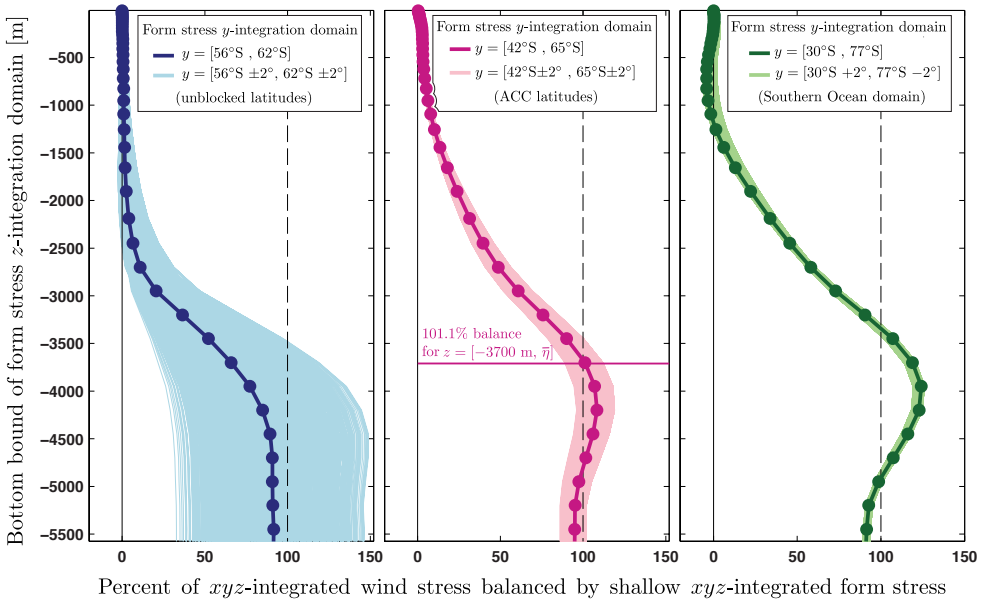

Figure 2.5: Percent of wind stress balanced by topographic form stress integrated from $z = \overline{\eta}$ to various depths, and over the unblocked latitudes (left), the ACC latitudes (center), and the full Southern Ocean domain (right). The division between the 'shallow' form stress regime and 'deep' form stress regime for the ACC latitudes is marked at $z = -3700$ m.

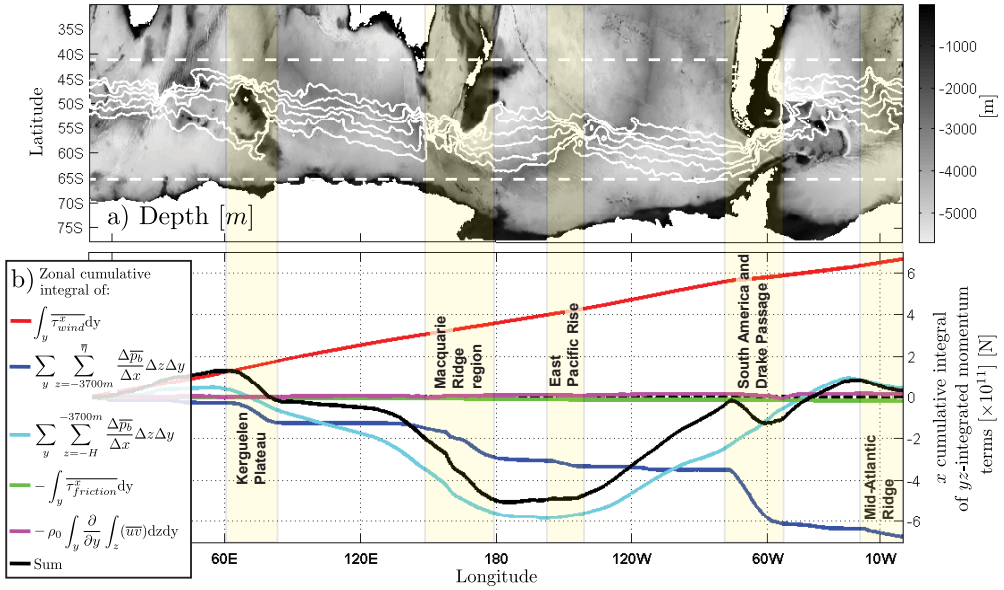

Figure 2.6: (a) SOSE bathymetry with important regions shaded in yellow, ACC streamlines shown in white, and ACC latitudinal bounds marked by dotted white lines. (b) Zonal cumulative integral of *y*-*z* integrated momentum terms between ACC latitudes 42°S and 65°S. Deep topographic form stress (light blue) decreases and then increases, largely canceling in the circumpolar zonal integral. Shallow topographic form stress (dark blue) shows step-like decreases at (from west): Kerguelen Plateau; the Macquarie Ridge region; the East Pacific Rise; South America and the Drake Passage; and the Mid-Atlantic Ridge.

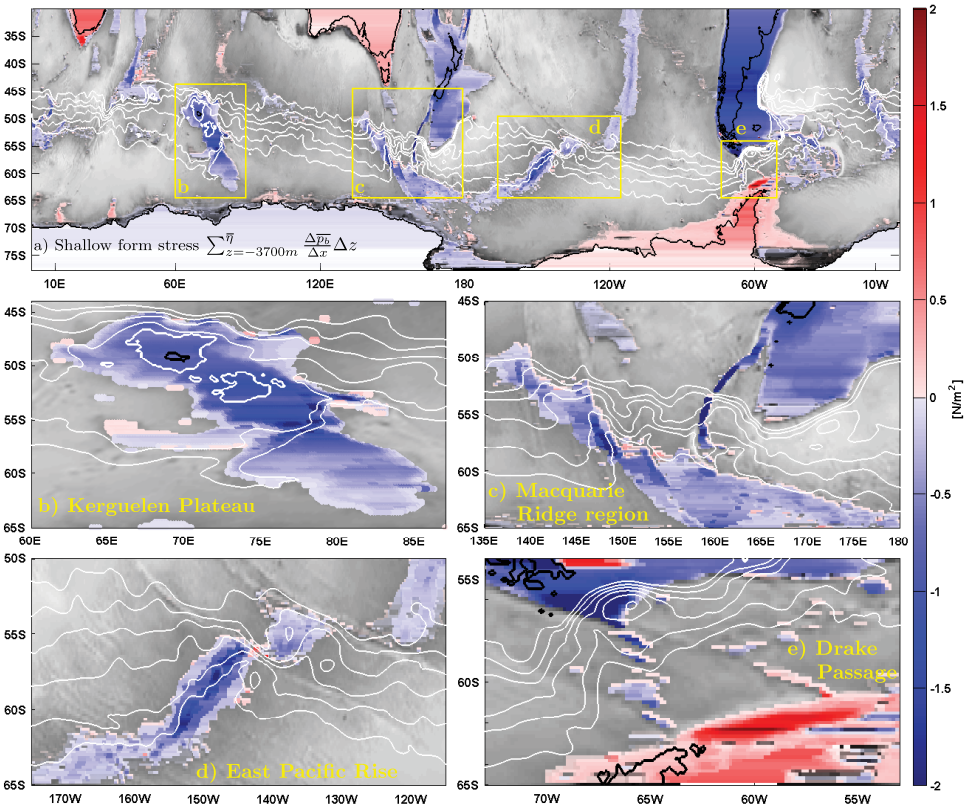

Figure 2.7: (a) Shallow topographic form stress. Close-up views of: (b) Kerguelen Plateau; (c) Southeast Indian Ridge/Macquarie Ridge/Campbell Plateau region; (d) East Pacific Rise region; and (e) Drake Passage. Solid white lines show SOSE ACC streamlines. Solid black lines show land boundaries.

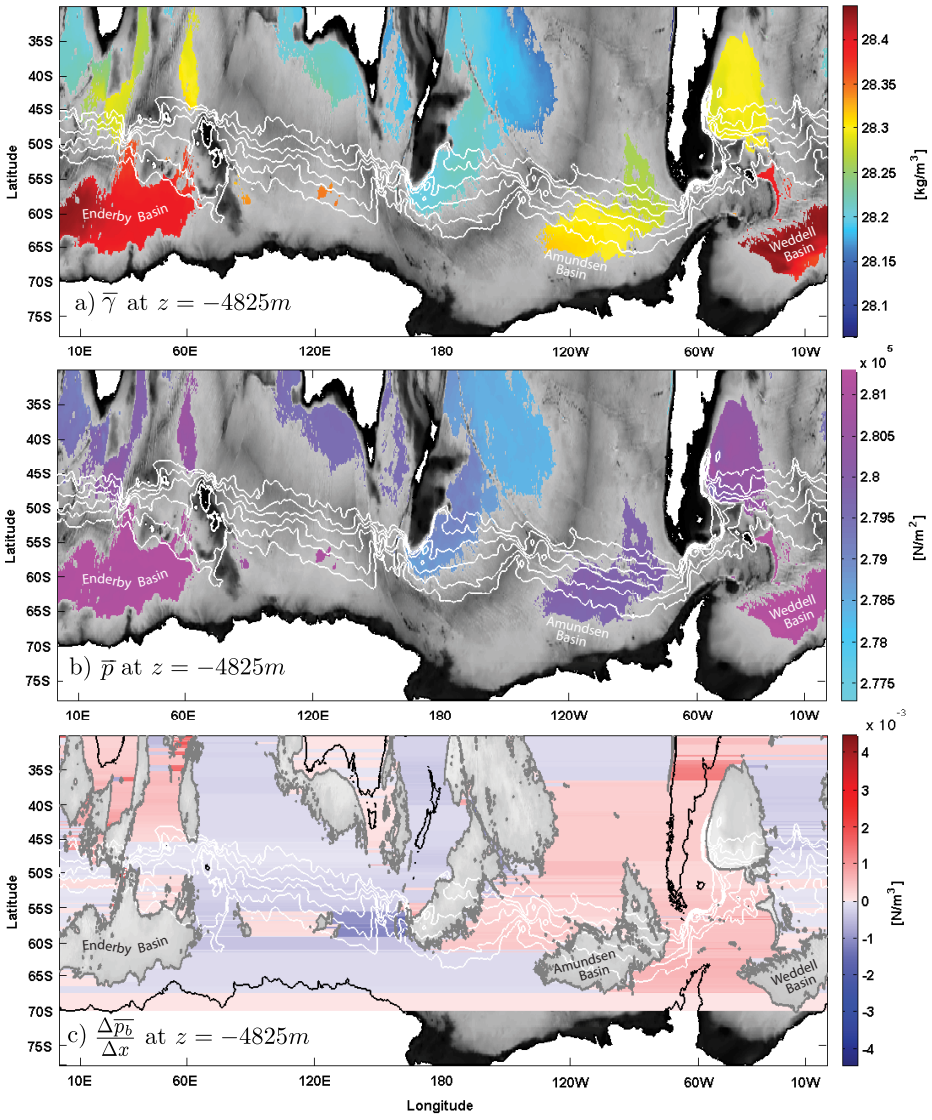

Figure 2.8: Time-mean map of (a) neutral density, (b) total pressure, and (c) topographic form stress at $z = -4825$ m. Denser water in the deep Indian and Atlantic sectors results in higher deep basin pressures than in the Pacific sector; thus the deep topographic form stress signal is largely negative between the Indian and Pacific deep basins, and largely positive between the Pacific and Atlantic deep basins.

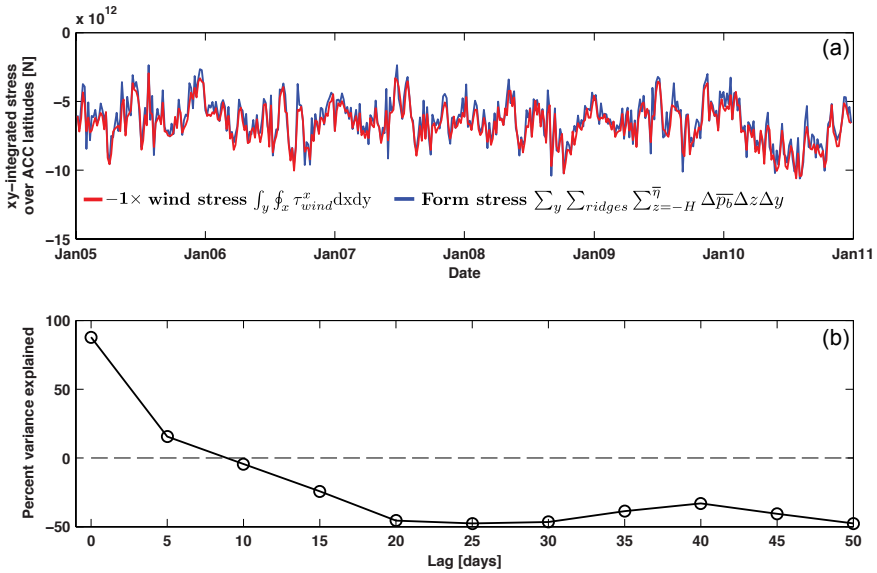

Figure 2.9: (a) Five-day averaged time series of wind stress and topographic form stress integrated over all longitudes and ACC latitudes 42°S to 65°S; wind stress signal is multiplied by -1. (b) Percent variance in the topographic form stress signal explained by the wind stress at time lags 0-50 days, over five-day increments. Maximum of 88% variance explained at 0 lag indicates a rapid topographic form stress response to changes in the wind stress signal.

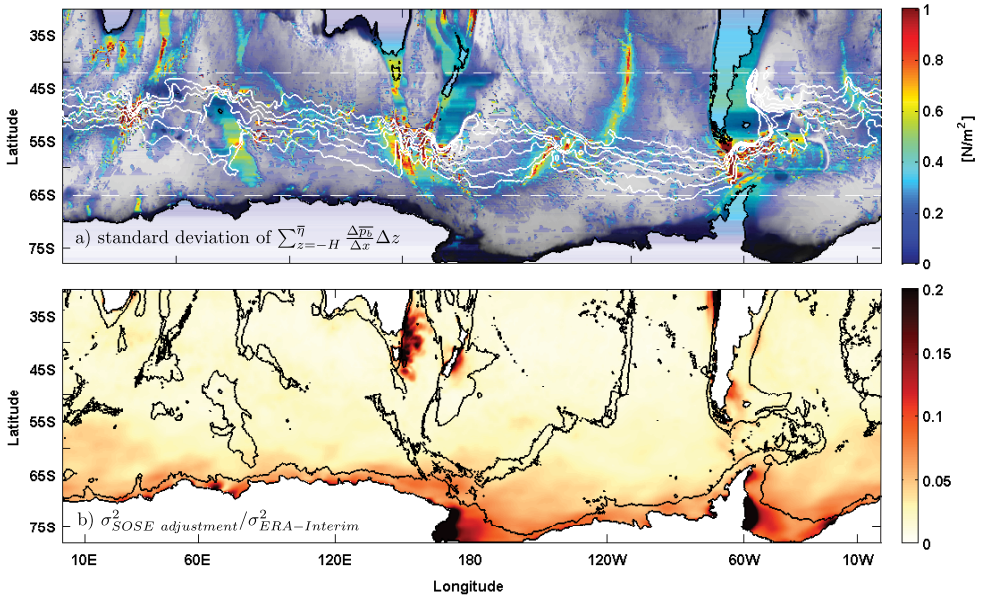

Figure 2.10: (a) Standard deviation at each point in the topographic form stress field. Higher standard deviation occurs at shallow ridges over which most of the form stress signal is concentrated, and at locations that underlie the path of the ACC jets. (b) Variance of SOSE adjustment to the ERA-Interim wind stress field normalized by the ERA-Interim wind stress variance. The 3000 m topographic contour is shown in black.

Chapter 3

Interfacial form stress in the Southern Ocean State Estimate

Key points

1. We isolate the interfacial form stress (IFS) by calculating zonal pressure gradients across isopycnal surfaces for the first time in a general circulation model.

2. IFS carries zonal momentum from wind stress source to topographic form stress sink, and reflects the signature of buoyancy forcing.

3. Transient eddy IFS dominates standing eddy IFS, but both concentrate at topographically steered currents along the ACC.

Abstract

The wind stress that drives the Antarctic Circumpolar Current (ACC) exits the fluid via topographic form stress (TFS) at the sea floor; interfacial form stress (IFS) carries much of this momentum from source to sink. These zonal momentum fluxes combine to set the strength and structure of the Southern Ocean meridional overturning

circulation (MOC), a key nexus of heat and gas exchange between the deep ocean and the atmosphere. We calculate IFS directly from the zonal pressure gradients across vertical perturbations in isopycnal surfaces, a method that includes both the mean and eddy component of the total IFS field. We confirm prevailing theory by showing that IFS compensates wind stress at the surface and carries this momentum through the ocean interior to the seafloor, where the momentum exits the fluid via topographic form stress. IFS plays a key role in balancing both wind stress and buoyancy forcing by significantly compensating wind stress in the thermocline and intermediate waters, and by driving deep water south and bottom water north across the Drake Passage latitudes.

Prior studies that have identified the dominance of the standing eddy component of the meridional overturning circulation (MOC) have not isolated interfacial form stress from the topographic form stress field. Both standing and transient eddy IFS concentrate over large topographically-steered currents along the ACC, and transient eddy IFS, rather than standing eddy IFS, comprises most of the total IFS field, suggesting that much of the standing eddy component of the MOC comes from topographic form stress rather than interfacial form stress.

3.1 Introduction

Strong, persistent eastward winds drive the Antarctic Circumpolar Current (ACC), the Southern Ocean's dominant current, on an unbroken path around Antarctica. The eastward momentum input by these winds must exit the fluid, lest the current accelerate indefinitely (Gill, 1968). The mechanisms that transmit this eastward momentum from source to sink directly control the Southern Ocean branch of the meridional overturning circulation (MOC), a key nexus of heat and carbon exchange between the deep ocean and the atmosphere (Marshall and Speer, 2012).

In a zonally-bounded ocean like the North Atlantic, momentum input by the wind exits the fluid and enters the solid earth where the ocean 'leans' against the land that forms the ocean's zonal boundaries. In the Southern Ocean, where much of the ocean lacks zonal boundaries, the fluid leans not only against available land boundaries such as South America, but also against the submerged ridges that underlie the current. Munk and Palmén (1951) first addressed the potential role of these submerged ridges in the ACC momentum balance, identifying the mechanism of fluid leaning against land as topographic form stress (TFS).

Theoretical and numerical studies of the ACC identify interfacial form stress (IFS) as the mechanism that carries zonal momentum downwards from the wind stress source at the surface to topographic sink at the seafloor (e.g. Johnson and Bryden, 1989; Olbers et al., 2004). Interfacial form stress works in much the same way as topographic form stress. In the case of topographic form stress, the fluid leans against a land ridge by exerting more pressure on one side of the ridge than the other, resulting in a transfer of zonal momentum from the fluid to the solid earth. In the case of interfacial form stress, lighter-density fluid leans against a 'ridge' of denser seawater by exerting more pressure on one side of the water 'ridge' than the other; this pressure forcing across the dense 'ridge' results in a transfer of momentum from the lighter layer to the denser layer.

Both IFS and TFS exert a pressure forcing on the layer. We have so far described TFS as a pressure forcing exerted on the land by the fluid, but we could equally describe it as an equal-but-opposite pressure forcing on the fluid by the land. Thus where the layer is bound by fluid, IFS balances a geostrophic transport in the layer, and where the layer is bound by land, TFS balances a geostrophic transport in the layer. Neglecting small atmospheric pressure forcing at the fluid surface, the combination of pressure forcing from IFS and TFS on a given fluid layer provides a full accounting of the drivers of the net geostrophic transport within the layer.

The MOC in the Southern Ocean can be modeled as the residual between a wind-driven Eulerian-mean circulation that tends to steepen the slope of Southern Ocean isopycnals, and an eddy-induced circulation that tends to relax these isopycnal slopes. In this view, the wind-driven Eulerian-mean circulation comprises wind-driven Ekman flow at the surface and a geostrophic return flow that is supported by topographic form stress at depth. Interfacial form stress appears in the eddy-induced circulation; to account for buoyancy exchange due to eddies flowing along sloped isopycnals, this eddy circulation can be expressed in terms of a meridional eddy buoyancy flux (Andrews and McIntyre, 1976; Marshall and Radko, 2003; Olbers et al., 2004).

A number of idealized channel model studies (McWilliams et al., 1978; Treguier and McWilliams, 1990; Wolff et al., 1991; Marshall et al., 1993) and general circulation model studies (Stevens and Ivchenko, 1997; Olbers and Ivchenko, 2001; Lee and Coward, 2003; Dufour et al., 2012; Mazloff et al., 2013, and others) have employed this decomposition of the MOC into Eulerian-mean and eddy-driven components to analyze the Southern Ocean zonal momentum balance. Of particular interest is a decomposition of the eddy-driven circulation term into a time-mean 'standing' component, representing zonal perturbations from the time-mean path of the ACC, and a time-varying 'transient' component. While some studies eliminate the standing component by averaging along ACC streamlines (Ivchenko et al., 1996; Best et al., 1999; Tansley and Marshall, 2001; Hallberg and Gnanadesikan, 2006), others have found that standing eddies play a dominant role in balancing the wind-driven Eulerian-mean circulation in the zonal-mean view. Stevens and Ivchenko (1997) found that standing eddies played a more important role than transient eddies in the fine-resolution Antarctic model (FRAM), but that transient eddies could balance as much as 1/3 of the Eulerian-mean circulation at some latitudes. Olbers and Ivchenko (2001) found in the 1/3-degree Parallel Ocean Program model (POP) that while transient eddies dominate in the deep ocean, standing eddies

dominate the upper ocean. In the eddy-permitting global ocean model (OCCAM), Lee and Coward (2003) showed that both transient eddies and standing eddies play important roles, and Dufour et al. (2012) showed that standing eddies play a more important role in the ACC response to transient changes in wind forcing. In the Southern Ocean State Estimate, the model used for this analysis, Mazloff et al. (2013) found that standing eddies play a larger role than transient eddies in balancing the wind-driven circulation. Thompson and Naveira Garabato (2014) used the Ocean General Circulation Model For the Earth Simulator (OFES) to refine the relationship between standing and eddy IFS, finding that IFS tends to concentrate at locations of standing eddies in the lee of topography, where the flexing of these meanders encourages the baroclinic instabilities that form mesoscale eddies where transient IFS can occur.

Still other studies have focused on the relative roles of wind stress and thermodynamic forcing in setting the strength and structure of the MOC. Surface heat loss near the Antarctic coast draws warm thermocline and intermediate waters south, while brine rejection and heat loss at low latitudes produces Antarctic Bottom Water that sinks and drives bottom water north (Mazloff et al., 2010). Marshall (1997), Shakespeare and Hogg (2012), Munday et al. (2013), and Howard et al. (2015) showed via idealized models that surface buoyancy forcing thus plays a key role in setting the MOC, and in driving the ACC itself.

In most of these studies, the role of topographic form stress is limited to the wind-driven Eulerian-mean component of the overturning, while the role of interfacial form stress is limited to the eddy overturning. In their most basic form, though, both topographic and interfacial form stresses are simply zonal pressure gradients acting on an isopycnal layer, and the geostrophic transport that is balanced by either interfacial or topographic form stress can take the form of a time- and zonal-mean, or a standing or transient eddy.

A few studies have investigated the structure of the MOC from this layer force balance perspective. In FRAM, Killworth and Nanneh (1994) showed that interfacial and topographic form stresses combined to compensate wind stress at the surface, drive deep water southwards in the interior, and drive strong northward and southward transports in the bottom water layer. Ward and Hogg (2011) and Howard et al. (2015) separated the force balance into topographic and interfacial form stresses for layers in an idealized reentrant channel model with simple topography. Ward and Hogg (2011) found that transient changes in wind stress are rapidly balanced by changes in topographic form stress, but that interfacial form stress serves to equilibrate the current via transient eddies resulting from baroclinic instabilities. Howard et al. (2015) used a similar idealized set-up, adding buoyancy forcing to the wind stress forcing. These authors found, as did Ward and Hogg (2011), that topographic form stress provides an immediate sink for wind stress momentum, but that interfacial form stress balances both the wind stress and buoyancy forcing after this initial spin-up period. Buoyancy forcing in this model tended to balance a meridional circulation that is northward in the bottom-most layers, where AABW production drives bottom water north, and southward in the layers above, where surface heat loss draws shallower water southwards.

In SOSE, too, transient changes in wind stress are largely balanced by topographic form stress on very short (< 5 day) timescales (Masich et al., 2015). The distribution of interfacial form stress and topographic form stress sets the structure of the MOC, though, and this distribution can change over longer timescales. Topographic form stress shows where momentum enters or exits the fluid system, while interfacial form stress shows where momentum is redistributed among ocean isopycnals. This paper explores the role of interfacial form stress in the MOC by conducting a layer force balance as in the studies above, and explicitly separating the interfacial form stress term from the topographic form stress term. For 30 layers covering the full SOSE domain,

we partition each isopycnal layer into segments whose geostrophic transport is balanced by topographic form stress, and segments whose geostrophic transport is balanced by interfacial form stress. Combined with the largely wind-driven ageostrophic transport in each layer, these segments sum to give a full accounting of the meridional overturning circulation in the Southern Ocean. The transport balanced by IFS alone isolates the transfer of momentum from layer to layer in the ocean interior, and mapping the mean, standing eddy, and transient eddy components of the resulting three-dimensional IFS field helps to elucidate the mechanisms that control this momentum transfer.

3.2 Methods

3.2.1 Southern Ocean State Estimate

SOSE is a 1/6-degree, eddy-permitting state estimate of the Southern Ocean south of 24.7°S. The model has 42 depth levels ranging from 10 m near the surface to 250 m at depth. Based on the MITgcm, SOSE constrains the model ocean to observations from the Southern Ocean, including satellite altimetry, sea surface temperature, and bottom pressure data, along with in-situ hydrographic data from Argo floats and a variety of regional observational programs (Mazloff et al., 2010).

SOSE bathymetry comes from Smith and Sandwell and the Earth Topography Five-Minute Grid, binned to a $1/4$-degree resolution and interpolated to the $1/6$-degree SOSE grid. This bathymetry is represented via partial cells, in which a fraction of the model cell contains fluid and a fraction contains land. In the previous topographic form stress analysis (Masich et al., 2015), we simplified the bathymetry to eliminate partial cells; here we make no such simplification.

For this analysis, we divide the model into 30 isopycnal layers of equal volume in the time-mean SOSE domain. Because conversion from a z-space model into isopycnal

space complicates the preservation of momentum and volume balances in the model, we calculate all layer terms in z-space, and then bin them into isopycnal space, as described below. We deal with outcropping layers at the surface and at topography by setting the layer to zero where it vanishes in the SOSE domain, as in Mazloff et al. (2013). We calculate all layer terms in 1-day averaged data from SOSE's 100th iteration, which spans the six years between 1 January 2005 and 31 December 2010.

3.2.2 Meridional transport in an isopycnal layer

The zonal momentum equation can be written:

$$\rho_0 \frac{\partial u}{\partial t} + \rho_0 \frac{\partial}{\partial x}(uu) + \rho_0 \frac{\partial}{\partial y}(uv) + \rho_0 \frac{\partial}{\partial z}(uw) - \rho_0 f v = -\frac{\partial p}{\partial x} + \frac{\partial \tau^x}{\partial z} + \rho_0 \nu \nabla^2 u, \quad (3.1)$$

where t is time, (u, v, w) are velocities in the (x, y, z) directions, ρ_0 is background seawater density, f is the Coriolis parameter, p is pressure, τ^x is zonal stress, and ν is kinematic viscosity.

Taking the time-mean vertical and circumpolar integral over an isopycnal layer bound above by $z = z(\gamma_n)$ and below by $z = z(\gamma_{n+1})$, where γ_n represents some neutral density surface, yields:

$$-\rho_0 f \overline{\oint_x \int_{z=z(\gamma_{n+1})}^{z=z(\gamma_n)} v \mathrm{dzdx}} = -\overline{\oint_x \int_{z=z(\gamma_{n+1})}^{z=z(\gamma_n)} \frac{\partial p}{\partial x} \mathrm{dzdx}} + \overline{\oint_x \int_{z=z(\gamma_{n+1})}^{z=z(\gamma_n)} \frac{\partial \tau^x}{\partial z} \mathrm{dzdx}}, \quad (3.2)$$

where the overbars indicate the time average, and we have neglected the small integrated Reynolds stress and interior viscosity terms. Locally, Reynolds stress divergence terms will be large in many regions, but they integrate to higher order in the time-mean circumpolar integral (Masich et al., 2015). The remaining terms describe the primary momentum balance that determines the meridional overturning circulation in the South-

ern Ocean: the Coriolis term on the left-hand side describes the meridional transport in the layer, and the two terms on the right-hand side describe the forcing that balances this transport.

To examine the role of each term in balancing the MOC, we convert the two forcing terms into the transports that they balance. The pressure gradient term balances the geostrophic component of the total meridional transport, and the stress term largely balances the ageostrophic component of the total transport:

$$V_{total} = V_{geostrophic} + V_{ageostrophic}, \tag{3.3}$$

where

$$V_{total} = \int_x \int_z v \mathrm{dzdx} = \sum_x \sum_z v \Delta z \Delta x \tag{3.4}$$

is the total meridional transport integrated over some continuous area of model grid cells that comprise the fluid layer of interest;

$$V_{geostrophic} = \frac{1}{\rho_0 f} \int_x \int_z \frac{\partial p}{\partial x} \mathrm{dzdx} = \frac{1}{\rho_0 f} \sum_x \sum_z \frac{\Delta p}{\Delta x} \Delta z \Delta x \tag{3.5}$$

is the corresponding geostrophic component of the total transport; and

$$V_{ageostrophic} = V_{total} - V_{geostrophic} \cong - \int_x \int_z \frac{1}{\rho_0 f} \frac{\partial \tau^x}{\partial z} \mathrm{dzdx} \tag{3.6}$$

is the corresponding ageostrophic component of the total transport. We will further decompose the geostrophic transport in the sections below.

3.2.3 Calculating transport balanced by TFS and IFS

We decompose the geostrophic transport into three components: transport balanced by topographic form stress, V_{TFS}, transport balanced by 'boundary' form stress, V_{BFS}, and transport balanced by interfacial form stress, V_{IFS}. Transport balanced by IFS occurs wherever water forms the zonal boundaries of the layer (green, Figures 3.1 and 3.2a), and transport balanced by TFS occurs wherever land forms the zonal boundaries of the layer (purple, Figures 3.1 and 3.2c). Transport in regions of the layer that are bound by land to the east and water to the west, or vice versa, can be classified as transport balanced by 'boundary' form stress, (orange, Figure 3.1 and 3.2b).

The combination of V_{IFS}, V_{BFS}, and V_{TFS} gives a full accounting of the geostrophic transport in the layer (Figure 3.2d). We find that 'western boundary' form stress – where land lies to the west and fluid lies to the east of the layer – tends to balance 'eastern boundary' form stress in the zonal integral (Figures 3.7b and 3.7c). For simplicity, we include the residual of these two boundary terms with the topographic term in the results below, since inclusion of these terms with the topographic term (Figure 3.7a) appears to smooth the zonally integrated topographic form stress transport field (Figure 3.6c).

We calculate form stress as the pressure difference across a zonally bound section of the layer along some fixed y and fixed z, and scaled by the height of the layer over which the gradient occurs (Figure 3.3):

$$\Big[\mathit{Form\ stress}\Big]_{x_W}^{x_E} = \frac{p(x_E) - p(x_W)}{x_E - x_W}\Delta z, \tag{3.7}$$

where x_W denotes the western zonal boundary of the layer and x_E denotes the eastern boundary of the layer. At land boundaries, we use the pressure given in the two fluid cells adjacent to land to extrapolate the pressure at the land-water interface.

3.2.4 Mean, standing eddy, and transient eddy IFS

We find the time- and zonal-mean component of the total IFS by calculating separately the six-year time-and zonal-mean pressure gradient and six-year time- and zonal-mean height of the section of the layer balanced by IFS:

$$IFS_{mean} = \left\langle \overline{\left(\frac{\sum_{z=z(\gamma_{n+1})}^{z(\gamma_n)} \frac{\Delta p_{IFS}}{\Delta x_{IFS}} \Delta z_{IFS}}{\sum_{z=z(\gamma_{n+1})}^{z(\gamma_n)} \Delta z_{IFS}} \right)} \right\rangle \left\langle \overline{\sum_{z=z(\gamma_{n+1})}^{z(\gamma_n)} \Delta z_{IFS}} \right\rangle, \tag{3.8}$$

where the brackets indicate the zonal mean, the overlines indicate the time mean, and the subscript $(\,)_{IFS}$ indicates the subset of the layer that is balanced by interfacial form stress. Scaling this term by $1/(\rho_0 f)$ yields the transport balanced by time- and zonal-mean IFS:

$$V_{mean\ IFS} = \frac{1}{\rho_0 f} IFS_{mean}. \tag{3.9}$$

We calculate the standing eddy component by subtracting this time- and zonal-mean term from the time-mean of the total V_{IFS}:

$$V_{stand\ IFS} = \overline{V_{IFS}} - V_{mean\ IFS}, \tag{3.10}$$

where the overline indicates the time-mean. We calculate the transient eddy component by subtracting the time- and zonal-mean component $V_{mean\ IFS}$ and the standing eddy component $V_{stand\ IFS}$ from the total transport balanced by IFS, V_{IFS}:

$$V_{trans\ IFS} = V_{IFS} - V_{mean\ IFS} - V_{stand\ IFS}. \tag{3.11}$$

Thus the total meridional transport can be broken down into five separate components:

$$V_{total} = V_{ageostrophic} + V_{TFS+BFS} + V_{mean\ IFS} + V_{stand\ IFS} + V_{trans\ IFS}. \tag{3.12}$$

This decomposition of the total transport allows us to attribute the meridional overturning transport into the momentum terms that balance it: transport balanced by wind stress momentum source, by topographic momentum sink, and by the mean and eddy components of interfacial form stress that carry this momentum from source to sink. We note here that both $V_{ageostrophic}$ and $V_{TFS+BFS}$ could be decomposed similarly into mean and eddy components, but these decompositions are beyond the scope of this paper.

3.3 Results

3.3.1 Meridional overturning circulation

Figure 3.4a shows the six-year time-mean meridional transport streamfunction. The filled black arrows shown in Figure 3.4a give the sense of circulation for the two main cells of the meridional overturning circulation as they appear in the Southern Ocean: a clockwise upper cell at densities lighter than approximately $\gamma = 28$ kg m^{-3}, and a counter-clockwise lower cell at densities heavier than approximately $\gamma = 28$ kg m^{-3}.

This transport streamfunction is the cumulative integral of the meridional layer transport (Figure 3.4b). Red and blue colors here indicate transport north (red) or south (blue), rather than the sense of circulation indicated by the colors in the streamfunction plot. We show the streamfunction (Figure 3.4a) only to orient the reader; from here forward, all plots will be shown in terms of the meridional layer transport (Figure 3.4b).

3.3.2 Partitioning the total transport

The full-depth transport balanced by TFS+BFS matches the wind stress-driven full-depth ageostrophic transport at every latitude (Figure 3.5a). Full-depth mean and

transient eddy IFS transports are significant; transient eddy IFS balances as much as 5 Sv northward, while mean and standing eddy IFS balances as much as 5 Sv southward. These terms balance each other, though, such that the full-depth transport balanced by total IFS is zero in the circumpolar integral. Thus the sum of all five terms – $V_{TFS+BFS}$, V_{ageos}, $V_{trans\ IFS}$, $V_{stand\ IFS}$, and $V_{mean\ IFS}$ – results in zero total meridional transport at every latitude.

We partition this vertically-integrated transport into the three separate layers of the MOC: northward intermediate and thermocline transport between the surface and $z = z(\gamma = 27.6\ \text{kg/m}^3)$ (Figure 3.5b), southward deep transport between $z = z(\gamma = 27.6\ \text{kg/m}^3)$ and $z = z(\gamma = 28.1\ \text{kg/m}^3)$ (Figure 3.5c), and northward bottom water transport between $z = z(\gamma = 28.1\ \text{kg/m}^3)$ and the seafloor (Figure 3.5d). Total transport (black line) in the intermediate and thermocline layers is northward (Figure 3.5b). In the Drake Passage latitudes, northward total transport is the sum of a strong northward wind-driven ageostrophic transport (+12.5 Sv at 60°S) and a smaller compensating southward transient eddy IFS transport (-6.0 Sv at 60°S). South of 56°S, TFS+BFS plays a very small role (-0.9 Sv at 60°S), but balances more transport to the north where South America blocks the zonal flow of the ACC at every layer.

In the deep layers between $z = z(\gamma = 27.6\ \text{kg/m}^3)$ and $z = z(\gamma = 28.1\ \text{kg/m}^3)$ (Figure 3.5c), total transport is southward (-15.0 Sv at 60°S), consisting almost entirely of southward TFS+BFS transport (-13.1 Sv at 60°S). Transient eddy IFS transport and ageostrophic transport contribute small northward components, and mean and standing eddy IFS contributes a small southward component. In the bottom water layers deeper than $z = z(\gamma = 28.1\ \text{kg/m}^3)$ (Figure 3.5d), total transport is northward (+5.7 Sv at 60°S), consisting largely of northward transient eddy IFS transport (+7.9 Sv at 60°S) and southward TFS transport (-2.0 Sv at 60°S) in the Drake Passage latitudes.

3.3.3 Wind stress, IFS, and TFS in the Drake Passage latitudes

Topographic form stress exerts forcing on the fluid wherever landmasses block the zonal path of the Southern Ocean, and wind stress directly forces most Southern Ocean layers where they outcrop at the surface at some point during the year (Mazloff et al., 2013). Thus at most latitudes, all three momentum terms – wind stress, IFS and TFS+BFS – combine to balance the transport in each layer. We focus, then, on the region where we can separate the transport balanced by each momentum term into combinations of two terms at a time: the Drake Passage latitudinal band, where no land blocks the upper ocean between 62°S and 56°S. For lighter densities in this latitude band, TFS+BFS plays no role, and the MOC is balanced by wind stress and IFS alone. At heavier densities blocked by topography, wind stress plays no role, and the MOC transport is largely balanced by IFS and TFS+BFS alone.

We highlight the Drake Passage latitude band by outlining the zonally unblocked regions in black in Figure 3.6. In thermocline and intermediate waters lighter than $\gamma = 27.6$ kg, strong northward Ekman transport is balanced by wind stress (Figure 3.6a); southward IFS transport partially compensates this northward flow (Figure 3.6b), moderating the northward upper branch of the upper cell of the MOC. In deep waters between $\gamma = 27.6$ kg m^{-3} and $\gamma = 28.1$ kg m^{-3}, the MOC largely comprises southward IFS and TFS+BFS transports (Figures 3.6b and 3.6c). In the bottom waters denser than $\gamma = 28.1$ kg m^{-3}, the northward bottom branch of the MOC consists of southward TFS+BFS transport that is outweighed by a larger northward IFS transport (Figures 3.6b and 3.6c).

Outside of the Drake Passage, all three momentum terms play a role in forcing the total layer transport, and TFS+BFS and wind stress forcing may balance each other directly in the layer at some latitudes. In the Drake Passage latitude band, where TFS+BFS and wind stress cannot balance directly, IFS carries momentum between wind

stress source and topographic sink. In this process, IFS tempers the northward flow of the upper branch of the MOC by compensating wind stress, and drives southward deep waters and northward bottom waters across the Drake Passage latitudes.

3.3.4 Distribution of mean, standing eddy, and transient eddy IFS

Nearly all of the transport balanced by IFS comes from transient eddy IFS (Figure 3.8). Time- and zonal-mean IFS plays almost no role in the overturning (Figure 3.8a), while standing eddy IFS balances a small amount of southward transport in the deep waters in the Drake Passage latitudes (Figure 3.8b). Figure 3.9 shows the three-dimensional structure of this transient IFS field.

In the intermediate and thermocline waters between the sea surface and $\gamma = 27.6$ kg m^{-3}, $V_{trans\ IFS}$ is largely southward (Figure 3.9a). Most of this southward transport concentrates in the lee of topography and in regions of high EKE (Figure 3.10c). In the deep waters between $\gamma = 27.6$ kg m^{-3} and $\gamma = 28.1$ kg m^{-3}, $V_{trans\ IFS}$ flows both northward and southward, concentrating along topographic boundaries as well (Figure 3.9b). The zonally integrated V_{IFS} (Figure 3.6b) makes clear that the northward flow in this layer occurs mostly in the denser waters between $\gamma = 28.05$ kg m^{-3} and $\gamma = 28.2$ kg m^{-3}, while the southward flow occurs in the lighter waters between $\gamma = 27.6$ kg m^{-3} and $\gamma = 28.1$ kg m^{-3}; this structure is somewhat visible in the transient eddy transport field averaged over the Drake Passage latitudes (Figure 3.9d). The combination of these northward and southward transports with southward $V_{TFS+BFS}$ still results in a net southward MOC in this layer (Figure 3.5c).

Deeper than $\gamma = 28.1$ kg m^{-3}, strongly northward $V_{trans\ IFS}$ (Figure 3.9c) outweighs southward $V_{TFS+BFS}$ such that the MOC flows northward in this layer. This northward $V_{trans\ IFS}$ lies in regions of high EKE and in the lee of large-scale topography, except in the Weddell Sea where eddy IFS drives a large-scale northward flow of bottom

water out of the Weddell basin.

Northward deep and bottom water IFS transport lies precisely beneath shallower southward IFS transport, since IFS transport must integrate to zero at every point in the horizontal plane. Locations of strong transient eddy IFS transport correspond somewhat with locations of high EKE (Figure 3.10c), indicating that some IFS transport occurs across mesoscale eddies. A few locations of very strong IFS transport lie outside of regions of high EKE, though.

In fact, regions of the very strongest transient eddy IFS transport hardly correspond with EKE at all. Mapping the absolute value of transient eddy IFS transport from surface to seafloor highlights where transient eddy IFS transport is large, in either direction (Figure 3.10a). Nearly 75% of the transient eddy IFS stronger than 0.2 Sv overlaps with regions of strong ($>$ .01 Sv) standing eddy IFS, while only 31% of transient eddy IFS stronger than 0.2 Sv overlaps with regions of high ($>$ .01 m^2s^{-2}) EKE. Regions of strongest IFS concentration are not quite colocated with the mesoscale eddies indicated by high EKE (Figure 3.10c and magenta contour, Figure 3.11a), but rather lie just upstream of these regions, corresponding instead with regions of strongest standing eddy IFS transport (Figure 3.10b and orange contour, Figure 3.11a), which is an order of magnitude smaller than the transient eddy IFS transport.

In particular, locations of transient eddy IFS transport correspond with locations of strong standing eddy IFS transport at the largest topographically steered currents along the ACC: along the eastern boundaries of Kerguelen Plateau (Figure 3.11b), MacQuarie Ridge (Figure 3.11c), Campbell Plateau, the Udintzev Fracture Zone in the East Pacific Rise, along the continental shelf in Drake Passage, and at the Malvinas Current (Figure 3.11d), the ACC's largest topographically steered current. Strong standing eddy IFS transport concentrates exclusively at these regions (Figure 3.10b), while regions of high EKE tend to lie just downstream (Figure 3.11c). The strongest transient eddy

IFS transport signals lie where strong standing IFS and high EKE overlap – where the presence of mesoscale eddies enhances the transport variability of the largest standing currents along the ACC. At Kerguelen Plateau, the Southeast Indian Ridge, the Malvinas current, and other larger-scale currents, the strongest transient eddy IFS transport occurs at the large-scale standing currents that hug topography (Figure 3.11, bottom row). Regions of strong EKE (black contours, Figure 3.11, bottom row) lie just downstream both of topography and of the standing currents themselves, enhancing their transport variability.

These topographically steered currents flow southward in the thermocline and intermediate waters; underlying deep countercurrents flow northward. Thus wind-driven Ekman flow, relatively widely distributed over the Southern Ocean, is largely compensated along these six topographically-steered currents, rather than across mesoscale eddies. Southward topographic form stress transport, which is distributed across the many zonal basins that comprise the Southern Ocean, is similarly compensated – outweighed, in fact – by northward bottom water IFS transport in these six currents as well.

The concentration of transient eddy IFS along these topographically steered currents indicates that changes in wind stress must be translated into changes in IFS largely at these standing ACC features, rather than across mesoscale eddies. The concentration of this transient eddy term in regions of standing eddy IFS suggests that changes in wind stress are translated into the ocean interior via transient adjustments to these large-scale standing eddies along the ACC, rather than across mesoscale transient eddies. This finding supports Thompson and Naveira Garabato (2014)'s point of view that the ACC equilibrates to changes in wind stress forcing via adjustments to standing meanders along the ACC. They too find that transient eddy IFS tends to concentrate at large standing meanders, fluxing momentum downwards in the lee of topography.

3.4 Summary and discussion

Mapping the total IFS field over the Southern Ocean has allowed us to address the question of where and how zonal momentum travels from wind stress source to topographic sink. We find that the structure of the SOSE total IFS field indeed largely counters the wind-driven Eulerian-mean circulation, compensating wind stress in the outcropping thermocline and intermediate waters, and countering the southward return flow, supported by TFS+BFS, in the bottom-most layers. In the deep waters between these two layers, though, IFS combines with TFS+BFS to drive this deep water southward, rather than countering the topographically-balanced flow. This southward deep water IFS transport reflects the penetration of wind stress momentum into the ocean interior, where eastward form stress in the Ekman layer is transferred downwards from layer to layer.

The combination of IFS and TFS+BFS closely resembles the form stress budget diagnosed by Killworth and Nanneh (1994) in FRAM, where the two form stresses combined to counter the surface Ekman flow in the lightest outcropping layers, to drive deep water southward, and to drive bottom water largely northward, though the direction of flow balanced by these two stresses varied with latitude. For the first time in a general circulation model, we have isolated the structure of interfacial form stress alone. We have been able to map IFS that not only balances wind stress and topographic form stress, but that transfers wind stress momentum from source to sink in the unblocked Drake Passage latitudes.

In most regions of the Southern Ocean, topographic form stress balances southward flow, rather than northward (Masich et al., 2015), and zonally integrated ageostrophic transport is very small at these depths (Figure 3.6a). This leaves interfacial form stress alone to balance the northward flow of these densest bottom waters. It is perhaps mis-

leading to say that IFS 'drives' this northward bottom flow, though. Instead, the IFS signal at these depths largely reflects the buoyancy circulation diagnosed by Howard et al. (2015), wherein southward deep water layers empty and the bottom water layers fill and flow northward. Similarly, southward IFS transport in the shallower layers not only balances wind stress and topographic form stress, but also reflects the drawing of warm waters southward due to surface heat loss in the subpolar gyres. Thus isolating the IFS signal from the wind stress and topographic form stress signals highlights the influence of buoyancy forcing in setting the strength and structure of the MOC.

Killworth and Nanneh (1994) identify this emptying and filling of layers as an 'erroneous' dynamical balance resulting from a centuries-long time dependence in FRAM's thermodynamic budget, but changes in Southern Ocean buoyancy forcing may be changing on much shorter timescales (Böning et al., 2008). At the same time, wind stress forcing is increasing over the ACC (Swart and Fyfe, 2012). These maps of IFS transport illustrate a dynamical link between mechanical and thermodynamic forcing. Stronger wind forcing over the ACC would result in a matching intensification of topographic form stress (Masich et al., 2015). To maintain the structure and strength of the MOC, the IFS field would have to exhibit a similarly matching intensification: stronger southward forcing in the lighter layers to balance wind stress, and stronger northward forcing in the denser layers to balance TFS. Similarly, a shift in buoyancy forcing would adjust IFS transport, and require a resultant change in how IFS balances wind and topographic form stresses.

Maps of the IFS field show that transient IFS dominates standing eddy and mean IFS, and that both standing and transient eddy IFS largely concentrates at six topographically steered currents along the ACC, and secondarily across mesoscale eddies. This finding is perhaps surprising given the many previous analyses that have shown the dominance of standing eddies, especially that of Mazloff et al. (2013), who found that

standing eddies dominate the zonal mean momentum balance in the Southern Ocean State Estimate itself. This difference may be due in part to the time period over which the eddy terms are calculated; we calculate the temporal anomaly with respect to the full six-year span of the model, while Mazloff et al. (2013) calculates the temporal anomaly with respect to three-month averages, and a longer time-mean tends to shift any signal from mean to transient. The six-year time average used in this analysis is longer than the two-year period used for the Mazloff et al. (2013) analysis, so interannual variability between the two analyses may play a role as well.

The chief difference between this analysis and previous analyses, though, is the explicit separation between topographic and interfacial form stress terms in this work. Both the TFS and IFS segments of each isopycnal layer may have mean, standing eddy, and transient eddy components. This analysis finds that transient eddies dominate the IFS component; thus Mazloff et al. (2013)'s and others' finding that standing eddies dominate in the overall balance suggests that these dominant standing eddies must come from the TFS partition of the overall transport, rather than the IFS partition. Indeed, Chapter Two's analysis demonstrates that the mean TFS signal is at least twice as large as the standard deviation of the TFS signal, implying the strong dominance of standing eddy TFS over transient.

Finally, though the magnitude of transient eddy IFS transport outweighs that of standing eddy IFS transport, the correspondence between topographically-steered currents and regions of strongest transient eddy IFS implies that most IFS variability occurs at these standing eddy locations, rather than at the mesoscale eddies that lie further downstream of topography. Thompson and Naveira Garabato (2014) determined that the 'flexing' of standing meanders is the mechanism that equilibrates the ACC in response to changes in wind stress. The concentration of transient eddy IFS in these standing meander regions suggests this meander flexing as well, since changes in meander structure

would appear as a transient signal with respect to the six-year time and zonal mean.

3.5 Acknowledgments

SOSE data is available at sose.ucsd.edu. This work was supported by National Science Foundation grants PLR-1141922 and PLR-1341431, and National Aeronautics and Space Administration grant NNX13AE446. J. Masich was also supported by the Department of Defense through the National Defense Science & Engineering Graduate Fellowship Program. We are grateful for fruitful comments and discussion with David Marshall and one anonymous reviewer.

Chapter Three, in part, has been submitted to the Journal of Geophysical Research: Oceans. Masich, J., M. R. Mazloff, and T. K. Chereskin. The dissertation/thesis author was the primary investigator and author of this paper.

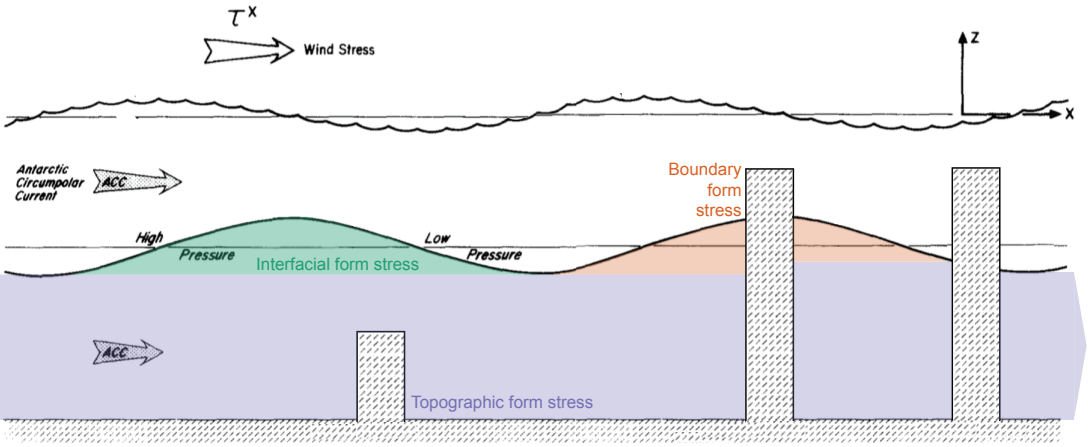

Figure 3.1: Schematic ocean layer adapted from Johnson and Bryden (1989). Green section indicates where interfacial form stress balances the geostrophic transport within the layer; orange section indicates where 'boundary' form stress balances the geostrophic transport in the layer; and purple section indicates where topographic form stress balances the geostrophic transport in the layer. Arrows at the edges of the topographic form stress section indicate zonally reentrant domain.

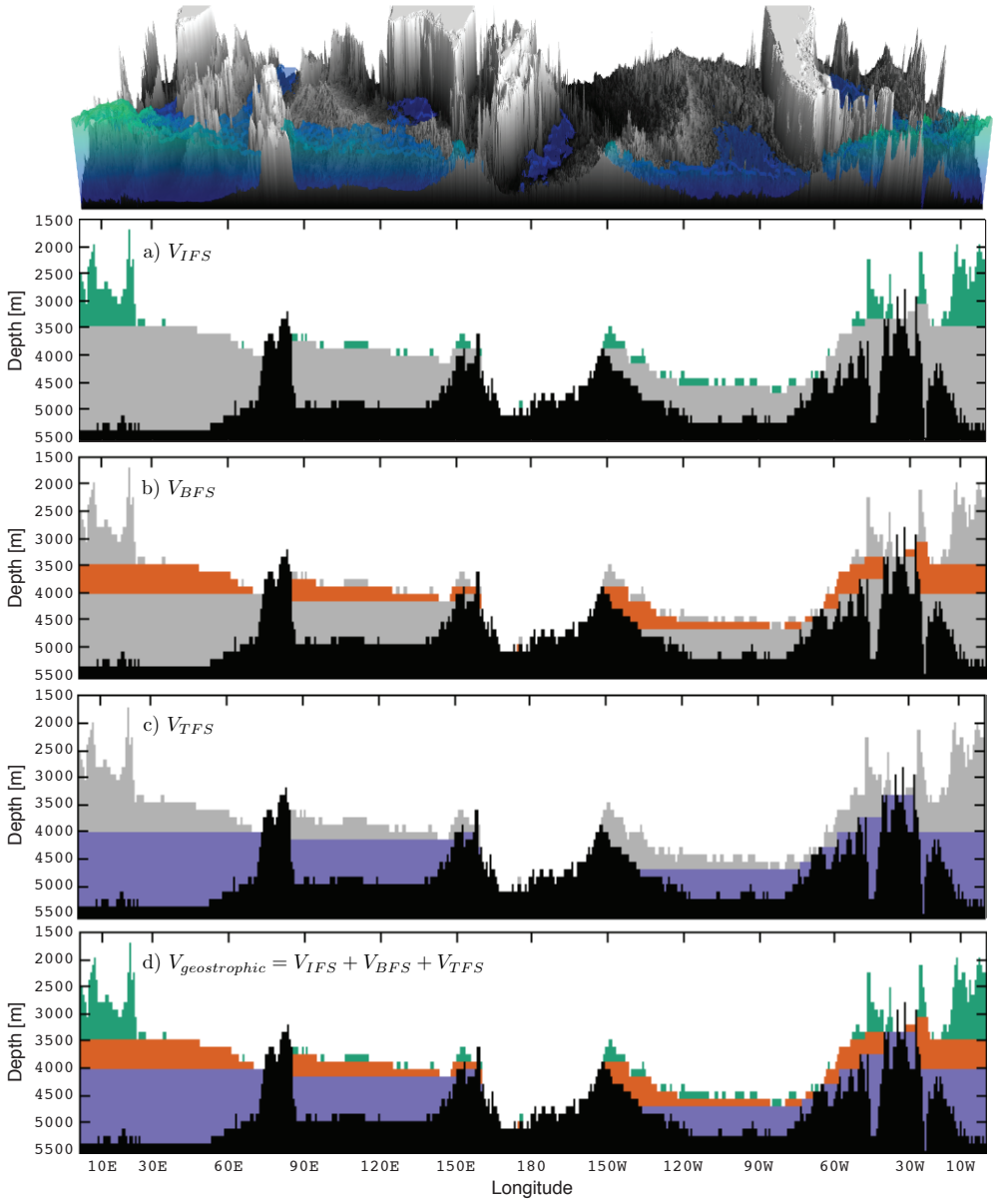

Figure 3.2: Example layer spanning $z = [-H, \gamma = 28.2\ \text{kg/m}^3]$ on 11 April 2005, with a vertical cut at 60°S. Partitions of transport in the layer at this 60°S latitude circle that are balanced by: (a) interfacial form stress; (b) boundary form stress; and (c) topographic form stress. This partitioning of the layer gives a full accounting of the geostrophic transport in the layer, (d).

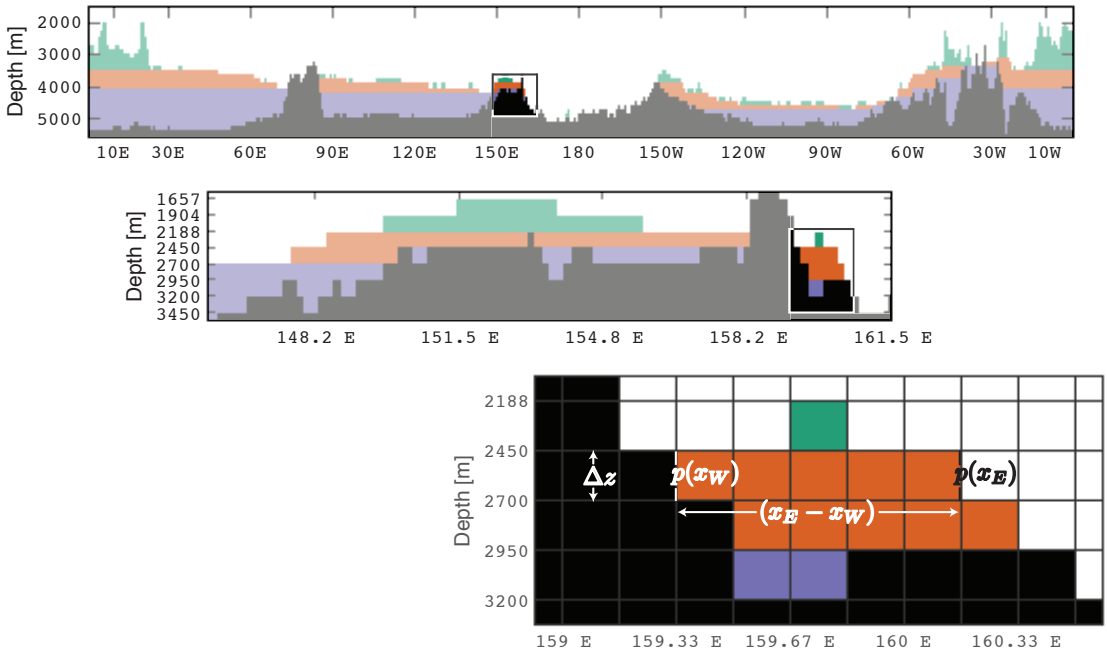

Figure 3.3: Zoom-in on the example layer shown in Figure 3.2. Green indicates transport balanced by IFS, orange indicates transport balanced by boundary form stress, and purple indicates transport balanced by TFS. The pressure gradient $(p(x_e) - p(x_w))/(x_e - x_w)$ gives the boundary form stress on the labeled layer. The sum of the pressure gradients in the cells that lie between $p(x_e)$ and $p(x_w)$ is equivalent to this boundary form stress.

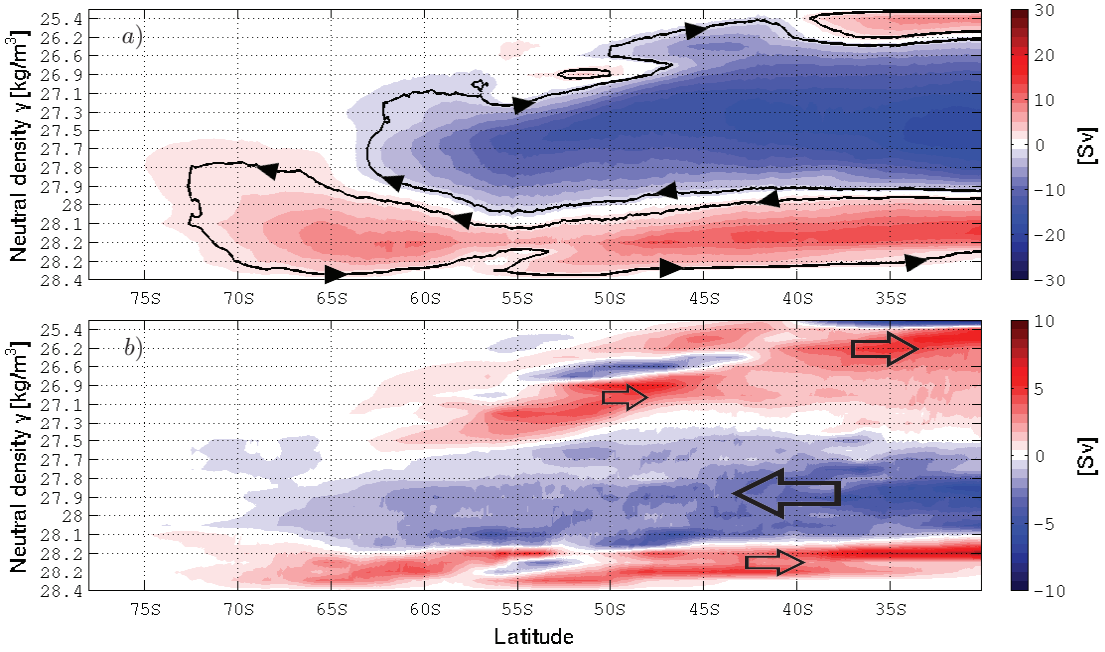

Figure 3.4: Six-year time-mean: (a) meridional streamfunction and (b) meridional transport. Small filled black arrows show the sense of streamfunction circulation; negative blue values indicate clockwise circulation, while positive red values indicate counter-clockwise circulation. Larger open arrows show the direction of flow for the meridional transport; negative blue values indicate southward flow, while positive red values indicate northward flow.

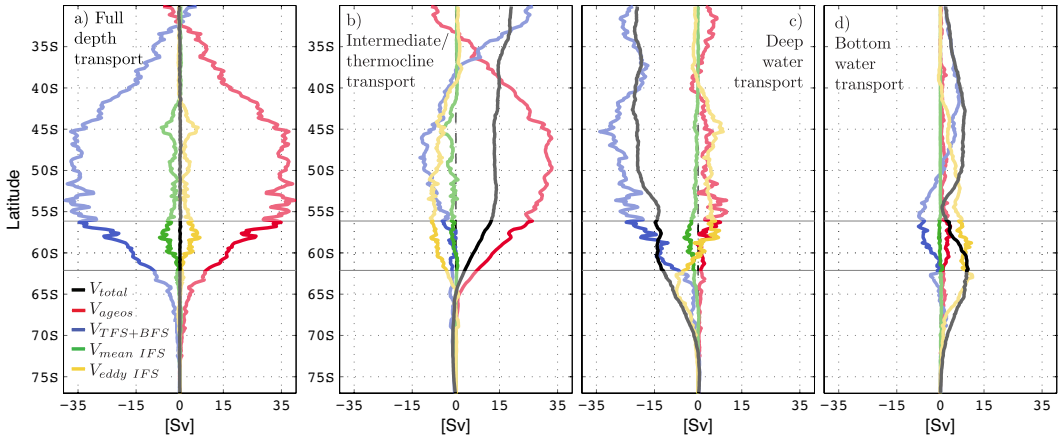

Figure 3.5: Six-year time-mean meridional total transport (black), and contributors to this total transport: ageostrophic transport balanced by wind stress (red), and geostrophic transports balanced by BFS+TFS (blue), by mean and standing eddy IFS (green), and by transient eddy IFS (yellow). Figure (a) shows the full-depth transport, while figures (b), (c), and (d) show transports for the three main layers of the MOC: (b) equatorward intermediate and thermocline water ($z = [z(\gamma = 27.6\ \text{kg/m}^3), \eta]$), where η is the height of the sea surface; (c) poleward deep water ($z = [z(\gamma = 28.1\ \text{kg/m}^3), z(\gamma = 27.6\ \text{kg/m}^3)]$); and (d) equatorward bottom water ($z = [-H, z(\gamma = 28.1\ \text{kg/m}^3)]$), where H is the depth of the seafloor. Horizontal gray lines indicate Drake Passage latitudes 62°S to 56°S.

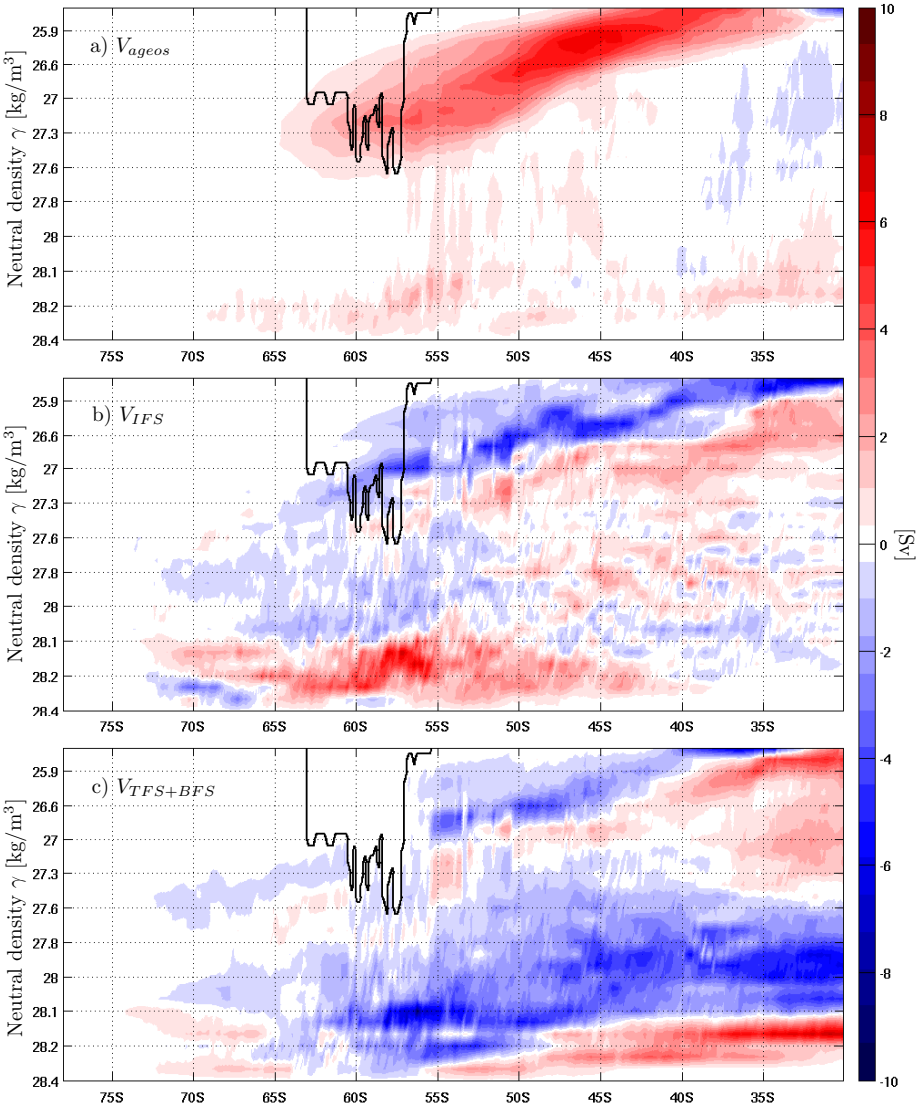

Figure 3.6: Six year time-mean and zonally integrated: (a) ageostrophic transport; (b) transport balanced by interfacial form stress; and (c) transport balanced by topographic form stress and boundary form stress. Black contour indicates Drake Passage latitudes where the Southern Ocean is not zonally blocked by topography.

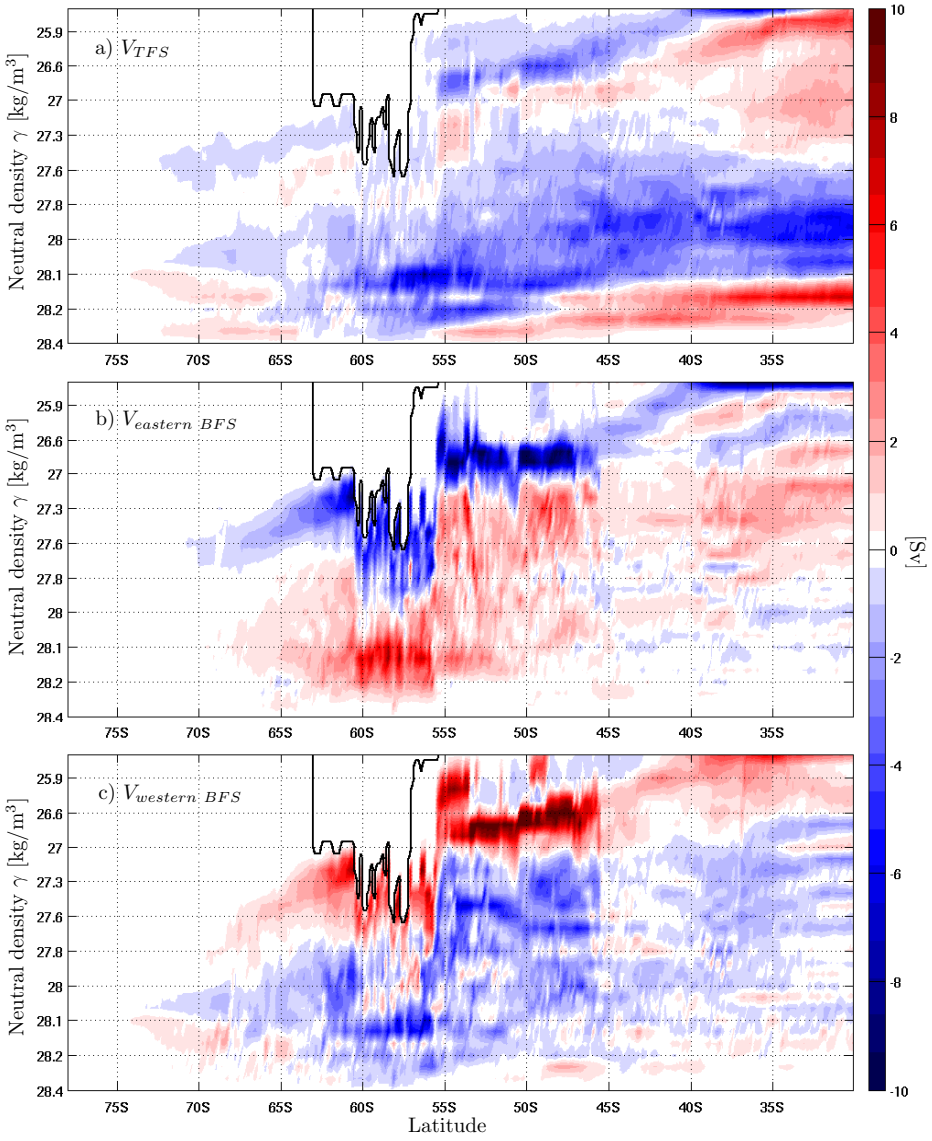

Figure 3.7: Six year time-mean and zonally integrated transport balanced by: (a) topographic form stress, where land lies to both the east and west of the layer; (b) eastern boundary form stress, where land lies to the east and water lies to the west of the layer; and (c) western boundary form stress, where land lies to the west and water lies to the east of the layer. The sum of these terms is the transport balanced by TFS+BFS, shown in Figure 3.6c. Black contour indicates Drake Passage latitudes where the Southern Ocean is not zonally blocked by topography.

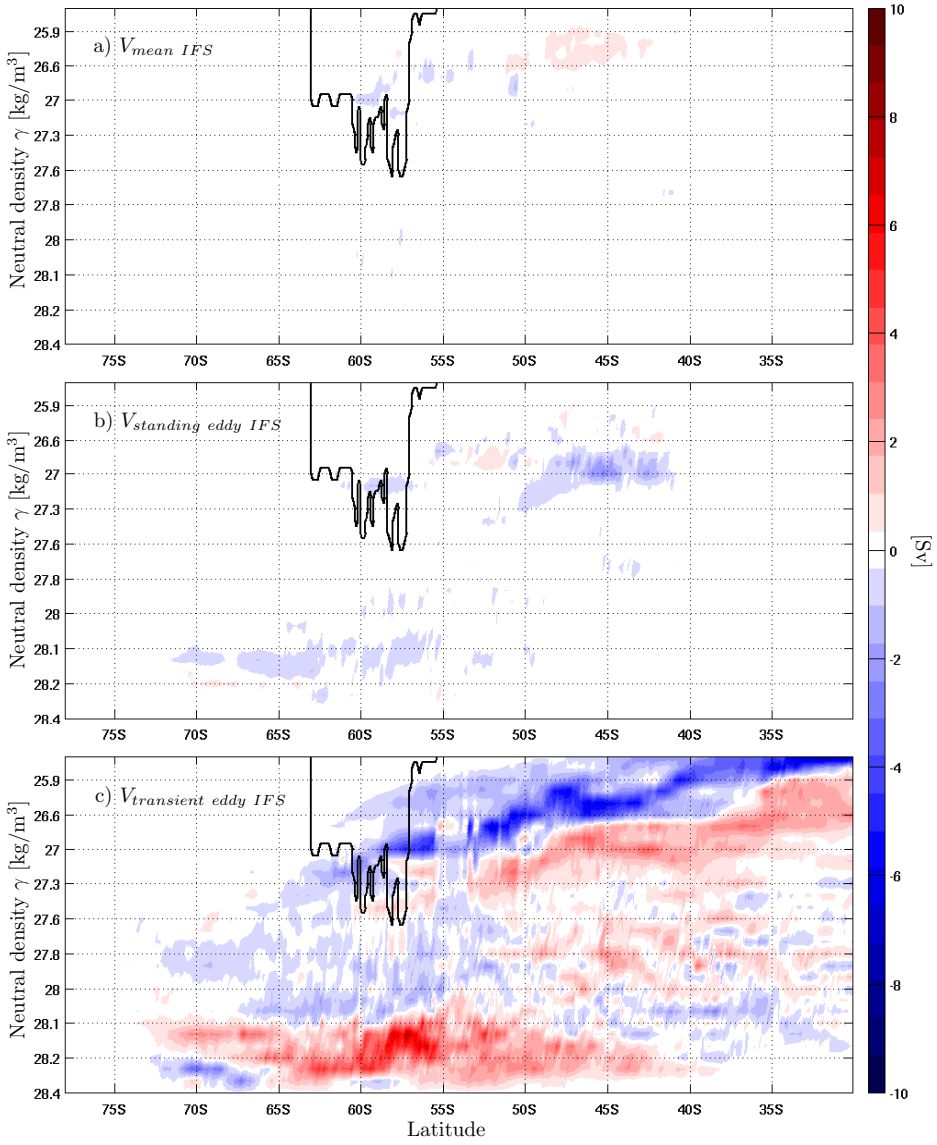

Figure 3.8: Six-year time-mean and zonally-integrated transport balanced by: (a) mean IFS; (b) standing eddy IFS; and (c) transient eddy IFS. The sum of these terms is the transport balanced by IFS, shown in Figure 3.6b. Black contour indicates Drake Passage latitudes where the Southern Ocean is not zonally blocked by topography.

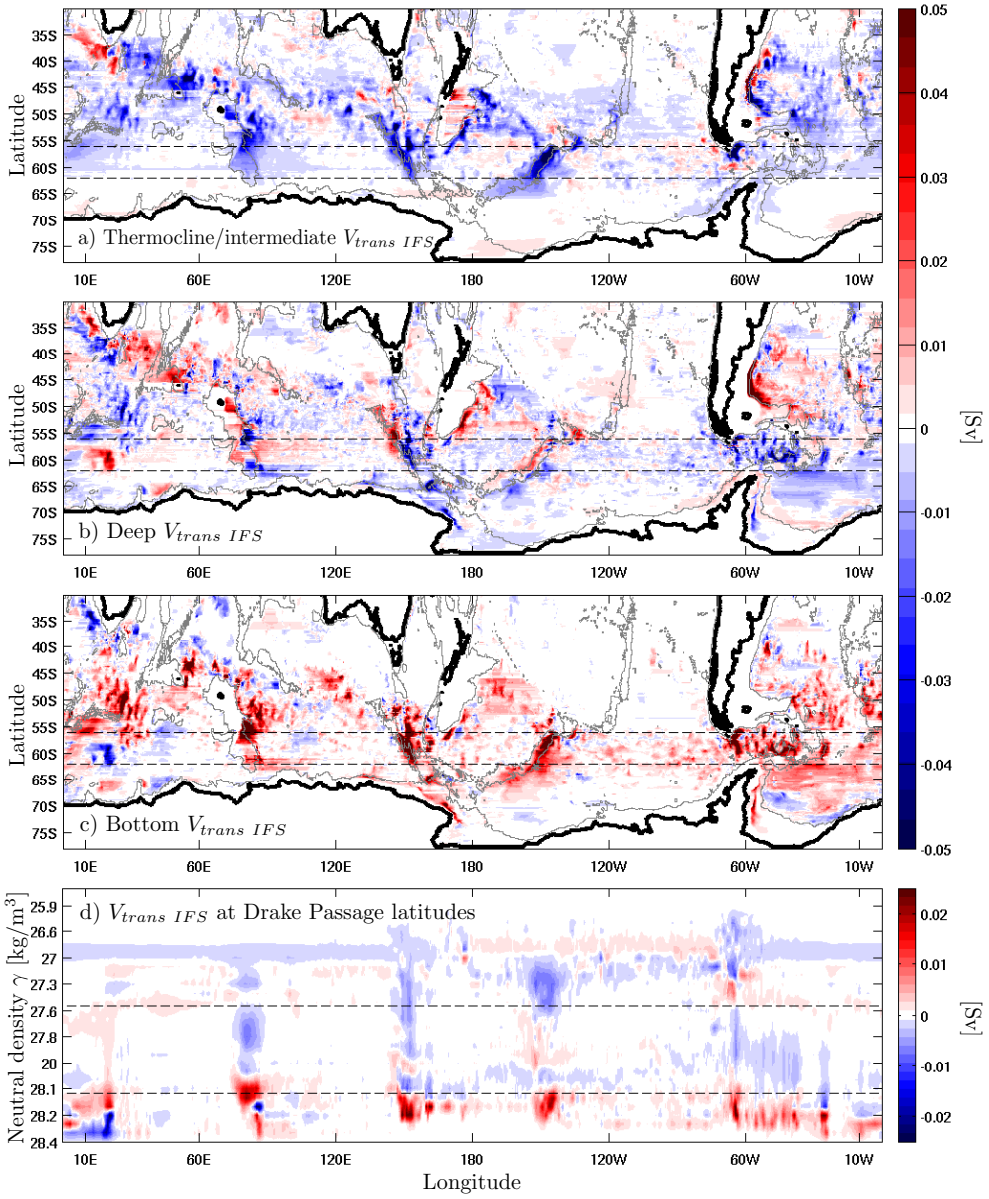

Figure 3.9: Six year time-mean transient eddy IFS transport for: (a) thermocline/intermediate water between $\gamma = 27.6$ kg/m^3 and the sea surface; (b) deep water between $\gamma = 27.6$ kg/m^3 and $\gamma = 28.1$ kg/m^3; and (c) bottom water between $\gamma = 28.1$ kg/m^3 and the sea floor. Dotted black lines show Drake Passage latitudes. Time-mean $V_{trans\ IFS}$ averaged over Drake Passage latitudes, (d); dotted black lines show divisions between Intermediate/thermocline water, deep water, and bottom water shown in (a) through (c) above.

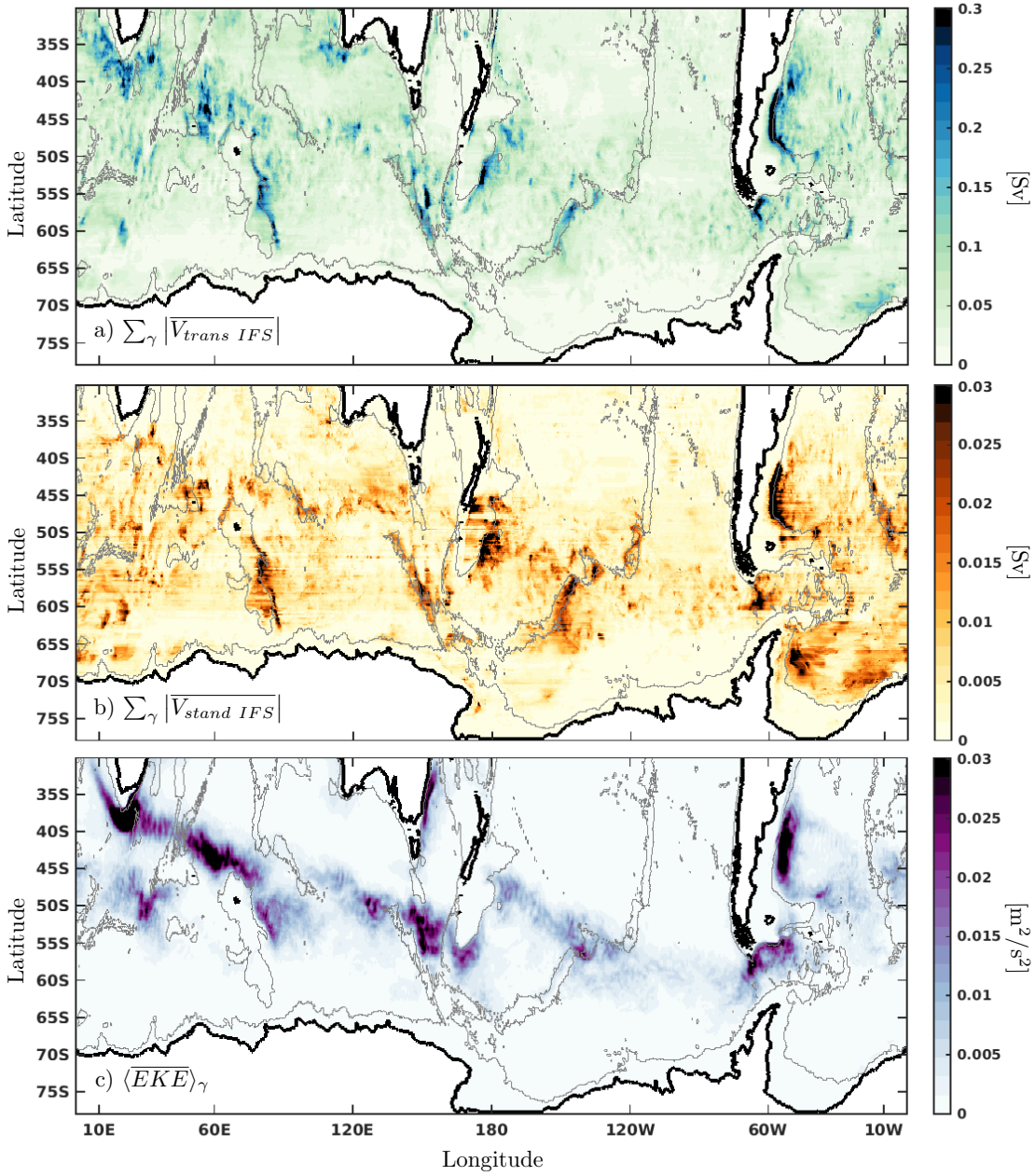

Figure 3.10: (a) Six year time-mean full-depth $\left|V_{trans\ IFS}\right|$ showing where the most transient eddy IFS transport occurs, north or south. (b) Six year time-mean full-depth $\left|V_{stand\ IFS}\right|$ showing where the most standing eddy IFS transport occurs, north or south. (c) Time- and layer-mean EKE averaged over all layers in the domain. Grey contour in all three plots shows the $z = -3000$ m contour; black lines denote land boundaries.

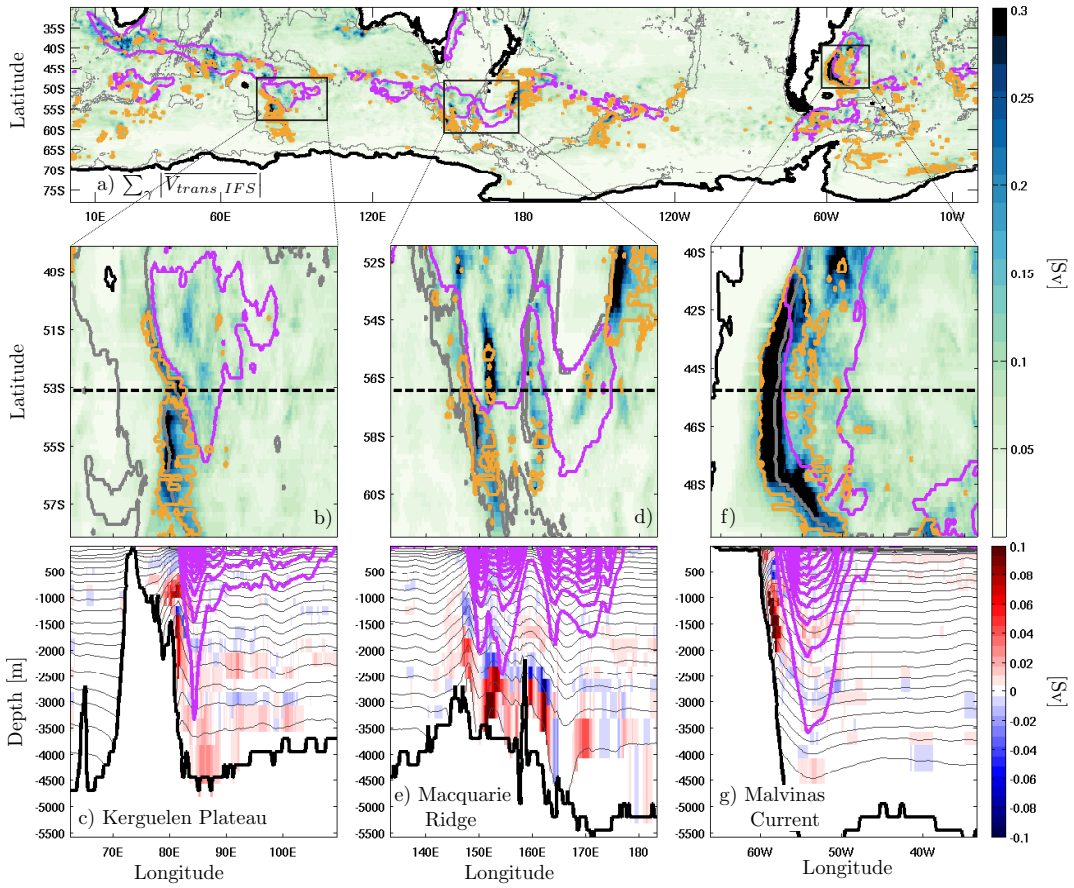

Figure 3.11: Figure 3.10, with contours of $\langle \overline{EKE} \rangle_\gamma > .01$ m^{2}s^{-2} overlaid in magenta, and contours of $\left|V_{stand\ IFS}\right| > .02$ Sv overlaid in orange, (a). Figure 3.11a zoomed in at: Kerguelen Plateau, (b); Macquarie Ridge (d); and the Malvinas current, (f). Black dotted lines show the location of the side-view shown in the bottom row of plots. Six-year time-mean transient eddy IFS transport shown at mean locations of isopycnal layers for Kerguelen Plateau, (c); Macquarie Ridge, (d); and the Malvinas Current, (g). Grey lines indicate isopycnal layer boundaries; black lines indicate land, and magenta contours indicate six-year time-mean EKE.

Chapter 4

Observational estimates of interfacial form stress in the Drake Passage

Abstract

We estimate interfacial form stress (IFS) across a standing frontal meander in the Antarctic Circumpolar Current (ACC) using observations from the cDrake experiment, a four-year deployment of Current and Pressure recording Inverted Echo Sounders (CPIES) in the Drake Passage. The unique properties of the CPIES array allow us to estimate IFS in this region using two different methods. The first method is a direct estimate of IFS in terms of the pressure exerted from one isopycnal layer to another, as in Chapter Three. The second is a parameterization of transient eddy IFS in terms of meridional buoyancy flux and the background stratification of the region, as in previous observational estimates of IFS along the ACC. We use the direct estimate of IFS to ground-truth Chapter Three's basin-scale transient eddy IFS field calculated from the Southern Ocean State Estimate (SOSE), and we use the parameterized estimate of transient eddy IFS to expand upon previous observations in the Drake Passage region. Finally, we compare the two fields to evaluate how effectively the parameterized formulation for transient

eddy IFS can capture the direct estimate.

We find that the vertical structure and magnitude of parameterized IFS corresponds with previous observational estimates in the region, but shows a degree of both horizontal and vertical structure previously unobserved in the Southern Ocean. The comparison between the observational estimates of direct and parameterized IFS show that parameterized IFS well captures the horizontal structure of the direct estimate, but the vertical structure of the two fields differ. The direct observational estimate of transient eddy IFS closely parallels the zonal mean structure of the SOSE transient eddy IFS field, driving thermocline and intermediate water lighter than approximately $\gamma = 27.6$ kg/m^3 north, bottom water denser than approximately $\gamma = 28$ kg/m^3 north, and the deep water that lies between these two isopycnals south.

4.1 Introduction

Wind stress over the Southern Ocean drives the world's largest current, the Antarctic Circumpolar Current (ACC), around the Antarctic continent. Because the ACC does not accelerate indefinitely, this eastward momentum input by wind stress must find an exit from the fluid system. Gill (1968) showed that bottom friction is an unlikely momentum sink; instead, eastward momentum exits the Southern Ocean via topographic form stress across landmasses and submerged ridges (Munk and Palmén, 1951; Olbers, 1998; Masich et al., 2015). Interfacial form stress (IFS) carries the momentum through the fluid interior, connecting source to sink (Johnson and Bryden, 1989; Olbers, 1998).

Interfacial form stress is directly analogous to topographic form stress. Eastward momentum is transferred from one fluid layer to another when the layer above 'leans' on the layer below – when the pressure on the west flank of a vertical perturbation in

the interface between the layers is greater than the pressure on the east flank. This pressure gradient transfers momentum from layer to layer, inducing a geostrophic transport in each layer. In a basin-scale numerical model, this pressure gradient across interface perturbations can yield a direct estimate of total IFS. On a regional scale, a paucity of coherent interface perturbations in the region can make this type of estimate impossible. Thus regional observational and numerical studies of IFS assume that transient eddy IFS comprises the majority of the total IFS signal, and calculate IFS in terms of a parameterization of transient eddy IFS that depends on estimates of eddy buoyancy flux, which can be estimated at a single point, and some knowledge of the background stratification in the region.

4.2 Two formulations of interfacial form stress

The upper cell of Southern Ocean meridional overturning is usually expressed as the sum of two transports: the mean overturning, flowing clockwise in the y-z plane – north at the surface, and southwards in the interior – and the eddy overturning that counters this mean term (Olbers, 1998; Marshall and Radko, 2003, and others). These mean and eddy terms can be expressed in terms of a thickness-weighted overturning (e.g. Young, 2012), or in terms of a transformed Eulerian mean (e.g. Andrews and McIntyre, 1976). Vallis (2006) succinctly expresses the approximate equivalence of these overturning formulations:

$$\overline{v_*} = \frac{\overline{vh}}{\overline{h}} + \frac{\overline{v'h'}}{\overline{h}} \approx \overline{v} - \frac{\partial}{\partial z}\frac{\overline{v'b'}}{\overline{b_z}} = \overline{v^*}, \tag{4.1}$$

where the overline indicates the time and zonal mean; v is meridional velocity; $\overline{v_*}$ on the far left represents the thickness-weighted overturning; $\overline{v^*}$ on the far right represents the transformed Eulerian mean overturning; $\overline{h}$ is the average thickness of some isopycnal

layer; $b = g(\rho - \rho_0)/\rho_0$ is buoyancy, where g is the acceleration due to gravity and $\rho_0 = 1035$ kg/m^3 is the background density; and $(\,)'$ indicates the perturbation to the time and zonal mean.

The center left-hand-side of the equation gives the mean and eddy decomposition of the thickness-weighted overturning, while the center right-hand-side gives the mean and eddy decomposition of the transformed Eulerian mean overturning. In the temporal and zonal average, the total terms $\overline{v_*}$ and $\overline{v^*}$ and the mean terms $\overline{vh}/\overline{h}$ and $\overline{v}$ should be nearly equivalent, implying that the two eddy terms, $\overline{v'h'}/\overline{h}$ and $-\left(\overline{v'b'}/\overline{b_z}\right)_z$ will be roughly equivalent as well.

These two eddy terms represent the two formulations of transient eddy IFS that we will explore in this chapter. In the case of the largely geostrophic ocean interior, the thickness-weighted formulation for transient eddy IFS overturning, $\overline{v'h'}/\overline{h}$, includes a direct estimate of the zonal pressure exerted from one isopycnal layer to another:

$$\frac{\overline{v'_{geostrophic}h'}}{\overline{h}} = \frac{g}{\rho_0}\frac{\overline{p'_x h'}}{\overline{h}}, \tag{4.2}$$

where p is pressure. In the zonally unblocked region of the Southern Ocean, the left-hand-side of this equation is the thickness-weighted velocity balanced by eddy interfacial form stress as calculated in Chapter Three; thus we refer to this formulation as 'direct' IFS and the transformed Eulerian mean formulation as 'parameterized' IFS.

The equivalence between the thickness-weighted and transformed Eulerian mean overturnings shown in equation 4.1 requires a circumpolar integration unbroken by zonal boundaries; thus we can expect direct and parameterized IFS to match strictly when zonally integrated along the Drake Passage belt or along closed ACC streamlines only. Observational efforts, though, have relied on the parameterized formulation to represent IFS locally. Mooring experiments, concentrated in a few highly energetic re-

gions of the ACC, yield remarkably consistent local IFS estimates. Johnson and Bryden (1989) calculated a parameterized IFS profile ranging from 0.76 Nm^{-2} near the surface to 0.43 Nm^{-2} at depth in the northern Drake Passage, and Phillips and Rintoul (2000) found parameterized IFS ranging between 0.2 Nm^{-2} and 0.51 Nm^{-2} south of Tasmania. Lenn et al. (2007) estimated shallow parameterized IFS profiles of approximately 0.2 Nm^{-2} as well, using synoptic shipboard acoustic Doppler current profiler and expendable bathythermograph measurements between 100 m and 250 m across the Drake Passage. All of these observations conclude that IFS transfers momentum downward only, indicating that lighter layers of water in these regions consistently exerted an eastward pressure forcing on the denser layers below.

The cDrake Local Dynamics Array (LDA) allows us to expand upon these point mooring estimates in three ways. The first is the expansion of previous one-dimensional IFS estimates into three dimensions across a standing frontal meander, giving us a sense of the spatial structure of the mean parameterized IFS field that these point estimates have sampled (Section 4.1).

Estimating both direct and parameterized IFS from the same observational dataset allows us to compare the two formulations. A strict interpretation of the parameterized IFS formulation requires a zonally unbounded circumpolar integration. Comparison of the parameterized IFS field to the concurrent direct IFS field allows us to evaluate the usage of this parameterization for local estimates (Section 4.2).

Finally, the spatial coverage and resolution of the LDA allows us to identify distinct isopycnal layers and estimate the zonal pressure exerted from one layer to another, a direct estimate of IFS. This estimate allows us to determine the meridional transport balanced by direct IFS within the LDA – indeed, from these data, we can estimate the contribution of this small region of the ACC to the transient eddy IFS component of the full meridional overturning (Section 4.3). This observational estimate of transport

balanced by eddy IFS can also be used to ground-truth the basin-scale model estimate explored in Chapter Three.

4.3 Methods

4.3.1 cDrake Experiment

As part of the cDrake experiment (Chereskin et al., 2012), 45 Current and Pressure Recording Inverted Echo Sounders (CPIES) were deployed across the Drake Passage between Tierra del Fuego and the Antarctic Peninsula (Figure 4.1). The CPIES were positioned to include the C-Line, a line of 27 CPIES spanning the Drake Passage and spaced an average of 50 km apart, and the Local Dynamics Array (LDA), a three-by-seven grid of CPIES spaced approximately 37 km apart in the northern Drake Passage. The placement of the LDA was chosen to capture eddies and interactions between the Polar Front and the Subantarctic Front, the two most energetic fronts in the region.

The CPIES instrument is uniquely suited for observations in the Drake Passage because the instrument observes from the seafloor, rather than higher in the water column where strong near-surface currents can interfere with instruments. The CPIES comprises three types of measurements: an Aanderaa current meter tethered 50 m above bottom, a pressure sensor attached 0.5 m above bottom, and an inverted echo sounder measuring the round-trip vertical acoustic travel time between the instrument and the sea surface. All instruments sampled at hourly or shorter intervals.

Tracey et al. (2013) used a second-order polynomial fit to scale the full-depth round trip acoustic travel time τ to a common pressure level of 2000 dbar, the deepest extent of many of the Argo profiles used to construct the hydrographic property look-up tables described below. Hourly time series of this scaled travel time τ_{2000}, of bottom pressure, and of bottom current were three-day lowpass filtered and subsampled

to twice daily (Tracey et al., 2013). Firing et al. (2014) objectively mapped this twice-daily data into two-dimensional maps of τ_{2000} and geostrophic bottom velocity mapped to 4000 dbar. This study combines these travel-time and bottom velocity maps with the hydrographic look-up tables described below to estimate three-dimensional maps of interfacial form stress.

4.3.2 Estimating hydrographic properties in the array

Because the speed of sound changes with water density, vertical acoustic travel time is modulated largely by temperature and more weakly by salinity in the water column above the echo sounder. Though the travel time observation corresponds to a specific mean water column density profile, more than one possible vertical density structure can correspond to the same travel time observation. The gravest empirical mode (GEM) technique uses local historical hydrographic data to empirically determine the density structure most likely to correspond to a given vertical acoustic travel time observation (Meinen and Watts, 2000; Donohue et al., 2010).

Almost 600 hydrographic profiles are used to construct the GEM, spanning the years 1975-2011 and concentrated in the Drake Passage between 54.5°S and 64.5°S, and 57°W and 80°W. All casts used in this analysis extended to at least 2000 dbar; about half of these, largely collected between 2007 and 2011 during the cDrake experiments, extended to 3800 dbar, limiting the vertical scope of cDrake array objective maps of these properties to 3500 dbar. Since most of the casts were collected during the austral summer, Cutting (2010) estimated and removed a seasonal cycle in the upper 150 meters of both the historical CTD casts and the travel time data via a supplementary dataset of Drake Passage XCTDs collected year-round (Sprintall et al., 2012).

The CTDs are used to calculate multiple GEMs: temperature, salinity, specific volume anomaly (computed via the MATLAB Seawater toolbox (Morgan, 1994)), and

geopotential height, calculated by integrating specific volume anomaly from 3800 dbar (Firing, 2012). To construct each GEM, vertical acoustic travel times are computed from the CTD data; these full-depth travel times are then converted to τ_{index}, the integrated round-trip travel time between the surface and 2000 dbar (Meinen and Watts (2000); Donohue et al. (2010)). To construct the GEM, the water property of interest – temperature, for example – is first binned over depth. Since the number of CTD observations diminishes with depth, these bins increase in size from 10 dbar near the surface to 400 dbar at depth (Firing, 2012). In each depth bin, a cubic spline is fit to the temperature data as a function of τ_{index}. These spline fits at each depth are combined into a lookup table between τ_{index} and corresponding temperature profiles, and cubic splines are used again to interpolate these vertical profiles to 10-dbar resolution (Firing, 2012). In this way, vertically integrated travel time measurements alone can be used to infer the vertical structure of the water column above the IES instrument.

Though the GEM technique produces a low-mode view of the three-dimensional density structure in the study region, Sun and Watts (2001) show that this method nonetheless succeeds in capturing 97% of the total Southern Ocean density variance. More locally, Chidichimo et al. (2014) showed that the cDrake experiment GEMs capture the dominant vertical structure in the region. Error estimates on GEM properties employed in the IFS calculation – temperature T, buoyancy b, and stratification N^2 – come from the root-mean-square difference between the property as calculated directly from the CTD casts and the profiles of each property given by the GEMs.

4.3.3 Estimating velocity in the array

Combined with bottom velocity measurements, the geopotential anomaly GEM can be used to calculate the geostrophic streamfunction in the array. We calculate merid-

ional geostrophic velocity v_g using the construction from Donohue et al. (2010):

$$v_g = v_{bcb} + v_{bottom} = \frac{1}{f}\left[\frac{\partial \tau_{2000}}{\partial x}\frac{\partial \Phi}{\partial \tau_{2000}}\right] + v_{bottom}, \tag{4.3}$$

where f is the Coriolis parameter, the derivative of geopotential anomaly Φ with respect to τ_{2000} comes from the 10 dbar resolution GEM, and τ_{2000}, $\partial\tau_{2000}/\partial x$, and v_{bottom} come from Firing et al. (2014)'s objective maps of each term. Firing et al. (2014) provide error estimates for v_g at 200 dbar intervals; because these estimates are relatively smoothly varying in z, we estimate error on v_g by interpolating these error estimates to the finer 10 dbar resolution.

4.3.4 Estimating direct and parameterized IFS in the array

We estimate parameterized IFS from the total meridional geostrophic velocity v_g given in Equation 4.3 and from buoyancy b and stratification N^2 estimates that are interpolated from their respective GEMs:

$$IFS_{param} = \rho_0 f \frac{\overline{v_g' b'}}{\left\langle \overline{N^2} \right\rangle_{array}}. \tag{4.4}$$

The temporal mean and anomaly are taken over the full timespan of the four-year experiment, except where indicated in the results section below. Angle brackets $\langle\ \rangle_{array}$ indicate the horizontal mean over the array; thus the stratification term $\left\langle \overline{N^2} \right\rangle_{array}$, represents a single time- and array-mean profile that represents the background stratification of the region.

Direct IFS relies on total meridional geostrophic velocity v_g, as above, and on a knowledge of the height h of the isopycnal layer over which it is calculated. For consistency with Chapter Three, we divide the cDrake array into the same 30 isopycnal

layers employed for the SOSE analysis. We calculate direct transient eddy IFS in terms of the thickness-weighted geostrophic velocity in the layer and the thickness of the layer itself:

$$IFS_{direct} = \rho_0 f \frac{\overline{v_g' h'}}{\bar{h}}, \tag{4.5}$$

where the layer height h is calculated as the height of the isopycnal layer interpolated from the neutral density (γ) GEM. For comparison to eddy IFS calculated from the Southern Ocean State Estimate in Chapter Three, we convert IFS_{direct} into the geostrophic transport balanced by this transient eddy IFS term, $V_{trans\ IFS}$, by zonally and vertically integrating:

$$V_{trans\ IFS} = \overline{v_g' h'} \mathrm{dx}, \tag{4.6}$$

where $\mathrm{dx} = 10^4$ m is the zonal grid spacing for the objective maps of bottom velocity and travel time constructed by Firing et al. (2014).

Because the vertical scope of the cDrake array is limited to 3500 dbar, we limit the spatial domain of the direct IFS analysis to layers that do not outcrop at this 3500 dbar bottom boundary or at the surface at any point in the four-year record; $\gamma = 28.075$ kg/m^3 thus represents the 'floor' of the vertical domain, and $\gamma = 27.13$ kg/m^3 represents the 'lid.' As a result, parameterized and direct IFS are calculated over slightly different spatial domains; Section (4.2.3) places the two estimates in the same spatial domain for direct comparison.

4.4 Results

4.4.1 Parameterized IFS

Johnson and Bryden (1989) made observational estimates of parameterized IFS from an array of moorings deployed a few hundred kilometers to the southwest of the

cDrake Local Dynamics Array (Figure 4.1, white circles). They constructed a single profile of time-averaged IFS by combining estimates of eddy heat flux $\overline{v'T'}$ and potential temperature gradient $\overline{\theta_z}$ estimated from temperature and velocity measurements at various depths among the moorings. For comparison to this parameterized IFS profile, we calculate parameterized IFS both in terms of equation 4.4 and in terms of temperature, where eddy temperature flux $\overline{v'T'}$ replaces eddy buoyancy flux, and the background potential temperature gradient $\left\langle \overline{\theta_z} \right\rangle_{array}$ replaces the background stratification:

$$IFS_{temperature\ param} = \rho_0 f \frac{\overline{v'T'}}{\left\langle \overline{\theta_z} \right\rangle_{array}}. \tag{4.7}$$

We average the buoyancy and temperature versions of parameterized IFS over the array to yield the time- and horizontal-mean profiles (Figure 4.2, blue and red), which both agree reasonably well with the Johnson and Bryden (1989) profile (Figure 4.2a, black). Below 2500 m, the profiles are nearly identical; above 2500 m, differences between the cDrake temperature IFS estimate and the Johnson and Bryden (1989) estimate are largely due to differences in the eddy heat flux estimated at each location. Johnson and Bryden (1989) estimated stronger poleward eddy heat fluxes at every depth compared to the array-mean cDrake estimate. This may be due in part to the placement of the cDrake array; because the array centers over a frontal meander, strong poleward eddy heat fluxes at the beginning of the meander are balanced by strong equatorward eddy heat fluxes further downstream (Watts et al., 2016). Differences are also due in part to greater structure in the mixed layer and thermocline sections of the background potential temperature gradient, resulting in some vertical structure in the cDrake IFS profile above 1000 m that is unresolved in the Johnson and Bryden (1989) estimate.

Finally, salinity plays an important role in the Southern Ocean, compensating temperature inversions in the Drake Passage and elsewhere that prevent temperature or

potential temperature from accurately representing the density structure of the water column (Stephenson et al., 2012). We thus compare parameterized IFS estimated from temperature (Figure 4.2, red) and from buoyancy (Figure 4.2, blue). Below 1200 m, the two profiles are nearly identical. Shallower than 1200 m, the two profiles match within error bars, except where the temperature IFS calculation exhibits structure that is not present in the buoyancy calculation, largely due to structure in the array- and time-mean $\left\langle \overline{\theta_z} \right\rangle_{array}$ profile that does not appear in the array- and time-mean $\left\langle \overline{N^2} \right\rangle_{array}$ profile.

Three-dimensional structure

Previous observational estimates of parameterized IFS are exclusively positive in sign, confirming the general theory that IFS balances wind stress. The array-mean profiles align with these previous results, but the three-dimensional structure that underlies this mean profile indicates that IFS exhibits a great deal of structure (Figure 4.3). Were Johnson and Bryden (1989) to place their moorings in a location closer to the southeast corner of the cDrake array, where IFS is strongly negative, they would have found an negative IFS profile – the opposite sign of that predicted by theory.

Positive IFS (Figure 4.3, red) dominates the western side of the array, closer to the Shackleton Fracture Zone, while a lee-wave-like pattern of negative and positive IFS dominates the eastern side of the array. Positive IFS indicates where pressure exerted by a lighter isopycnal layer on the heavier layers below is eastward; thus positive IFS implies the downward flux of eastward momentum that carries windstress into the ocean interior. Negative IFS (Figure 4.3, blue) indicates the upward flux of eastward momentum, or equivalently the downward flux of westward momentum. Vertical structure in the array is different for downward versus upward IFS; downward IFS appears to concentrate towards the ocean interior, while upward IFS concentrates near the surface.

4.4.2 Comparing parameterized and direct IFS

Thus far, we have discussed parameterized IFS in pressure terms, for comparison to previous observational estimates. To bring this term into dialogue with direct IFS, we calculate both parameterized and direct IFS in the velocity units in which they should be roughly equivalent. Following equation 4.1, we take the vertical divergence of parameterized IFS:

$$v_{param\ IFS} = -\frac{\partial}{\partial z}\frac{\overline{v'b'}}{\overline{N^2}}, \tag{4.8}$$

and divide direct IFS by the mean height of each isopycnal layer:

$$v_{direct\ IFS} = \frac{\overline{v'h'}}{\overline{h}} \tag{4.9}$$

to formulate both forms of IFS in terms of the transient eddy contribution to the residual meridional overturning velocity.

The direct IFS velocity term is calculated in density space. For comparison between the two terms, we calculate the time-mean parameterized IFS velocity term in Cartesian space, and then sort it into density space. Because the position of the isopycnal layers is time-dependent, we sort the time-mean parameterized IFS velocity term into isopycnal layers for every day of the time period in question, and then take the time-mean of the daily sorted parameterized IFS velocity. We thus have a direct and parameterized IFS velocity term, both in density space, for comparison.

The direct IFS velocity estimate is limited to the isopycnal layers that are resolved for the full time period within the cDrake array; for the full four-year span of the experiment, the 'floor' for this term is the $\gamma = 28.075$ kg/m^3 isopycnal, which appears in the time-mean around 2200 m to 2800 m depth, and the 'lid' is the $\gamma = 27.13$ kg/m^3 isopycnal, which appears in the time-mean around 100 to 200 m depth. As the lightest non-outcropping layer in the domain, this 'lid' isopycnal can be considered a reasonable

proxy for the bottom of the mixed layer; our comparison thus omits the mixed layer, where we do not expect equation 4.1 to hold true. Having placed the two terms on equal spatial footing in the ocean interior, we evaluate how closely parameterized IFS velocity and direct IFS velocity match by comparing the pattern and magnitude of the vertical-mean fields. To compare pattern, we calculate the correlation coefficient between the two fields; to compare magnitude, we compare the ratio of the root-mean-square (rms) of each field.

We compare the two vertical-mean fields over a number of different isopycnal domains. Holding the floor at $\gamma = 28.075$ kg/m^3, we allow the lid of the spatial domain to range from this floor up to the lightest density in the domain, $\gamma = 27.13$ kg/m^3 (Figure 4.4, *y*-axis). Because the density structure in the array changes seasonally, we conduct this analysis not only for the full four-year time-mean (Figure 4.4, black), but for the summer months December, January and February (Figure 4.4, magenta), and for the winter months June, July and August (Figure 4.4, cyan).

The correlation coefficient for the two fields is highest for the summer averaged fields, perhaps because the 'lid' isopycnal surface more consistently represents the bottom of the mixed layer in the less dynamically volatile summer months. Correlation coefficients increase steadily as the 'lid' moves further above the 'floor', until the 'lid' reaches $\gamma = 27.34$ kg/m^3, where we see a maximum correlation coefficient of 82% for the summer months (Figure 4.4a).

The ratio of the rms of each field approaches one around this isopycnal as well; where the isopycnal 'lid' is $\gamma = 27.34$ kg/m^3, the rms of the parameterized field is only 18% larger than the rms of the direct IFS field (Figure 4.4b). Other choices for isopycnal layer 'lids' result in an rms of the parameterized field that ranges from twice as large to nearly 6 times as large as the rms of direct IFS field.

The optimal match between the two fields thus occurs when they are averaged

over the summer months only, with isopycnal 'floor' at $\gamma = 28.075$ kg/m^3 and isopycnal 'lid' at $\gamma = 27.34$ kg/m^3. The high correlation and low rms ratio between the two vertical-mean fields implies that parameterized IFS velocity can reasonably well represent direct IFS velocity in the vertical mean (Figure 4.5a and 4.5c).

The vertical structure contributing to these vertical-mean fields does not appear to match quite as well as the zonal-mean fields. Mapping the zonal average of each isopycnal layer back into z-space gives us a rough sense of the vertical distribution of these best-matched parameterized and direct IFS velocity fields (Figure 4.5b and 4.5d). While both fields are strongly concentrated towards the surface, the parameterized field exhibits an alternation in sign with depth that is not visible in the direct field. We thus conclude that parameterized IFS can represent direct transient eddy IFS reasonably well in the regional vertical mean, but perhaps not so well in the regional zonal mean.

4.4.3 Direct IFS

Over the full circumpolar domain, transient eddy IFS transport in the Southern Ocean State Estimate thermocline/intermediate water layers is almost entirely southward in the ACC latitudes (Figure 4.6a). A small northward transport in this layer in the Drake Passage latitudes is largely due to a strong northward transport along the continental shelf in the Drake Passage. Zooming in on the contribution to this circumpolar field from the cDrake region in the model (Figure 4.6b) emphasizes this northward $V_{trans\ IFS}$, which dominates the isopycnal layers between $\gamma = 27.3$ kg/m^3 and $\gamma = 27.6$ kg/m^3 in the cDrake region of the model (Figures 4.6a, 4.6b). In both zonal integrations of the model field – circumpolar (Figure 4.6a) and cDrake region ((Figure 4.6b) – southward deep $V_{trans\ IFS}$ is bounded above by this subsurface northward flow at approximately $\gamma = 27.6$ kg/m^3, and below by northward-flowing bottom water at approximately $\gamma = 28.05$ kg/m^3.

Remarkably, the zonal sum of $V_{trans\ IFS}$ estimated from the observational array exhibits a structure quite similar to that in the model field (Figure 4.6c): northward transport of thermocline/intermediate waters lighter than $\gamma = 27.6$ kg/m^3 and bottom waters heavier than $\gamma = 28.05$ kg/m^3, and southward transport of the deep waters bordered by these two water masses. This transport is about $1/3$ as strong as the SOSE domain transport. This may be due to the fact that the model includes transport that is balanced by transient eddy IFS across not only structures that are fully resolved in the cDrake region, but also by eddy IFS that occurs across vertical perturbations in the layer whose widths exceed the scope of the domain.

This similarity in vertical structure between the model and observational estimates may reflect a similarity in IFS structure across topographically-steered currents, as in Chapter Three. The strongest northward and southward IFS transports in both the model and the cDrake array occur just downstream of topography; cDrake IFS transport concentrates along the Shackleton Fracture Zone (SFZ; Figures 4.7a, 4.7c and 4.7e), while the model IFS transport concentrates along the continental shelf (Figures 4.7b, 4.7d and 4.7f), perhaps because the SFZ is largely unresolved in the model topography (Figure 4.8). In both model and observational estimates, the north-south-north vertical structure of regional IFS transport is dominated by the presence of this structure at topographically steered currents; indeed, we see this concentration of eddy IFS at topographically-steered currents along the whole of the SOSE ACC (Figure 3.10). The cDrake estimate of transient eddy IFS transport thus proves a strong ground-truth of the SOSE eddy transient IFS field; even on scales as small as a single topographically-steered frontal meander, the north-south-north structure of the transient eddy IFS transport contribution to the meridional overturning circulation is clearly visible.

4.5 Summary and discussion

The cDrake Local Dynamics Array has afforded us a unique opportunity to explore the structure of interfacial form stress along a standing frontal meander in the ACC. The mean profile of parameterized IFS in the array closely aligns with previous estimates in the region and elsewhere along the ACC. As seen in previous estimates (Phillips and Rintoul, 2000; Lenn et al., 2007; Johnson and Bryden, 1989), the array-mean profile of parameterized IFS is positive, transferring eastward wind stress momentum downwards through the water column, with magnitude slightly larger than the 0.2 Nm^{-2} basin-mean wind stress, implying that the Drake Passage may be a hot spot of IFS momentum transfer.

The horizontal scope of the array expands this one-dimensional view of IFS, demonstrating that the array-mean profile comprises a great deal of horizontal and vertical structure; strong positive IFS dominates the upstream side of the frontal meander, but IFS varies in sign further downstream. Regions of negative IFS tend to intensify towards the sea surface, while regions of positive IFS in the array intensify towards the ocean interior.

The array also provides the unique opportunity to calculate IFS directly, in terms of the pressure exerted from one layer to another in the northern Drake Passage. The analytical equivalence between parameterized and direct IFS, given by equation 4.1, relies on a circumpolar integration; thus the rough match in the horizontal structure of the regional parameterized and direct IFS terms is perhaps surprising. Tuning of the isopycnal 'lid' that represents the top of the ocean interior allows the parameterized formulation to have a correlation coefficient as high as 82% with the horizontal structure of the direct estimate, but the vertical structure does not match as well.

Finally, a zonal integration of the direct estimate of IFS demonstrates that the

structure of the basin-scale contribution of transient eddy IFS to the residual meridional overturning circulation can be seen via observational data across a single standing meander in the Drake Passage. The observational estimate of transport balanced by transient eddy IFS flows northward in the thermocline/intermediate densities lighter than $\gamma = 27.6$ kg/m^3, southward in the deep waters between $\gamma = 27.6$ kg/m^3 and $\gamma = 28$ kg/m^3, and back northward again in the bottom waters denser than $\gamma = 28$ kg/m^3. This same north-south-north structure can be seen in the model estimate of $V_{trans\ IFS}$ in the northern Drake Passage cDrake region and in the basin-scale zonal integration.

This result implies that the structure of the transient eddy contribution to the overall residual meridional overturning circulation can be observed at a single frontal meander along the ACC. The rough parallelism between the two estimates of IFS, direct and parameterized, suggests that a parameterized estimate of IFS may be able to capture a large percentage of the horizontal distribution of this structure, especially within the summer-time ocean interior; thus local observations of buoyancy flux and background stratification can provide insight into the structure of the eddy contribution to the overall residual overturning circulation in the Southern Ocean.

4.6 Acknowledgments

The National Science Foundation Office of Polar Programs supported this work under NSF grants PLR-1141922 and PLR-1542902, and the National Aeronautics and Space Administration supported this work under grant NNX13AE44G. J. Masich was also supported by the Department of Defense through the National Defense Science and Engineering (NDSEG) program. Thanks to D.R. Watts, K. A. Donohue, K. L. Tracy, G. Chaplin, E. Sousa, and A. Foppert at the University of Rhode Island, and Y. L. Firing for their work collecting, processing and analyzing the cDrake data.

Chapter Four is currently being prepared for submission for publication of the material. Masich, J., T. K. Chereskin, and M. R. Mazloff. The dissertation author was the primary investigator and author of this material.

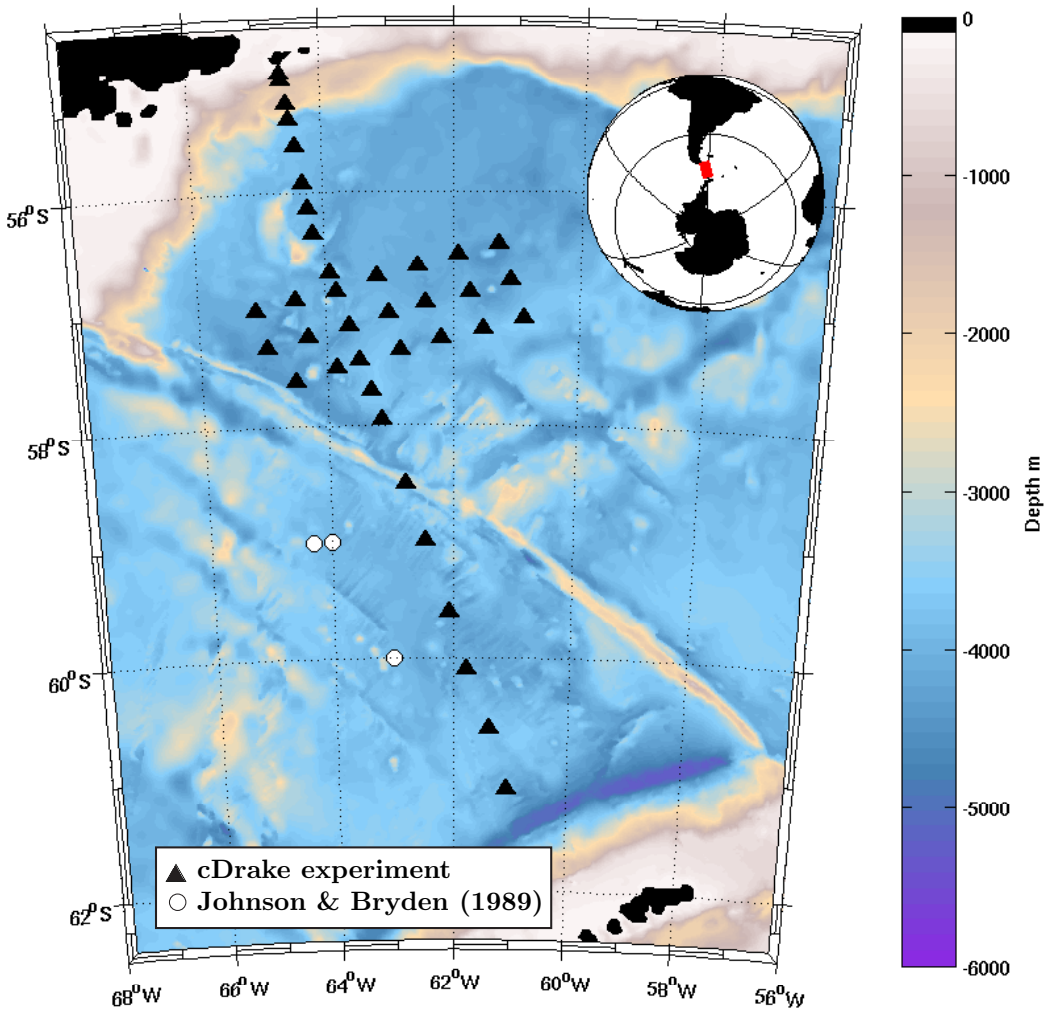

Figure 4.1: Map of the Drake Passage region. Black triangles indicate cDrake Experiment CPIES. White circles indicate current meter moorings used for Johnson and Bryden (1989) analysis. Bathymetry is combination of shipboard multibeam measurements from the R/V Nathaniel B. Palmer with the Smith and Sandwell (1997) satellite-derived bathymetry (Firing, 2012).

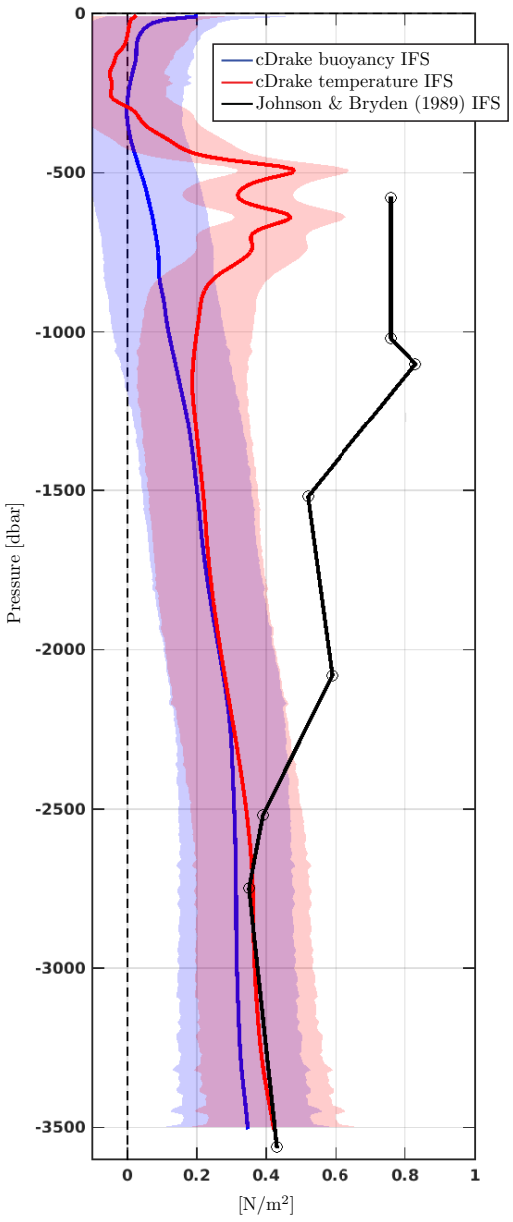

Figure 4.2: Time- and array-mean cDrake Experiment IFS profile calculated from buoyancy, blue, and from temperature, red. Johnson and Bryden (1989) IFS profile, black.

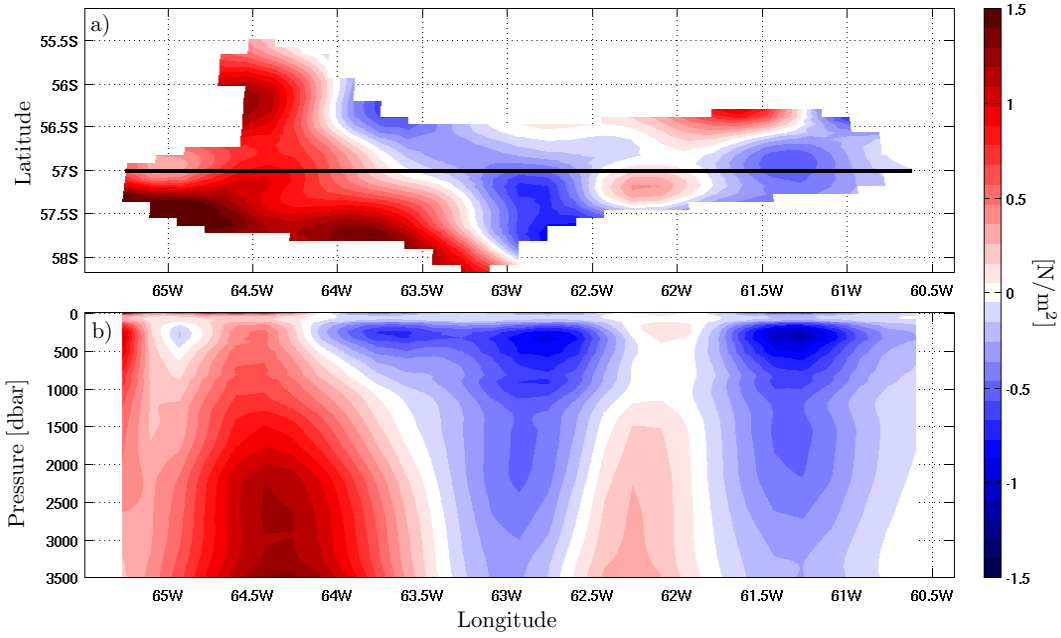

Figure 4.3: Four-year time- and depth-mean IFS, (a); black line indicates 57°S. Four-year time-mean vertical structure at 57°S, (b). Red indicates the downward flux of eastward momentum; blue indicates the upward flux of eastward momentum.

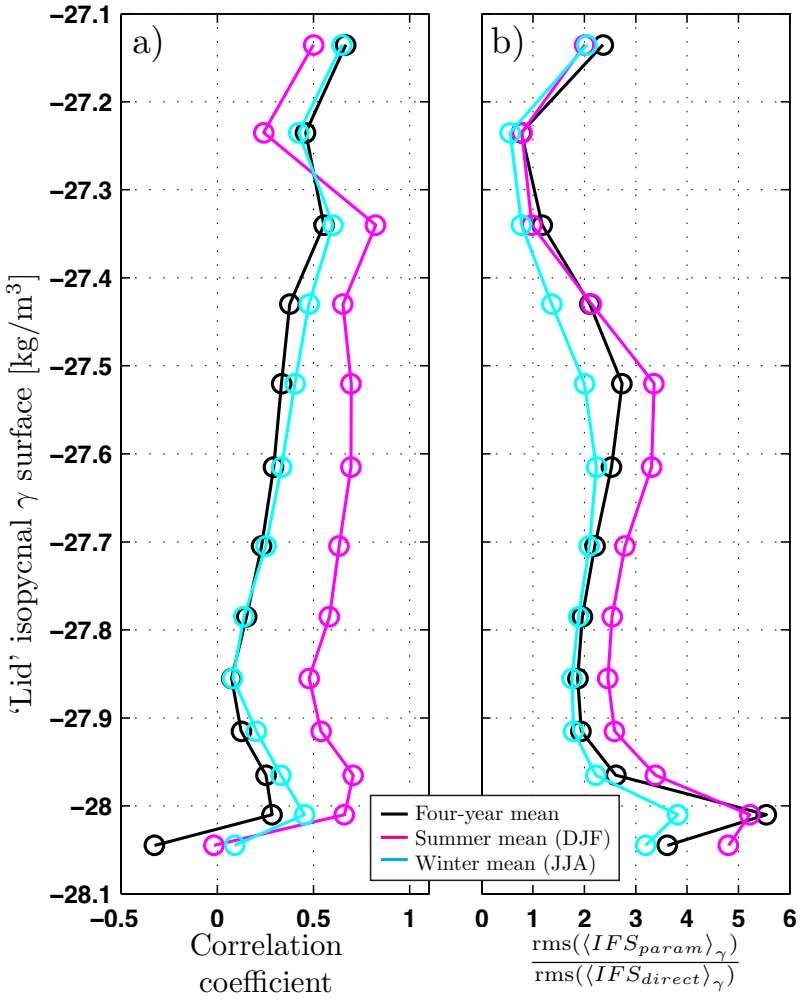

Figure 4.4: Comparison of time-mean and vertical-mean parameterized and direct IFS fields: correlation coefficient, (a), to compare the pattern between the two fields, and the ratio of the rms of the two fields, parameterized over direct, (b), to compare the magnitude of the two fields. Black indicates that the time-mean is over the full four years of the experiment; magenta indicates the time-mean over the summer months only (December, January, February); cyan line indicates time-mean over the winter months only (June, July, August).

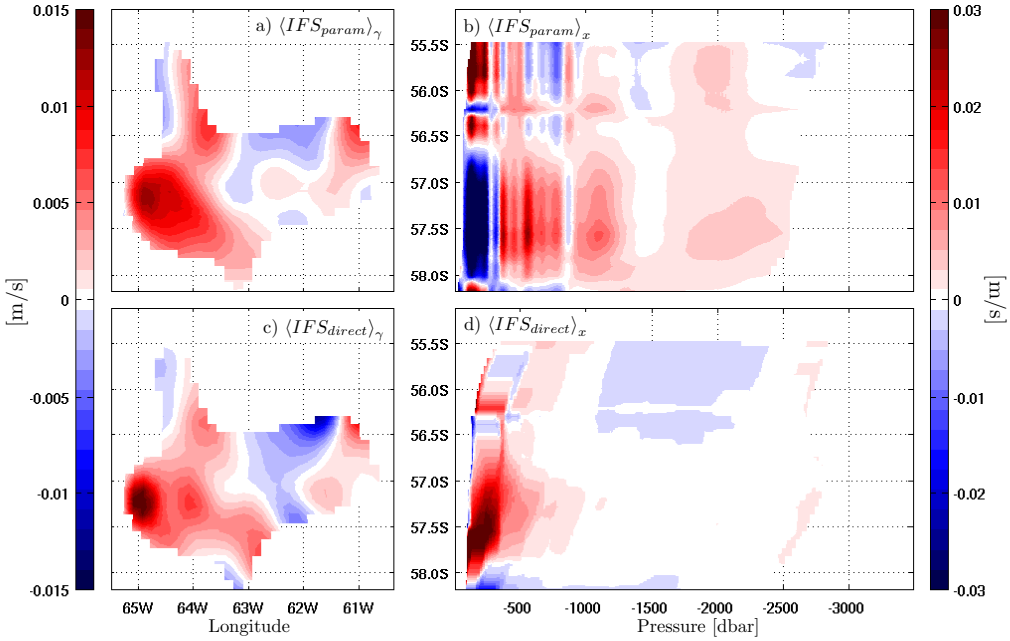

Figure 4.5: Best-match parameterized and direct IFS fields, averaged over the summer months only (December, January, February). Vertical average of domain bound by $\gamma = 28.075$ kg/m^3 at the bottom and $\gamma = 27.34$ kg/m^3 at the top for: parameterized field, (a), and direct field, (c). Zonal average of same domain for: parameterized IFS (c), and direct IFS (d), where isopycnal layer zonal averages have been interpolated to the mean vertical position of the layer. Correlation coefficient between (a) and (c) is 82%, and rms of (a) is 18% larger than rms of (c).

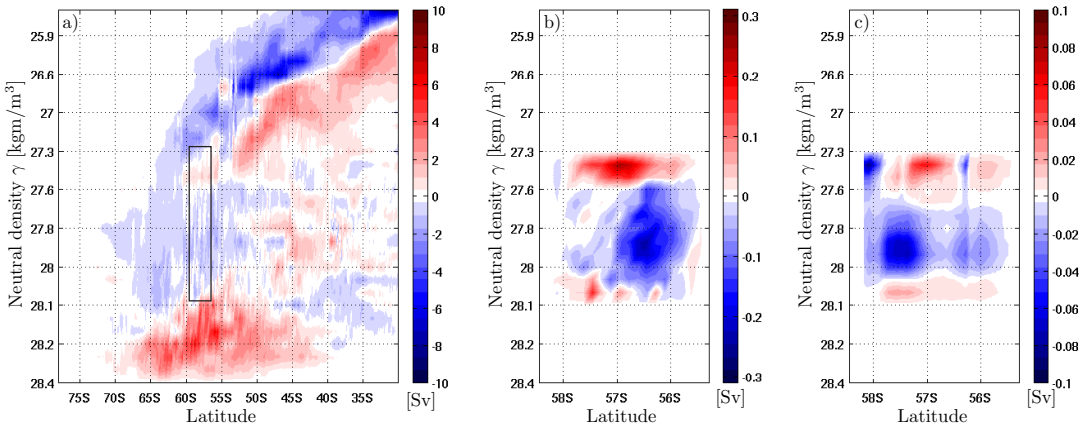

Figure 4.6: Vertical structure of the zonal sum of transport balanced by transient eddy IFS in: SOSE circumpolar domain, (a); SOSE cDrake area, (b); and observational cDrake array, (c). Black box in (a) shows area of (b) and (c).

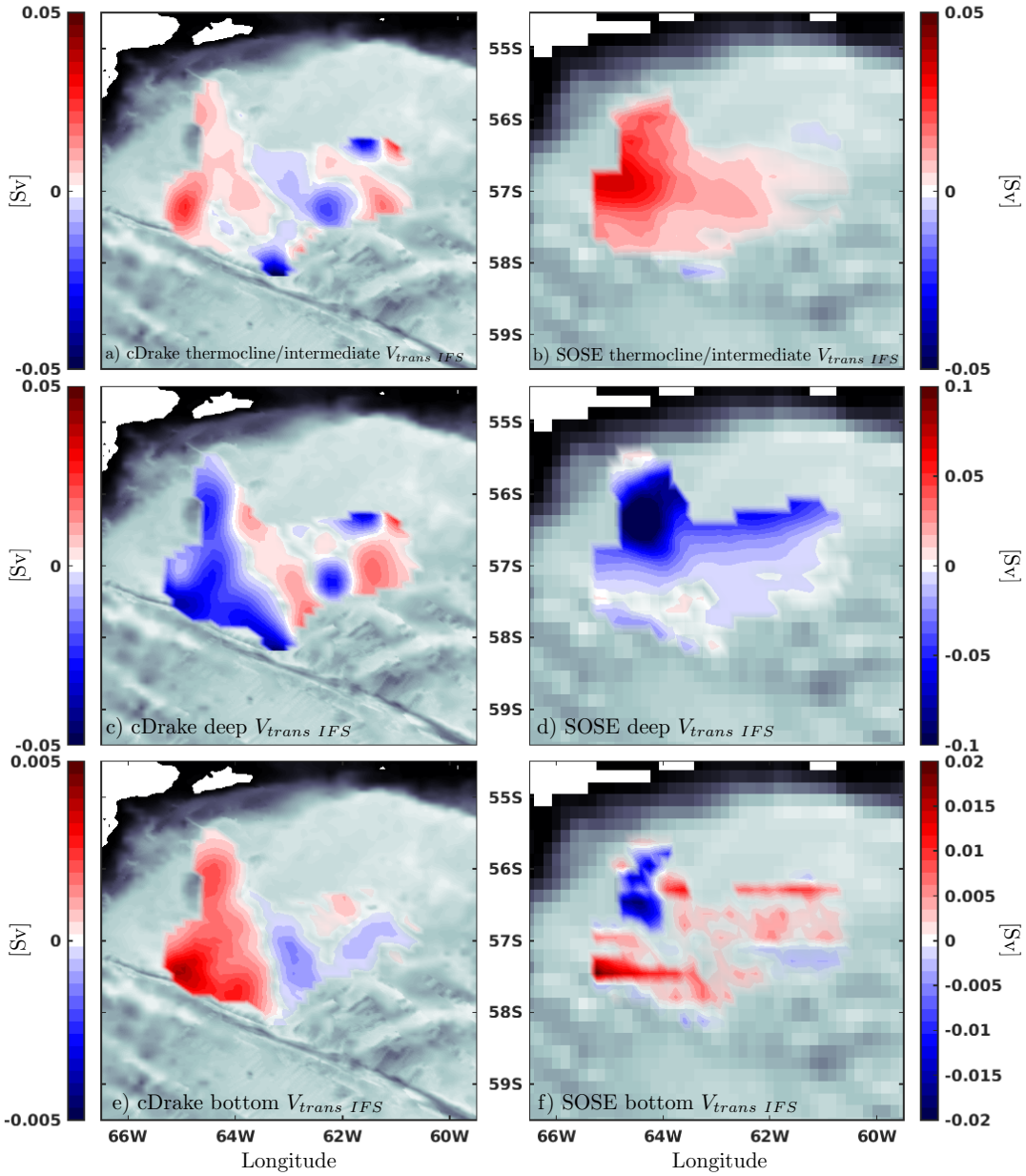

Figure 4.7: Thermocline/intermediate transport balanced by transient eddy IFS between $\gamma = [27.4, 27.6]$ kg/m^3 in cDrake observational estimate, (a), and SOSE model estimate, (b). Deep water transport between $\gamma = [27.6, 28.01]$ kg/m^3 balanced by transient eddy IFS in cDrake observational estimate, (c), and SOSE model estimate, (d). Bottom water transport between $\gamma = [28.01, 28.08]$ kg/m^3 balanced by transient eddy IFS in cDrake observational estimate, (e), and SOSE model estimate, (f). Grey shading shows underlying topography as in Figure 4.8 below.

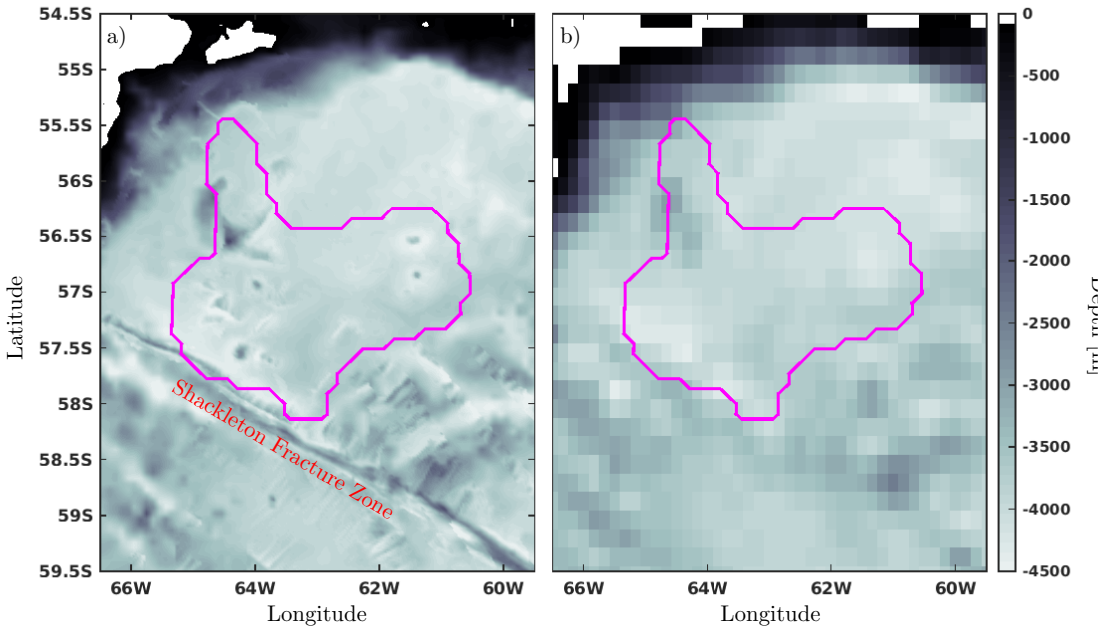

Figure 4.8: Bathymetry is combination of shipboard multibeam measurements from the R/V Nathaniel B. Palmer with the Smith and Sandwell (1997) satellite-derived bathymetry (Firing, 2012), (a). Southern Ocean State Estimate bathymetry, (b). Magenta contour shows boundaries of cDrake Local Dynamics Array map. Shackleton Fracture Zone labeled in red, (a).

Chapter 5

Summary and conclusions

This thesis has explored sources and sinks of zonal momentum in the Southern Ocean, and the pathways momentum travels through the fluid from surface source to seafloor sink. We have added to the existing understanding of the zonal momentum balance in the Southern Ocean by explicitly separating the topographic and interfacial form stress signals, and mapping each signal in three dimensions in the Southern Ocean State Estimate. We have ground-truthed the state estimate findings by calculating interfacial form stress via observational data from the cDrake experiment, located at a standing frontal meander in the Drake Passage.

Basin-scale maps of topographic form stress show that 95% of the momentum input by wind stress exits the fluid via topographic form stress in the Southern Ocean State Estimate, and that almost all of the wind stress is balanced by topographic form stress shallower than 3700 m depth. While nearly 60% of this topographic form stress occurs across submerged ridges, as Munk and Palmén (1951) surmised nearly 70 years ago, more than 40% occurs across the South American landmass; the zonal pressure gradient from the South Pacific to the South Atlantic, then, accounts for almost half of the momentum sink that prevents the ACC from accelerating indefinitely.

Basin-scale maps of interfacial form stress confirm the theory that IFS balances wind stress, and carries that momentum into the ocean interior. Isolated from wind stress and topographic form stress, the IFS field reveals this mechanical balance, as well as the signature of the surface buoyancy constraints that also set the structure and strength of the MOC. IFS balances southward flow of thermocline, intermediate, and deep water, and northward flow of bottom water.

Previous studies that do not separate topographic and interfacial form stresses have found that standing eddies dominate transient eddies in balancing the wind-driven Eulerian mean meridional overturning circulation. Most of the interfacial form stress transport in this analysis comprises transient eddies, rather than standing eddies. We infer that most of the standing eddy term must be present in the subset of the MOC balanced by topographic form stress, rather than interfacial form stress. Transient eddy IFS concentrates at large-scale topographically-steered ACC currents, suggesting that transient adjustments to the size and shape of these currents is the primary mechanism by which IFS balances wind stress, topographic form stress, and buoyancy constraints.

Observational estimates of IFS in the northern Drake Passage underline the heterogeneity of the IFS signal, demonstrating that time-mean IFS can vary widely in magnitude and sign across a frontal standing meander in the ACC. The zonally integrated observational IFS estimate provides a remarkable benchmark for the SOSE IFS field, exhibiting a north-south-north pattern of IFS transport that is present both in the observational estimate and the cDrake region subset of the model IFS field. Parameterized in terms of buoyancy flux, the cDrake IFS field closely aligns with previous estimates in the area. Finally, we compare the direct IFS field calculated as in Chapter Three and the parameterized IFS field calculated as in previous observational estimates. These two fields show a reasonably close match in pattern and magnitude in the vertical mean field, but a poor match in the zonal mean field. The reasons underlying this poor match

between parameterized and direct IFS are the subject of future study.

References

Andrews, D. and M. E. McIntyre, 1976: Planetary waves in horizontal and vertical shear: The generalized Eliassen-Palm relation and the mean zonal acceleration. *Journal of the Atmospheric Sciences*, **33**, 2031–2048.

Best, S., V. Ivchenko, K. Richards, R. Smith, and R. Malone, 1999: Eddies in numerical models of the Antarctic Circumpolar Current and their influence on the mean flow. *Journal of Physical Oceanography*, **29**, 328–350.

Böning, C. W., A. Dispert, M. Visbeck, S. R. Rintoul, and F. U. Schwarzkopf, 2008: The response of the Antarctic Circumpolar Current to recent climate change. *Nature Geoscience*, **1**, 864–869, doi:10.1038/ngeo362.

Chereskin, T. K., K. A. Donohue, D. R. Watts, K. Tracey, Y. Firing, and A. Cutting, 2012: cDrake: Dynamics and transport of the Antarctic Circumpolar Current in Drake Passage. *Oceanography*, **25**, 134–135.

Chidichimo, M. P., K. A. Donohue, D. R. Watts, and K. L. Tracey, 2014: Baroclinic transport time series of the Antarctic Circumpolar Current measured in Drake Passage. *Journal of Physical Oceanography*, **44**, 1829–1853.

Cutting, A. L., 2010: *Constituents of sea surface height variability in Drake Passage*. Masters thesis, University of Rhode Island.

Donohue, K. A., K. L. Tracey, D. R. Watts, M. P. Chidichimo, and T. K. Chereskin, 2016: Mean Antarctic Circumpolar Current Transport Measured in Drake Passage. *Geophysical Research Letters*.

Donohue, K. A., D. R. Watts, K. L. Tracey, A. D. Greene, and M. Kennelly, 2010: Mapping circulation in the Kuroshio Extension with and array of Current and Pressure recording Inverted Echo Sounders. *Journal of Atmospheric and Oceanic Technology*, **27**, 507–527.

Dufour, C. O., J. Le Sommer, J. D. Zika, M. Gehlen, J. C. Orr, P. Mathiot, and B. Barnier, 2012: Standing and transient eddies in the response of the Southern Ocean meridional overturning to the southern annular mode. *Journal of Climate*, **25**, 6958–6974.

Firing, Y. L., 2012: *Dynamics of the Antarctic Circumpolar Current in Drake Passage*. Ph.d. thesis, University of California San Diego.

Firing, Y. L., T. K. Chereskin, D. R. Watts, K. L. Tracey, and C. Provost, 2014: Computation of geostrophic streamfunction, its derivatives, and error estimates from an array of CPIES in Drake Passage. *Journal of Atmospheric and Oceanic Technology*, **31**, 656–680.

Gill, A. E., 1968: A linear model of the Antarctic Circumpolar Current. *Journal of Fluid Mechanics*, **32**, 465–488.

Gille, S. T., 1997: The Southern Ocean Momentum Balance: Evidence for Topographic Effects from Numerical Model Output and Altimeter Data. *Journal of Physical Oceanography*, **27**, 2219–2232, doi:10.1175/1520-0485(1997)027<2219:TSOMBE>2.0.CO;2.

Grezio, A., N. C. Wells, V. O. Ivchenko, and B. A. de Cuevas, 2005: Dynamical budgets of the Antarctic Circumpolar Current using ocean general-circulation models. *Q. J. R. Meteorol. Soc.*, **131**, 833–860, doi:10.1256/qj.03.213.

Hallberg, R. and A. Gnanadesikan, 2006: The role of eddies in determining the structure and response of the wind-driven Southern Hemisphere overturning: Results from the Modeling Eddies in the Southern Ocean (MESO) project. *Journal of Physical Oceanography*, **36**, 2232–2252.

Holloway, G., 1987: Systematic forcing of large-scale geophysical flows by eddy-topography interaction. *Journal of Fluid Mechanics*, **184**, 463, doi:10.1017/S0022112087002970.

Howard, E., A. McC. Hogg, S. Waterman, and D. P. Marshall, 2015: The Injection of Zonal Momentum by Buoyancy Forcing in a Southern Ocean Model. *Journal of Physical Oceanography*, **45**, 259–271, doi:10.1175/JPO-D-14-0098.1.

Hughes, C. W., M. P. Meredith, and K. J. Heywood, 1999: Wind-Driven Transport Fluctuations through Drake Passage: A Southern Mode. *Journal of Physical Oceanography*, **29**, 1971–1992, doi:10.1175/1520-0485(1999)029<1971:WDTFTD>2.0.CO;2.

Ivchenko, V. O., K. J. Richards, and D. P. Stevens, 1996: The Dynamics of the Antarctic Circumpolar Current. *Journal of Physical Oceanography*, **26**, 753–774, doi:10.1175/1520-0485(1996)026<0753:TDOTAC>2.0.CO;2.

Johnson, G. C. and H. L. Bryden, 1989: On the size of the Antarctic Circumpolar Current. *Deep-Sea Research*, **36**, 39–53.

Killworth, P. D. and M. M. Nanneh, 1994: Isopycnal Momentum Budget of the Antarctic Circumpolar Current in the Fine Resolution Antarctic

Model. *Journal of Physical Oceanography*, **24**, 1201–1223, doi:10.1175/1520-0485(1994)024<1201:IMBOTA>2.0.CO;2.

Lee, M.-M. and A. Coward, 2003: Eddy mass transport for the Southern Ocean in an eddy-permitting global ocean model. *Ocean Modelling*, **5**, 249–266.

Lenn, Y.-D., T. K. Chereskin, J. Sprintall, and E. Firing, 2007: Mean jets, mesoscale variability and eddy momentum fluxes in the surface layer of the Antarctic Circumpolar Current in Drake Passage. *Journal of Marine Research*, **65**, 27–58, doi:10.1357/002224007780388694.

Marshall, D., 1997: Subduction of water masses in an eddying ocean. *Journal of Marine Research*, **55**, 201–222.

Marshall, J., D. Olbers, H. Ross, and D. Wolf-Gladrow, 1993: Potential Vorticity Constraints on the Dynamics and Hydrography of the Southern Ocean. *Journal of Physical Oceanography*, **23**, 465–487, doi:10.1175/1520-0485(1993)023<0465:PVCOTD>2.0.CO;2.

Marshall, J. and T. Radko, 2003: Residual-mean solutions for the Antarctic Circumpolar Current and its associated overturning circulation. *Journal of Physical Oceanography*, **33**, 2341–2354.

Marshall, J. and K. Speer, 2012: Closure of the meridional overturning circulation through Southern Ocean upwelling. *Nature Geoscience*, **5**, 171–180, doi:10.1038/ngeo1391.

Masich, J., T. K. Chereskin, and M. R. Mazloff, 2015: Topographic form stress in the Southern Ocean State Estimate. *Journal of Geophysical Research: Oceans*, **120**, doi:10.1002/2015JC011143.

Mazloff, M. R., R. Ferrari, and T. Schneider, 2013: The Force Balance of the Southern Ocean Meridional Overturning Circulation. *Journal of Physical Oceanography*, **43**, 1193–1208.

Mazloff, M. R., P. Heimbach, and C. Wunsch, 2010: An Eddy-Permitting Southern Ocean State Estimate. *Journal of Physical Oceanography*, **40**, 880–899, doi:10.1175/2009JPO4236.1.

McWilliams, J. C., W. R. Holland, and J. H. Chow, 1978: A description of numerical Antarctic Circumpolar Currents. *Dynamics of Atmospheres and Oceans*, **2**, 213–291, doi:10.1016/0377-0265(78)90018-0.

Meinen, C. S. and D. R. Watts, 2000: Vertical structure and transport on a transect across the North Atlantic Current near 42°N: time series and mean. *Journal of Geophysical Research*, **105**, 21,869–21,891.

Morgan, P. P., 1994: SEAWATER: a library of MATLAB computational routines for the properties of sea water: Version 1.2. Technical report, CSIRO.

Morrison, A. K., T. L. Frölicher, and J. L. Sarmiento, 2015: Upwelling in the Southern Ocean. *Physics Today*, **68**, 27.

Munday, D. R., H. L. Johnson, and D. P. Marshall, 2013: Eddy saturation of equilibrated circumpolar currents. *Journal of Physical Oceanography*, **43**, 507–532.

Munk, W. H. and E. Palmén, 1951: Note on the Dynamics of the Antarctic Circumpolar Current. *Tellus*, **3**, 53–55, doi:10.1111/j.2153-3490.1951.tb00776.x.

Olbers, D., 1998: Comments on On the Obscurantist Physics of Form Drag in Theorizing about the Circumpolar Current*. *Journal of Physical Oceanography*, **28**, 1647–1654, doi:10.1175/1520-0485(1998)028<1647:COOTOP>2.0.CO;2.

Olbers, D., D. Borowski, C. Völker, and J.-O. Wölff, 2004: The dynamical balance, transport and circulation of the Antarctic Circumpolar Current. *Antarctic Science*, **16**, 439–470.

Olbers, D. and V. O. Ivchenko, 2001: On the meridional circulation and balance of momentum in the Southern Ocean of POP. *Ocean Dynamics*, **52**, 79–93.

Phillips, H. E. and S. R. Rintoul, 2000: Eddy Variability and Energetics from Direct Current Measurements in the Antarctic Circumpolar Current South of Australia. *Journal of Physical Oceanography*, **30**, 3050–3076, doi:10.1175/1520-0485(2000)030<3050:EVAEFD>2.0.CO;2.

Shakespeare, C. J. and A. M. Hogg, 2012: An analytical model of the response of the meridional overturning circulation to changes in wind and buoyancy forcing. *Journal of Physical Oceanography*, **42**, 1270–1287.

Smith, W. H. and D. T. Sandwell, 1997: Global sea floor topography from satellite altimetry and ship depth soundings. *Science*, **277**, 1956–1962.

Sprintall, J., T. K. Chereskin, and C. Sweeney, 2012: High-resolution underway upper ocean and surface atmospheric observations in Drake Passage: Synergistic measurements for climate science. *Oceanography*, **25**, 70–81.

Stephenson, G. R., S. T. Gille, and J. Sprintall, 2012: Seasonal variability of upper ocean heat content in Drake Passage. *Journal of Geophysical Research: Oceans*, **117**.

Stevens, D. P. and V. O. Ivchenko, 1997: The zonal momentum balance in an eddy-resolving general-circulation model of the southern ocean. *Quarterly Journal of the Royal Meteorological Society*, **123**, 929–951, doi:10.1002/qj.49712354008.

Sun, C. and D. R. Watts, 2001: A circumpolar gravest empirical mode for the Southern

Ocean hydrography. *Journal of Geophysical Research*, **106**, 2833–2855.

Swart, N. C. and J. C. Fyfe, 2012: Observed and simulated changes in the Southern Hemisphere surface westerly wind-stress. *Geophysical Research Letters*, **39**, doi:10.1029/2012GL052810.

Tansley, C. E. and D. P. Marshall, 2001: On the dynamics of wind-driven circumpolar currents. *Journal of Physical Oceanography*, **31**, 3258–3273.

Thompson, A. F. and A. C. Naveira Garabato, 2014: Equilibration of the Antarctic Circumpolar Current by Standing Meanders. *Journal of Physical Oceanography*, **44**, 1811–1828, doi:10.1175/JPO-D-13-0163.1.

Thompson, D. W. J. and S. Solomon, 2002: Interpretation of Recent Southern Hemisphere Climate Change. *Science*, **296**, 895–899, doi:10.1126/science.1069270.

Tracey, K. L., K. A. Donohue, D. R. Watts, and T. K. Chereskin, 2013: cDrake CPIES data report November 2007 to December 2011 GSO Technical Report 2013-01. Technical report, University of Rhode Island.

Treguier, A. M. and J. C. McWilliams, 1990: Topographic Influences on Wind-Driven, Stratified Flow in a β-Plane Channel: An Idealized Model for the Antarctic Circumpolar Current. *Journal of Physical Oceanography*, **20**, 321–343, doi:10.1175/1520-0485(1990)020<0321:TIOWDS>2.0.CO;2.

Vallis, G. K., 2006: *Atmospheric and oceanic fluid dynamics: fundamentals and large-scale circulation*. Cambridge University Press.

Ward, M. L. and A. M. Hogg, 2011: Establishment of momentum balance by form stress in a wind-driven channel. *Ocean Modelling*, **40**, 133–146, doi:10.1016/j.ocemod.2011.08.004.

Watts, D. R., K. L. Tracey, K. A. Donohue, and T. K. Chereskin, 2016: Estimates of eddy heat flux crossing the Antarctic Circumpolar Current from observations in Drake Passage. *Journal of Physical Oceanography*, 16–0029.

Webb, D. J. and B. A. De Cuevas, 2006: On the fast response of the Southern Ocean to changes in the zonal wind. *Ocean Science Discussions*, **3**, 471–501.

Wolff, J.-O., E. Maier-Reimer, and D. J. Olbers, 1991: Wind-Driven Flow over Topography in a Zonal β-Plane Channel: A Quasi-geostrophic Model of the Antarctic Circumpolar Current. *Journal of Physical Oceanography*, **21**, 236–264, doi:10.1175/1520-0485(1991)021<0236:WDFOTI>2.0.CO;2.

Young, W. R., 2012: An exact thickness-weighted average formulation of the Boussinesq equations. *Journal of Physical Oceanography*, **42**, 692–707.

Zika, J. D., J. Le Sommer, C. O. Dufour, J.-M. Molines, B. Barnier, P. Brasseur, R. Dussin, T. Penduff, D. Iudicone, A. Lenton, G. Madec, P. Mathiot, J. Orr, E. Shuckburgh, and F. Vivier, 2013: Vertical Eddy Fluxes in the Southern Ocean. *Journal of Physical Oceanography*, **43**, 941–955, doi:10.1175/JPO-D-12-0178.1.